Institute of Atomic Physics
Romanian Participation in EUROfusion
Annual Report 2017

Institute of Atomic Physics
http://www.ifa-mg.ro/index.php

Acknowledgments

This work has been carried out within the framework of the EUROfusion Consortium and has received funding from the Euratom research and training programme 2014-2018 under grant agreement No 633053. The views and opinions expressed herein do not necessarily reflect those of the European Commission.

The work carried out on complementary projects has been received funding from the Romanian National Education Ministry / Institute of Atomic Physics under contract 1EU-6/2014 and 2/2016.

Foreword

EUROfusion, the '*European Consortium for the Development of Fusion Energy*' (*https://www.euro-fusion.org/*), is a consortium of national fusion research institutes located in the European Union and Switzerland. It was established in 2014 to succeed the European Fusion Development Agreement (EFDA - *https://en.wikipedia.org/wiki/European_Fusion_Development_Agreement*) as the umbrella organisation of Europe's fusion research laboratories. The consortium is currently funded by the Euratom Horizon 2020 programme. EUROfusion manages and funds European fusion research activities on behalf of Euratom. Thirty research organisations and universities from 26 European Union member states plus Switzerland and Ukraine signed the EUROfusion consortium agreement. In addition, more than 100 Third Parties contribute to the research activities through the Consortium members. EUROfusion collaborate with Fusion for Energy (*http://fusionforenergy.europa.eu/*) and intensively support the ITER International Organization (*www.iter.org*).

EUROfusion funds fusion research activities in accordance with the Roadmap to the realization of fusion energy (*https://www.euro-fusion.org/wpcms/wp-content/uploads/2013/01/JG12.356-web.pdf*). The Roadmap outlines the most efficient way to realize fusion electricity. It is the result of an analysis of the European Fusion Programme undertaken in 2012 by the Research laboratories within EFDA. Its main objectives are: the preparation for the experiments on ITER, the world's largest tokamak, a magnetic fusion device that has been designed to prove the feasibility of fusion as a large-scale and carbon-free source of energy based on the same principle that powers our Sun and stars and the development of the concepts for the fusion power demonstration plant DEMO (https://www.euro-fusion.org/newsletter/demo-and-the-road-to-fusion-power/). The roadmap breaks the overall task into eight missions:

- **Plasma regimes of operation:** as plasmas must be confined at temperatures 20 times higher than the temperature of the core of the sun it is necessary to minimize the energy losses due to small-scale turbulence and the taming of plasma instabilities.
- **Heat-exhaust systems:** the power necessary to maintain plasmas at high temperatures is ultimately exhausted in a narrow region of the reaction chamber called the divertor. The need to withstand large heat loads led to the development of plasma facing materials and exhaust systems that should be adequate for ITER.
- **Neutron resistant materials:** The ultimate goal is to produce suitable structural and high-heat flux materials that will be able to ensure efficient electricity production and adequate plant availability; they also need to exhibit reduced activation so as to avoid permanent waste repositories.
- **Tritium self-sufficiency:** efficient breeding and extraction systems to minimize tritium inventory are necessary as DEMO will burn about 0.4kg of tritium per operational day; the choices of the materials and the coolant of the breeding blanket will have to be made consistently with the choice of the components for the transformation of the high-grade heat into electricity
- **Implementation of the intrinsic safety features of fusion:** fusion has intrinsic safety features which should be implemented in a coherent architecture in order to ensure the inherent passive resistance to any incidents and to avoid the need of evacuation in the worst incident case. The development of methods for reducing the problem associated with the presence of tritium in the components extracted for disposal and the definition of appropriate disposal routes are the main requirements.
- **Integrated DEMO design and system development:** compared to ITER, DEMO will need a more efficient technical solution for remote maintenance as well as highly reliable components; in addition, DEMO will need to exploit a highly efficient heat transfer and associated electrical generation systems.
- **Competitive cost of electricity:** the perspective of economic electricity production from fusion has to be set as a target, e.g. minimizing the DEMO capital costs. In order to meet this target, we must build on the experience of ITER, design solutions demonstrating a reliable plant with a high availability and serve as a credible data basis for commercial energy production.
- **Stellarators:** an additional objective is to bring the stellarator line to maturity as a possible long-term alternative to tokamaks. Stellarators have indeed intrinsic advantages relative to the tokamak, but their physics basis is not mature enough to achieve the goal of electricity from fusion by 2050.

EUROfusion funds the Research Units in accordance with their participation to the mission-oriented Work Packages outlined in the Consortium Work Plan. The Institute of Atomic Physics (IAP – *www.ifa-mg.ro*) is a member of the EUROfusion since the establishment of the Consortium, in 2014. IAP ensures the management of the Romanian participation in EUROfusion by coordinating the activity of 5 research institutes:

- *National Institute of Laser, Plasma and Radiation Physics (NILPRP),*
- *National Institute of Cryogenic and Isotope Technology (NICIT),*
- *National Institute for Research and Development in Optoelectronics (INOE 2000),*
- *National Institute of Physics of Materials (NIPM),*
- *National Institute of Physics and Nuclear Engineering (NIPNE)*

and three universities:

- *University of Craiova (UCv),*
- *University A. I. Cuza from Iasi (UAIC),*
- *Technical University Cluj-Napoca (UTCN).*

which acts as linked-third-parties inside the Consoritum.

The Romanian reasearch activities have been developed manly inside the ITER Physics workpackages:

- *WPJET1 (JET campaigns)*
- *WPJET2 (JET Plasma-Facing Components)*
- *WPJET4 (JET Enhancements)*
- *WPPFC (Preparation of efficient PFC operation for ITER and DEMO)*
- *WPCD (Code Development for Integrated Modelling)*
- *WPMST1 (Medium-Size Tokamak campaigns)*
- *WPISA (Infrastructure Support Activities)*
- *WPSA (Preparation of exploitation of JT-60SA)*
-

and also in the framework of Power Plant Physics and Technology department:

- *WPMAG - Magnets system project*
- *WPMAT - Materials project*

A consistent contribution has also been brought for the ‚*Enabling Research*' (WPENR) work package. In addition to the mission-oriented work, WPENR aims at promoting fundamental understanding and longer research perspective dedicated to nuclear fusion.

The 'Education' work package (WPEDU) has ensured the support for several PhD and Master students studying different aspects of nuclear fusion science and technology.

The main results of these research activities are presented in this report together with a comprehensive list of publications.

ew semi-analytical method for the study of turbulence in ITER plasmas

M. Vlad, F. Spineanu, V. Baran, D. Palade, A. Croitoru, A. Zubarev

National Institute for Lasers, Plasma and Radiation Physics, Bucharest-Magurele, Romania

WPENR1-P, EUROfusion Project: AWP17-ENR-MFE-IAP-04

Turbulence is a complex nonlinear process that mixes disorder and order. Quasi-coherence or order appears at the basic level of tracer trajectories in the case of smooth velocity fields that have finite correlation lengths. Ion trajectories are random sequences of trapping or eddying events and long jumps. The order of the trajectories determines much amplified and strongly complicated effects on turbulence fields due to the nonlinear constraints of the evolution. The turbulence that is dominantly two-dimensional has a self-organizing character, which consists of the generation of quasi-coherent large scale structures and flows.

<u>The development of the concept of invisible (hidden) drifts and the analysis of their effects</u>

We have found more subtle effects of organization in turbulence, namely the hidden drifts (HDs). We have defined the HDs and analysed some of their effects on turbulence evolution [2]. Essentially, the HDs are two opposite average velocities that compensate one another. The hidden drifts (HDs) are found in the statistics of the trajectories as organized components of the motion in the radial direction, that appear in the presence of a poloidal average velocity V_d. Average displacements conditioned by the sign of the initial potential appear as shown in Figure 1. They represent ordered steps in the stochastic motion, which lead to a pair of symmetrical average velocities. They exactly compensate one another and do not yield direct transport (average velocity).

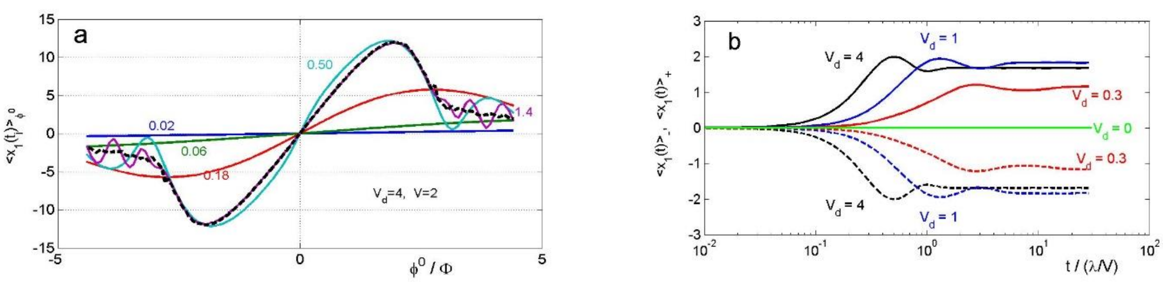

Figure 1 – The ordered motion that produces the HDs. a) The displacements conditioned by the initial value of the potential ϕ^0 have the sign of ϕ^0 at any time (the time moments label the curves and the dashed line correspond to the saturation. b) The average displacements conditioned by the sign of the initial potential are symmetrical time dependent functions, which depend on the average poloidal velocity V_d.

We have show that the HDs are the origin of strange turbulent fluxes (STFs), which consist of a stochastic advection process that depends on the sign of the fluctuations. The sign of the advected fluctuations is associated to the sign of the HD, so that the positive and the negative fluctuations move in opposite directions and generate fluxes. The HDs generate correlations of the Lagrangian velocity with the initial potential and with the initial vorticity $\omega = \Delta\phi$:

$$C_\phi = \langle \phi(0,0) v_r(x(t),t) \rangle, \quad C_\omega = \langle \omega(0,0) v_r(x(t),t) \rangle$$

They depend on V_d, on the amplitude V of the stochastic velocity and on the decorrelation time τ_d: Typical results are presented in Figure 2, which shows that both correlations are anti-symmetrical functions of V_d that increase with V and decay at small and large t_d:

The characteristics of the HDs and of the potential and vorticity STFs were determined using a semi-analytical approach, the decorrelation trajectory method, which describes both the random and the ordered aspects of tracer trajectories in stochastic velocity fields.

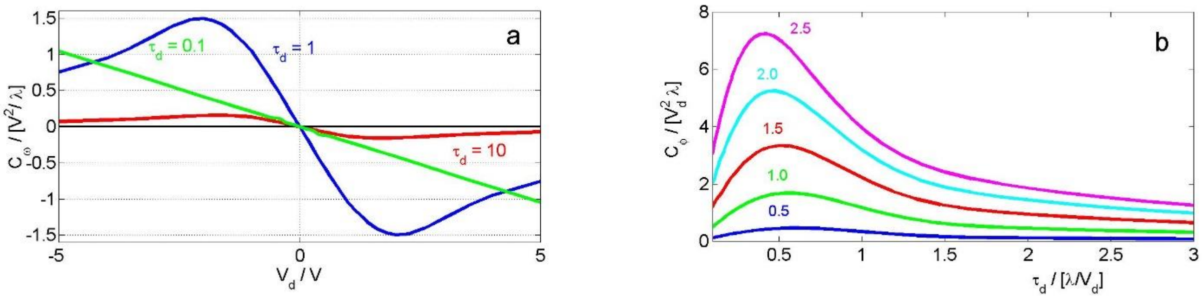

Figure 2 – The Lagrangian correlations C_ω and C_φ produced by the HDs.
a) C_ω as functions of the average velocity V_d for the values of τ_d that label the curves and $V = 1$.
b) C_φ as function of τ_d for the amplitudes V of the stochastic velocity field that label the curves and Vd = 4.

We have shown that the approximate adiabatic response that characterizes drift-type turbulence determines a STF of potential fluctuations, which modifies the frequencies of the test modes on turbulent plasmas. This process provides a new mechanism for the generation of zonal flow modes. The vorticity STF is expected to have important effects on turbulence evolution that will be evaluated in future work.
The results are presented in [2], [4], [C2] and [C3].

<u>*The development of the iterated self-consistent (ISC) approach for the study of turbulence evolution*</u>
The ISC approach is a combined study of test particle and test mode. Both depend on the momentary EC of the background turbulence, but iterated calculations of the statistics of the trajectories (including the characteristics of the quasi-coherent structures) and of the growth rate of the test modes permits the evaluation of the evolution of the EC.
The parameters of the quasi-coherent structures were determined using the DTM method. A detailed study of the dependence on the poloidal velocity and on the parameters of the turbulence (amplitude, shape of the Eulerian correlation, correlation lengths and time) was performed. The results are presented in [C1] and [3].
The method was applied to the drift turbulence. We have found two regimes [P1]. At weak drive the saturation is determined by ion diffusion, which determines a damping effect and significant change of the shape of the spectrum. At large drive, the quasi-coherent structures determined by trapping and the zonal flow modes that are generated have the main role in the saturation of the drift turbulence. The strength of the drive (that mainly depends on the parallel wave number) increases with plasma size. Thus, the second regime is predicted for ITER by this model.
We have studied test modes on turbulent plasmas for the case of dissipative trapped electron modes (DTEM) [5] and for the ion temperature gradient (ITG) driven turbulence [6], [C4], [C5]. The frequencies and the growth rates were determined as functions of the characteristics of the background turbulence. The ISC method was developed for the treatment of these instabilities by including the parallel spectrum and diffusion.
The results are presented in [1], [5], [6], [C4] and [C5].
A computer code was developed for the study of the drift turbulence using the ISC method. We note that this code is not performing the simulation of the turbulence, but it calculates the quantities related to test particles and test modes according to the iterated procedure. The run time is of few hours on a laptop.

Calculation of the radial current sustained by series of transient changes: ionization and trapping/detrapping events

F. Spineanu, M. Vlad, D. Palade, A. Croitoru, V. Baran, A. Zubarev

National Institute for Lasers, Plasma and Radiation Physics, Bucharest-Magurele, Romania
WPENR-C

The study of MHD invariants and of topological transformation that involve the plasma streamlines and the magnetic field lines provides a useful perspective on the regimes of low collisionality where radial redistribution of the current density and formation of Internal Transport Barriers occur. The experiment shows that in hybrid scenarios in some cases it is formed a channel of almost vanishing toroidal current centered on the magnetic axis (”hollow current profile”). It is rather localized in the sense that its limits are defined by an abrupt rise of the current amplitude.

The latter fact has suggested that we have a typical *skin* effect. The alternative view that can be proposed as an explanation for this hollow current profile is suggested by the Meissner effect. In this physical picture it is not the toroidal current that is expelled from the central region (as it is proposed by the skin effect) but it is the poloidal magnetic field that is expelled. The reason is that the central part is more and more similar to a superconductor.

Almost everything that characterizes the Meissner effect looks common to the central plasma region, with one exception: the need for a radial electric current in the case of the tokamak plasma, necessary for the generation of the circular electric field (through $\boldsymbol{v} \times \boldsymbol{B}$). We propose a physical explanation and a background for this radial current. It originates in two sources of current that is created in the central area and is directed toward the exterior of the plasma. One is the direct loss of part of the hot ions created by Neutral Beam Injection. It is a well documented phenomenon (DIII-D) that a loss of up to 40% of the new ions accompanies the countercurrent injection. The second is the current that occurs due to the transitory phase in the evolution of a newly born NBI ion which takes the banana orbit. For a short time, after each event of ionization of an NBI ion, there is a transient displacement which ends up when the ion is in periodic motion on the banana. Multiplied by the number of suce events it will produce a current which is oriented practically parallel with the equatorial plane. For shorter reference we will call this current ”expansion of bananas”. Both these currents (direct loss and expansion of bananas) intervenes in several processes. We mention two such processes. (1) the current completes the analogy between the dynamics in the center of the tokamak and the Meissner effect; (2) the current supports a torque that can lead to rotation of a radially finite layer which then acts as an Internal Transport Barrier

The conclusion is

- there is change of phase: *normal* to *superconducting*
- the change of phase takes place at a front $r_0(t)$ (an interface) separating the phases
- the superconducting phase advances radially
- there is charge motion in the direction of the advancement of the front, *i.e. radial*, v_r, as required by the London eq.

Radial current sustained by transient changes: ionization and trapping/detrapping events

Here we show results from the code LIGHTS, which we have written for the calculation of the transient current in plasma.

Papers

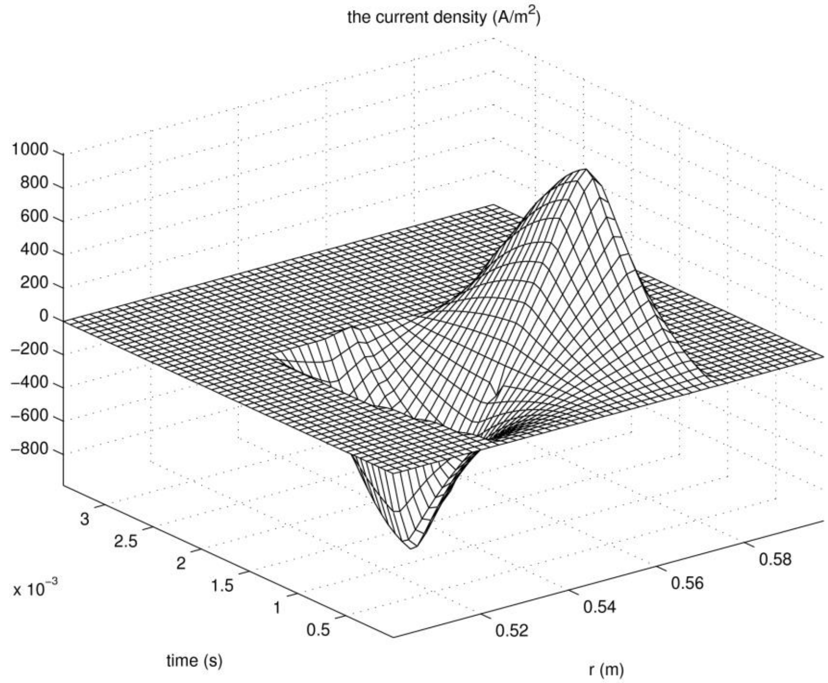

Figure: Current density from the transient events of ionization of a pellet.

The code LIGHTS collects all contributions from elementary events of ionization followed by expansion of the new ion's orbit until it reaches periodicity on the banana. This calculation is made with high accuracy since the trajectories of each new ion traverses different elements of a radial mesh, with the possibility to not be correctly recorded. However the result, after taking adequate measures on precision, is smooth. One can easily see that the current is rather high. It combined with the main magnetic field and produces a torque, able to rotate plasma poloidally.

The present stage of this investigation is devoted to evaluation of the Stringer mechanism which combines the poloidal nonuniformity of the fluxes with neoclassical gemetric effect. Then we expect to provide new arguments to the formation of the Transport Barriers (localized layers of poloidal rotation) when there is Neutral Beam Injection.

We have studied the generation of link number during magnetic reconnection by transition from a sheared magnetic field to a magnetic island where there are lines that turn around the local symmetry axis (the ”O” point of the island). Retaining just the topological aspect, we examine the generation of link using methods of field theory, two of them being possibly well-suited: (1) the sphaleron (transition over a finite heigth barrier); (2) the relaxation of a hyper-knot (process that is connected with axial anomaly and baryogenesis). We propose a description that can be applied to the generation of chiral fermions since they are similar to the discrete units of link. The example is a parallel to the axial anomaly.

The development of such line of study can help to quantify the degree of complexity of the magnetic field in a region of stochasticity (as occur in astrophysics or in incomplete magnetic re-connections in tokamak) with very important role in the transport processes.

Papers

[1] F. Spineanu, M. Vlad, On the late phase of relaxation of two-dimensional fluids: turbulence of unitons, Focus on Turbulence in Astrophysical and Laboratory Plasmas, New Journal of Physics 19 (2017) 025004.

Determination of the coupling between the eddy currents (due to the resistive wall modes (RWM)) and the sink/source currents (SSC) (due to Wall Touching Kink Modes (WTKM)). Deposition and characterisation of YBCO films on the LSMO nanoisland decorated substrates.

T. Petrisor[1], L. Ciontea[1], M. Nasui, T. Petrisor Jr[1]., R. B. Mos[1], C.V. Atanasiu[2], L.E. Zakharov[3], K. Lackner[4], M. Hoelzl[4], E. Strumberger[4] ,

1 Technical University of Cluj-Napoca-UTCN,

[2]National Institute for Laser, Plasma and Radiation Physics, Magurele, Romania,

[4]LiWFusion Princeton, USA,

[4]Max Planck Institute for Plasma Physics, Garching, Germany

WPENR-P

Determination of the coupling between the eddy currents (due to the resistive wall modes (RWM)) and the sink/source currents (SSC) (due to Wall Touching Kink Modes (WTKM)).

A rigorous mathematical formulation of the surface current circuit equations in the thin wall limit was given. In the triangular representation of the wall surface, both divergence-free eddy and source/sink currents are represented by the same model of a uniform current density inside each triangle. This model was implemented in the SSC and the shell simulation code SHL. The coupling of finite element matrix equations for both types of currents contains the same matrix elements of mutual capacitance of two triangles. The additional mutual inductances between eddy currents and source/sink currents, and mutual inductances between source/sink currents, use the same capacitance. This common feature provides the basis for interfacing upon necessity of the SSC and SHL codes with other similar codes, such as STARWALL, or source/sink codes which are under development with an alternative approach. The optimized formulation of the S/S-current problem for the typical tokamak situation of a localized wetting zone was presented. It is shown that the gradient representation can be used only in the wetting zone while the divergence-free stream-function representation of the surface current can used over the entire wall surface. The presented numerical examples correspond to typical geometries of the wall and the wetting zone. Our code received the status of ”open source licence”.

Deposition and characterisation of YBCO films on the LSMO nanoisland decorated substrates.

A new method to control the formation of oxide nanostructures grown on single crystalline substrates, namely the polymer-assisted surface decoration (PASD) technique, has been developed. Epitaxial LSMO nanoislands, with $(001)_{LSMO}||(001)_{MgO}$, and $[100]_{LSMO}||[100]_{MgO}$ relationship, have been grown from a polymeric precursor solution which enables an excellent control over the stoichiometry. This system presents nanostructures having a mean lateral size of 27 nm and 6 nm in height respectively. The oxide nanoislands are uniformly distributed on the (100)MgO substrate surface with a density of about 500 μm^{-2}. The TEM analysis indicates the existence of misfit dislocations at the LSMO/MgO interface. The size, dimension, and density of the nanoislands can be tuned by changing the concentration of metal ions in the precursor solution and the thermal treatment, rendering the method a high versatility. The efficiency of the LSMO nanostructures in vortex pinning was evaluated by critical current density, J_c, measurements on YBCO film epitaxially grown of the as decorated substrates. The mesurements were performed at different values of applied magnetic field and different temperatures. The J_c increase confirms the vortex pinning efficiency over a wide range of magnetic fields, even at temperatures close to the transition temperature, T_c. The J_c values were determined from V – I curves using a 5 µV/cm electric field criterion. At 77 K in zero field, the YBCO film has a J_c = 1.6 MA/cm^2, while this value for the YBCO/LSMO^{nano} film is J_c = 2.2 MA/cm^2. The increase of the of the critical current density by LSMO nano-particle substrate decoration is visible for all the values of the magnetic field, especially at high magnetic field values, at all the investigated temperatures. The J_c increase confirms the vortex pinning efficiency over a wide range of magnetic fields, even at temperatures close to the transition temperature, T_c. The evaluation of the pinning force density, F_p, reveals the positive effect of substrate decoration, figure 1b. In the case of the pure YBCO film the maximum F_p is 1.2 GN/m^3, while for the YBCO/LSMO^{nano} film this value is 1.8 GN/m^3. It is interesting to observe that field values for which these two values are obtained are different. For the YBCO film this value is 0.6 T, while for the YBCO/LSMO^{nano} film it is 1 T. The field values for which maximum of pinning force density is attained are called matching fields, and correspond to a situation in which the vortex lattice parameter is equal to the distance between pinning centers. Alternatively, at the matching field there is a maximum number of vortices pinned by the pinning centers. The expression for the matching field is $B = \Phi_0/a_p^2$, were Φ_0 = 2.068 × 10^{-15} Wb represents the magnetic flux quanta, and a_p is the vortex lattice parameter or the distance between pinning centers. For the two matching field values the following pinning center densities, $1/a_p^2$, were calculated, 300 μm^{-2} for the YBCO film and 500 μm^{-2}, for the YBCO/LSMO layer. The value 500 μm^{-2} represents an excellent agreement with the LSMO nanoparticle density on the MgO substrate. Thus, a conclusion may be drawn that the pinning centers in the YBCO/LSMO film are represented by the nano-islands. For a more quantitative analysis a Dew-Hughes approximation of the *f(b)* curves is needed. In this approach the *f(b)* curves are approximated by the following relation:

$$f = A \cdot h^p(1-h)^q,$$

where *A* is a numerical constant, and the *p* and *q* parameters are directly linked to the pinning mechanism. A variation of one or both parameters as a function of temperature indicates the presence of additional pinning mechanisms.

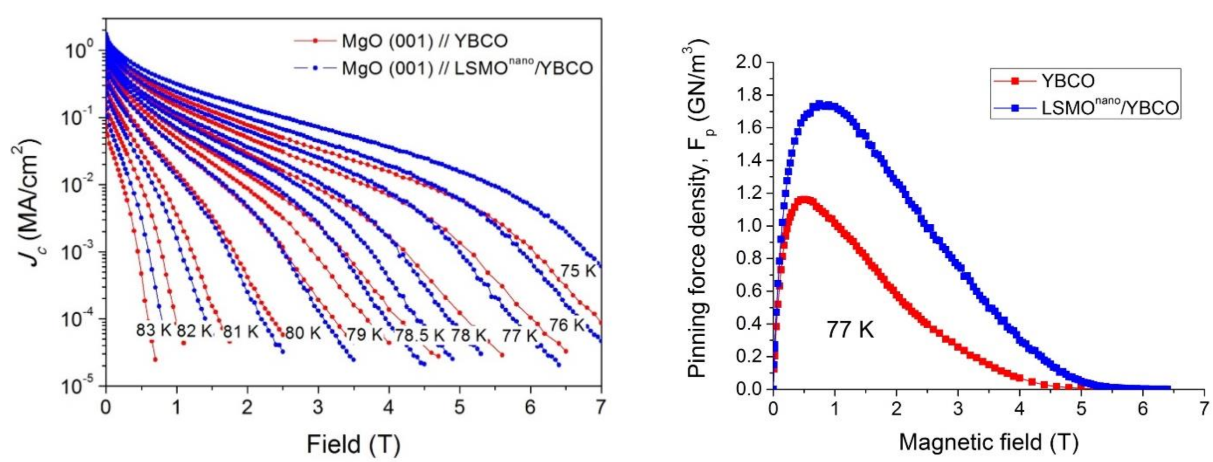

(a) (b)

Figure 1. *(a) The J_c (B) dependencies at different temperatures and (b) pinning force density at 77 K for the YBCO and YBCO/LSMO^{nano} films.*

The precursor coating solution is prepared starting from yttrium acetate $Y(CH_3COO)_3 \cdot 4H_2O$, barium trifluoroacetate $Ba(CF_3COO)_2$ and copper acetate $Cu(CH_3COO)_2 \cdot H_2O$ corresponding to the 1:2:3 stoichiometry. While the Ba trifluoroacetate is dissolved in methanol, the Y and Cu acetates are separately dispersed in methanol, treated with an excess of propionic acid (C_2H_5COOH), and further neutralized with NH_4OH until the solutions become clear. The three solutions are mixed together under stirring and concentrated by the removal of solvent under vacuum. The decomposition of the organic part of the precursor powder begins in the temperature range 175°C – 400 °C, indicated by a weight loss of 60% on the TG curve and by two exothermic peaks on the DTA curve at 332°C and 370°C, respectively. Above of 400°C the TG–DTA curves are stable, indicating that the thermal decomposition of the sample is complete. The asw obtained coating solution has been fully characterized to enable the optimization of the thermal treatment for adequate superconducting YBCO thin films. In order to determine the functional groups, the coating solution has been characterized by IR spectroscopy and the stability of the solution was determined by magnetic nuclear relaxometry (NMR).

Upgrading the experimental setups for production of ITER like surfaces and of surfaces coated with W nanoparticles

T. Acsente, C. Stancu, A. Lazea, G. Dinescu

National Institute for Laser, Plasma and Radiation Physics, 409 Atomistilor Str., PO Box MG-36, Magurele-Bucharest, 077125, Romania

Outline

1. General objectives of the project
2. The objectives of the activities in the present stage of the project
3. Results
4. Conclusions

1. General objective of the project

The project WPENR2-RO contract nr. 1EU-16/20.07.2017 is related to the Eurofusion WPENR project AWP17-ENR-MFE-CEA-10 "Study of Tritiated and non-tritiated dust Adhesion/re-suspension on Dedicated Surfaces" (Acronym STANDS), aiming at characterizing relevant properties of the dusts formed in tokamaks with respect to mobilization and removal phenomena. The INFLPR team contribution is related to the production of relevant W dust particles and ITER like surfaces, using plasma techniques.

2. The objectives of the activities in the present stage of the project

In this stage of the project we focused on techniques for production of relevant W dust particles and ITER like surfaces in order to be used by partners for adhesion and mobilization studies.

The activities were devoted to following: i)implementation of a setup and its testing for production of tungsten particles using an atmospheric pressure plasma jet; ii) configuration of the MSGA (magnetron sputtering combined with gas aggregation) experimental system for particles deposition on large area surfaces; preliminary delivery of such samples to project partners; iii)iImplementation of an experimental setup and obtaining of ITER like rough surfaces by sputtering in Ar plasma and He plasma of the exposed surfaces.

3. Results

3.1 Synthesis of W particles using atmospheric pressure plasma jet

Tungsten particles with various morphologies and sizes were obtained by using a radiofrequency (13.56 MHz) atmospheric pressure plasma jet operated with tungsten electrodes, at high argon mass flow rate. The main principle for production of particles consisted in erosion of the electrode surface during exposure to the plasma jet [1]. Quasi-sspherical particles (Fig. 1 down) obtained at P_{RF}= 200W, 3000 sccm, time= 20 min are adequate for adhesion experiments. Some samples were produced and delivered to the partners of the STANDS project for preliminary studies.

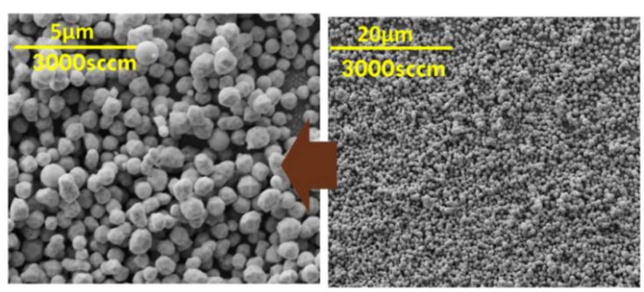

Figure 1. Tungsten particles obtained by the RF jet

3.2 Configuration of the MS-GAS (magnetron sputtering combined with gas aggregation) experimental system for uniform deposition on surfaces

In the operation of a MS-GS system W nanoparticles were previously obtained [1]. Usually, the particles are focused on spot of low area on a substrate. In the project, we realized experiments and identified conditions to obtain such particles distributed on a large area. Fig. 2 presents a picture of two foils of W (4 cm x 2.5 cm) covered with WNPs placed on a substrate holder. Such samples were delivered to STANDS project partners for preliminary take-off experiments with a Duster Box device.

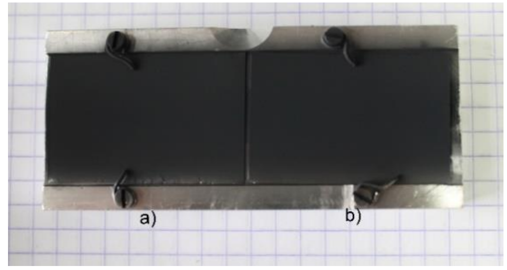

Figure 2. W substrates covered with W

3.3. Obtaining of ITER like rough surfaces by sputtering in Ar plasma and He plasma exposure

For obtaining W surfaces with various roughness we tested two approaches: i) roughening of the W sample by using it as target in magnetron sputtering, and ii) roughening of surface by submitting samples heated at more than 1000 ^oC to He containing discharges [2]. In Figure 3, optical images of a W target, before and after magnetron plasma exposure are presented, illustrating the roughening effect. The roughening by the He discharges is illustrated in Figure 4.

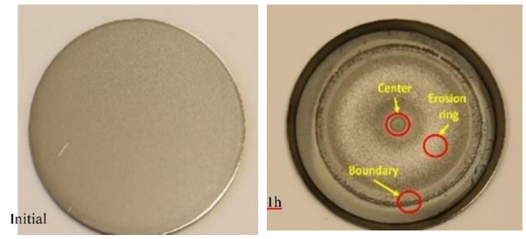

Figure 3. W surface roughening by sputtering

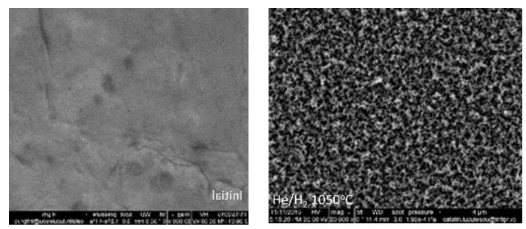

Figure 4. W surface roughening by discharge in He/H_2 at high temperature

4. Conclusion

Plasma procedures for producing tungsten particles by plasma at atmospheric pressure, coating of large surfaces with W nanoparticles at low pressure and production of ITER-like surfaces by plasma erosion are implemented and are in use for further preparation of samples for the project partners.

DETERMINATION OF THE COUPLING BETWEEN THE EDDY CURRENTS DUE TO RESISTIVE WALL MODES AND THE SINK/SOURCE CURRENTS DUE TO WALL TOUCHING KINK MODES

C.V. Atanasiu[1], L.E. Zakharov[2], K. Lackner[3], M. Hoelzl[3]

[1]National Institute for Laser, Plasma and Radiation Physics, Magurele, Romania,
[2]LiWFusion Princeton, USA,
[3]Max Planck Institute for Plasma Physics, Garching, Germany

WP-ENR_P & WP-CD_P

The understanding of plasma disruptions in tokamaks and predictions of their effects require realistic simulations of electric currents excitation in 3-dimensional vessel structures by the plasma touching the walls. The Wall Touching Kink Modes (WTKM) are frequently excited during the Vertical Displacement Events (VDE) and cause big sideways forces on the vacuum vessel which are difficult to confront in large tokamaks. In ITER, the occurrence of a limited number of major disruptions wills definitively damage the chamber with no possibility to restore the device. The aim of the present work was to understand how currents flow to the plasma facing surfaces during disruption events as the key basis for disruption modelling and vessel design. For the purpose of WTKM modelling the surface current density $\mathbf{j}d_w$ in the conducting shell has been split into two components ($\mathbf{j}$ is the current density in the wall of thickness d_w): (a) one is a divergence free surface current $\mathbf{i}$ and (b) the second one is a current proportional to $\nabla\Phi^S$ with potentially finite divergence in order to describe the plasma sink/source of the wall current. If in a previous task, we have developed a methodology to calculate the plasma sink/source surface current, in the present task we have developed a Finite-Element matrix representation of the energy functional for inductively driven eddy currents by using the same approach as for the Sink/Source (S/S) surface currents (SSC). The minimization of quadratic forms representing the two energy functionals leaded to linear systems of equations with symmetric positively defined matrices which has been solved using the Cholesky decomposition. Thus, the calculation of both wall currents was reduced to two relations. As output, our code returns the values of the stream function and the source/sink potential Φ^S in all vertexes, allowing the calculation of the magnetic vector potential **A** and magnetic field **B** of the wall currents in any point. For a given Finite-Element (FE) discretisation of ITER, with 21744 triangles and 11223 vertexes of the FE discretization the matrices size are of order of 1GB. Some numerical results are given in the next figures. The following milestones have been accomplished:

1) Creation of a Finite-Element matrix representation of the energy functional for inductively driven eddy currents by using the same approach as for the Sink/Source surface currents;
2) The eddy surface currents in 3D thin wall with holes have been calculated given the external time dependent magnetic flux by developing a Shell simulation code (SHL);
3) The inductive coupling between the two surface current components by considering a real-time dependence rather than a simplified $exp(\gamma t)$ type one has been determined;
4) A unified formulation for both surface current components has been developed;
5) To check the accuracy of our numerical results, we have developed an ITER wall case allowing an analytical solution.

Results

We have considered the ITER wall geometry with holes given in Fig. 1 and Fig. 2. We have identified the FE edge elements in ITER discretized with 21744 FE triangles presenting 11223 vertexes. We have considered a wetting zone created by a shifted vertically toroidal plasma and an m/n=1/1 kink mode (Fig. 3). The resulted eddy currents excited by the plasma perturbation and the corresponding stream function I distribution is given in Fig. 4. In Fig. 5, the eddy currents excited by both plasma perturbation and S/S currents are represented and the distribution of $\emptyset^S$ at the wall surface is given. Finally, the total surface current with the S/S current as the dominant component are reported in Fig. 6.
Our code received the status of "**open source licence**" and can be accessed now by the entire European fusion community.

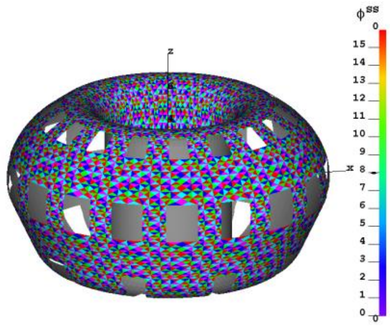

Figure 1 - 21744 FE triangle distribution in ITER wall

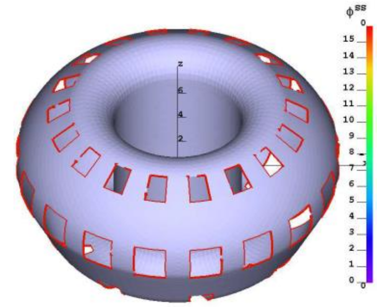

Figure 2 - Identifying the FE edge elements in ITER wall

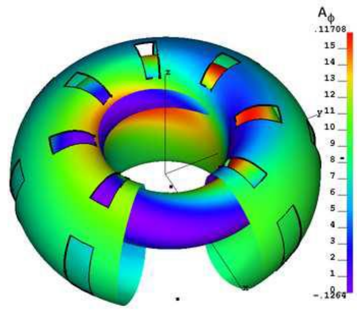

Figure 3 - Wetting zone created by a shifted vertically toroidal plasma with a kink m/n=1/1. The color of the wall ≡ distribution of the perturbed Aφ.

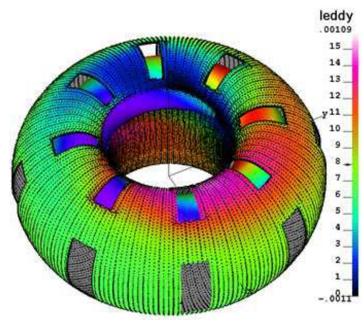

Figure 4 - Eddy currents excited by the plasma perturbation. The color corresponds to the I stream function.

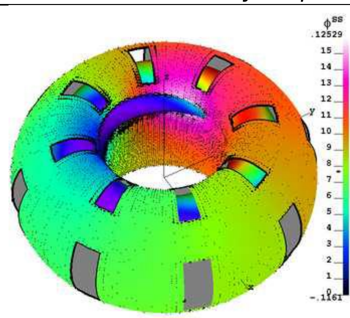

Figure 5 - Eddy currents excited by both plasma perturbation and S/S current. Distribution of Φ^S at the wall surface.

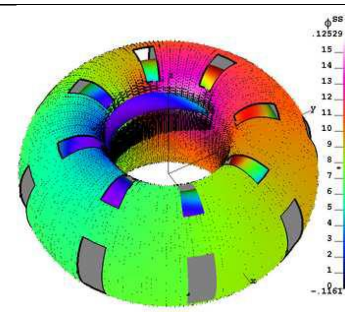

Figure 6 - Total surface current with the S/S current as the dominant component.

OPTIMIZATION OF THE CODE FOR SURFACE CURRENTS DETERMINATION IN THE TOKAMAK WALL

C.V. Atanasiu[1], L.E. Zakharov[2], K. Lackner[3], M. Hoelzl[3], G. Steinbrecher[4], N. Pometescu[4], D. Dumitru[1]

[1]*National Institute for Laser, Plasma and Radiation Physics, Magurele, Romania*

[2]*LiWFusion Princeton, USA*
[3]*Max Planck Institute for Plasma Physics, Garching, Germany*
[4]*University of Craiova, Physics Department, Romania*

WP-CD_C

The Wall Touching Kink Modes (WTKM) are frequently excited during the Vertical Displacement Events (VDE) and cause big sideways forces on the vacuum vessel which are difficult to confront in large tokamaks. In ITER, the occurrence of a limited number of major disruptions will definitively damage the chamber with no possibility to restore the device. In a previous step of this project, a rigorous mathematical formulation of the surface current circuit equations in the thin wall approximation was given. In the triangular representation of the wall surface, both divergence-free eddy and source/sink currents were represented by the same model of a uniform current density inside each triangle. This model was implemented in the source/sink currents SSC and the shell simulation code SHL.
Our code received the status of "**open source licence**" and can be accessed now by the entire European fusion community. In the present stage, two tasks have been considered:

A) Reducing the influence of the singularities appearing during the surface currents determination in multiply connected domains (L-shaped domains).

We have considered the ITER wall geometry with holes given in Fig. 1. We have identified the FE edge elements in ITER discretized with 21744 FE triangles and 11223 vertexes. By developing a case with an analytical solution, we have find that if for 1 hole the relative error was of 0.003 for a grid with a FE mesh 32×32×4, for 3 holes the error is ≈ 5 times greater. This is due to the presence of many re-entry corners. The following Poisson problem has been considered:

$$d_w \frac{\partial(\frac{\mathbf{n}}{d_w}\cdot\mathbf{B})}{\partial t} = d_w \sigma \frac{1}{D}\left\{\frac{\partial}{\partial u}\left[\frac{1}{\sigma d_w}\left(\frac{g_{vv}}{D}\frac{\partial I}{\partial u} - \frac{g_{uv}}{D}\frac{\partial I}{\partial v}\right)\right] + \frac{\partial}{\partial u}\left[\frac{1}{\sigma d_w}\left(\frac{g_{uu}}{D}\frac{\partial I}{\partial v} - \frac{g_{uv}}{D}\frac{\partial I}{\partial u}\right)\right]\right\},$$

where I is the stream function of the divergence free component (eddy currents), d_w is the wall thickness, σ is the wall conductivity, g_{uu} , g_{uv} and g_{vv} are the covariant metric coefficients. **B** is the magnetic field on the wall surface. Numerically, this problem has been solved by using conformal transformations. In Fig. 2, the distribution of the relative error between the numerical solution without improvement and the analytical one is given, while in Fig. 3, the same distribution is presented but with a numerical solution improved by using conformal transformations. With our correction method, the relative error is significantly smaller.

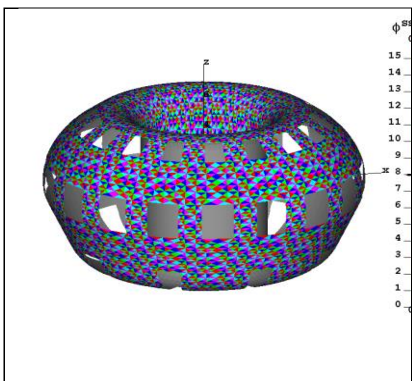

Figure 1 - 21744 FE triangles and 11223 vertexes in ITER

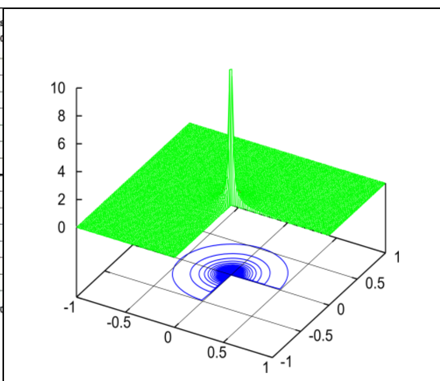

Figure 2 - Distribution of the relative error (Ia-In)/Ia [%] without improvement

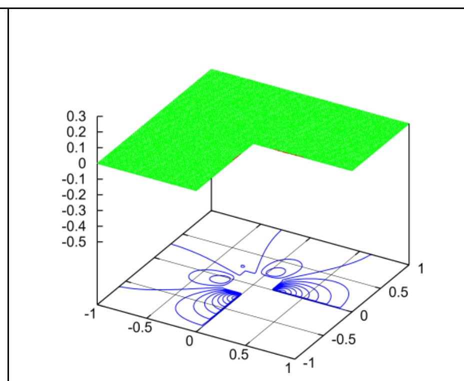

Figure 3 - Distribution of the relative error (Ia-In)/Ia [%] with conformal transformation improvement

B) Developing a compatibility between the geometry discretised by triangles and the geometry discretised by nonconforming Bezier finite elements and mathematical algorithm for the case of nonconforming Fourier elements.

In order to extend the existing code [1] for solving the MHD equations to the case when a limiter is attached to the tokamak was elaborated an efficient method which takes into account the nonconforming aspect of the finite elements in the new configuration. Correspondingly, a numerical algorithm from the class of conjugated gradient with linear restriction, for the case when the objective function is at most of second degree, was elaborated. The algorithm uses the special structure of the boundary conditions on the line where the limiter is attached on the tokamak wall to achieve better performances compared to existing general minimization algorithms [7].

The resulting FORTRAN90 programme was tested on synthetic data. The singular behaviour of the electric field on the limiter inner boundary was studied on analytic model, as well as its effect on the accuracy of finite element approximation.

In the case when the tokamak wall is discretised with triangular finite elements and an attached metallic plate is discretised with non-conforming Bezier finite elements, error bound for the approximation of smooth functions by finite elements was derived. The compatibility of non conforming heterogeneous geometries was treated by the general method, relaxing the continuity and first derivative smoothness with the weak continuity requirement, involving the averaging of the jump across the boundary with a set of polynomial weight. In this method (the so called mortar algorithm) the continuity and smoothness requirement is relaxed by requiring the vanishing of the averaged jump values. This algorithm was realized as a set of FORTRAN90 programme, with increasing complexity. The approximation error of a set of test functions, in two variables, (the tokamak wall parameterized) was computed by using the classical first order triangular conforming finite element system, by conforming and nonconforming Bezier finite elements and finally by a combined set of heterogeneous finite element system containing both quadrilateral (5, 5) order nonconforming finite elements as well as classical first order triangular finite elements.

In the case of nonconforming Fourier elements we consider the tokamak wall covered by a non-conformal set of convex quadrilateral finite elements; on the each quadrilateral we have defined a set of basis functions generated by trigonometric polynomials. By using the mortar element method, the compatibility problem of the nonconforming Fourier finite elements was reduced to a set of linear constraints on the Fourier coefficients of two Fourier quadrilateral finite element, whose edge have a common part of non zero length. In a similar manner, the compatibility problem of the triangular geometry on the limiter and the quadrilateral Fourier nonconforming finite elements was reduced to a set of linear constraints on the Fourier coefficients and the coefficients of the linear functions associated to the triangles from neighbourhood of the quadrilateral finite element [8]. The resulting quadratic minimization problem with linear constraints it is possible to be reduced to the problem solved in ref [9].

MODELLING OF THE LOW ROTATION REGIME EFFECT ON THE NTM ONSET AND EVOLUTION

Iulian Gabriel Miron[1]

[1] *National Institute for Lasers, Plasma and Radiation Physics, Bucharest, Romania*

WP-MST1

The MST1 Working Package is an important part of the Work Plan for the Implementation of the Fusion Roadmap in 2014 – 2018. In our case, it is of a peculiar importance, due to the simple fact that the problem treated here, the influence of the low plasma rotation on NTM, is specific to very few tokamak installations that belong to the Mid-Sized tokamaks (TCV, for instance). Therefore, our objective results are to be compared to the MST1 experimental results. The participation of the Romanian research groups to the mentioned campaign is linked to Topic 9 tasks, “Assess plasma stability performance and stability control in high-beta and advanced tokamak regimes”.

Our model has been used for the low rotational regime, by solving the perturbed equations in the ideal plasma surrounding the magnetic island, the perturbed equations in vacuum and the circuit equations in the external structures outside the plasma column. A resulting linear system of perturbed equations has been solved. The jump of the perturbation across the resistive magnetic island is initially provided within the linear theory threshold, for a finite island width [1]. We have obtained, just outside the magnetic island, the tearing mode solution as a perturbed magnetic flux function

$$\Psi_{TM}^{mn}(t) = A_s^{mn} + B_s^{mn} e^{-in\Omega_{err}t} + \sum_{p=1}^{6L} C_{ps}^{mn} e^{\tau_p t} \tag{1}$$

The parameters shown above are analytically derived functions of ideal plasma, wall, coils, error field (static and/or rotational) and initial perturbations parameters. Specific index notations are used [2]. In order to calculate the neoclassical tearing mode perturbed flux, the perturbed resistive magnetic island equations are to be solved. We have used the inner island perturbed equations solution found in Ref [3]. By replacing their test function with our real, time dependent, above calculated solution outside the island, we have obtained the inner magnetic island solution, i.e. the NTM flux function [4]

$$\Psi_{NTM}^{mn}(t) = \frac{1}{\tau_{FKR}^{5/4}}\left\{\frac{A_s^{mn}}{\Gamma(9/4)}t^{5/4} - \frac{iB_s^{mn}}{n\Omega_{err}}\left[\frac{t^{1/4}}{\Gamma(1/4)}\left(4 + e^{-in\Omega_{err}t}E_{3/4}(-in\Omega_{err}t)\right) - \frac{e^{-in\Omega_{err}t}}{(-in\Omega_{err}t)^{1/4}}\right]\right.$$
$$\left. - \sum_{p=1}^{6L}\frac{C_{ps}^{mn}}{\tau_p}\left[\frac{t^{1/4}}{\Gamma(1/4)}\left(4 + e^{\tau_p t}E_{3/4}(\tau_p t)\right) - \frac{e^{\tau_p t}}{{\tau_p}^{1/4}}\right]\right\} \tag{2}$$

We retrieve our calculated parameters from (1), A_s^{mn}, B_s^{mn}, C_{ps}^{mn} and τ_p. We now have everything we need concerning the NTM calculations.

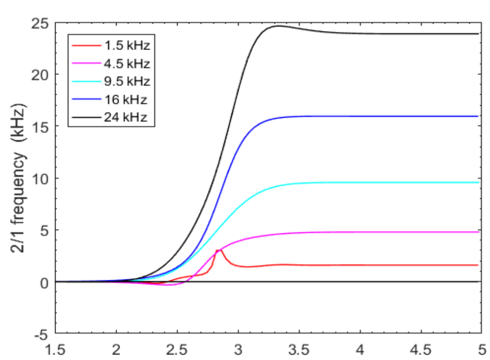

Figure 1: 2/1 mode frequency evolution for different rotation frequencies

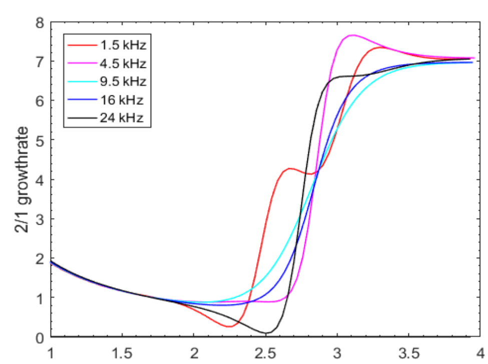

Figure 2: 2/1 mode growth rates for different plasma rotations

The absolute value of the expression of (2) is the NTM amplitude, the real part of its time derivative over Ψ_{NTM}^{mn} is the mode growth rate, the imaginary part of the former quantity is the frequency and the argument of Ψ_{NTM}^{mn} is the phase of the NTM.

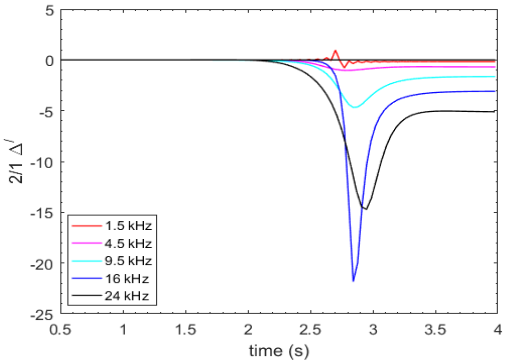

Figure 3: 2/1 mode stability index evolution for plasma rotation frequencies

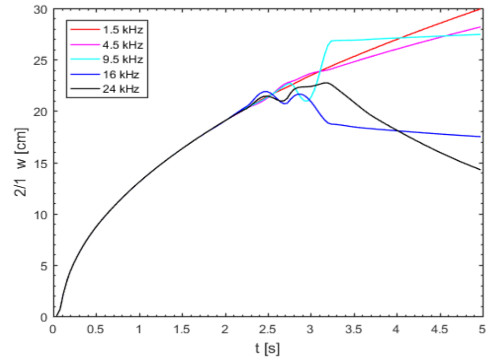

Figure 4: 2/1 magnetic island width for different plasma rotations

The rotation frequency of the plasma is an explicit parameter found in both (1) and (2). We will study the most important *m/n* NTMs evolution, the 2/1 and 3/2 modes. *m* and *n* are the poloidal and toroidal numbers, respectively. To estimate the role of the plasma rotation on the mode evolution, different dependencies are drawn when plasma rotation spans a wide range of values. An error field spectrum is considered here, generated by external coils disposed around the plasma column. It is clear from Figure 1 that as the plasma rotation is higher, the 2/1 mode rotation follows the plasma behaviour, despite the coupling with the existing error field. As for the 2/1 mode growth rate, the onset threshold of the mode appears to be minimum for the lowest plasma rotation rate (Fig.2). However, it seems that there is not a monotone dependence between the NTM threshold onset and the plasma rotation, from the growth rate perspective. Instead, regarding the stability index, the higher the plasma rotation is, the higher the onset threshold and the bigger negative value for the stability index become, as expected (Fig.3). The above quantity is calculated as $\Delta'_{NTM}(t)=-(2m/r_s)[1-\Psi^{mn}_{TM}(t)/\Psi^{mn}_{NTM}(t)]$, where r_s is the radial coordinate of the magnetic surface where the island forms. By solving the modified Rutherford equation, the magnetic island width is calculated. Figure 4 clearly shows the stabilizing effect of the plasma rotation of the 2/1 NTM evolution. A similar evolution is treated for the 3/2 mode. At very low rotation, whatever parameter variation has no or very little effect on the NTM onset and evolution. Figure 5 shows the 3/2 island evolution for different plasma co- and counter-currents regarding the plasma rotation. It seems that the mode becomes more unstable not only where the positive plasma current increases, but when its absolute value gets higher.

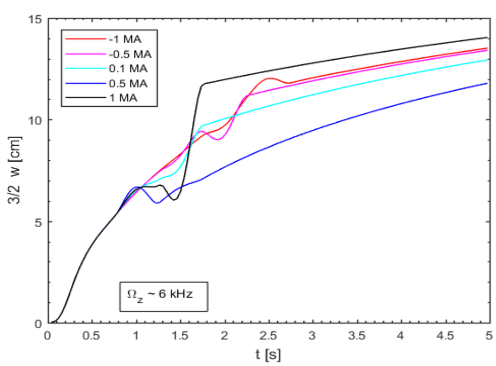

Figure 5: 3/2 magnetic island width for different plasma co- and counter-currents

To conclude, the most important NTM modes ((2,1) and (3,2)) have been studied here within the low plasma toroidal rotation regime. It has been retrieved the fact that NTM onset threshold increases with the rotation and it has been found that the lower the rotation is, the more ineffective the other parameters becomes in order to change the NTM stability conditions. The model proposed here is fit to exhibit the evolution of the NTM and its corresponding magnetic island and could become a handy tool to check or find supplementary information that the experimental campaigns are difficult to achieve.

References

[1] C.C Hegna and J.D., Phys. Plasmas 1, 2308 (1994)

[2] I.G. Miron, Plasma Phys. Control. Fusion 50, 095003 (2008)

[3] C.C Hegna, J.D. Callen and R.J. LaHaye, Phys. Plasmas 6, 130 (1999)

[4] I.G.Miron, "Modelling of seed magnetic island formation", P2.060, 43rd EPS Conference on Plasma Physics, July 4-8 2016, Leuven, Belgium.

MODELLING OF THE NTV EFFECT ON THE NTM STABILITY DUE TO THE NON-RESONANT COUPLING. DERIVATION OF THE KINETIC TERMS

Iulian Gabriel Miron[1]

[1] *National Institute for Lasers, Plasma and Radiation Physics, Bucharest, Romania*

WP-MST1

The project intends to establish the role of the neoclassical toroidal viscosity (NTV) torque on the onset and evolution of the neoclassical tearing modes (NTM). The challenge was to assess whether the non-resonant NTV torque or the resonant electromagnetic (EM) torque prevail as the main torque mechanism of the NTM destabilization. Previous theoretical studies have claimed that the damping effect of the NTV quantity is the main drive for the NTM stability degradation whereas some AUG experimental results have shown that the resonant coupling between the NTM and the external perturbations is the principal mechanism of the NTM unstable behaviour. We have kinetically modelled the NTV torque quantity starting from the derivation of the perturbed traceless pressure tensor. A weak particles collisionality regime is taken into account for which the particles energy integral is calculated keeping into account the resonance between the particles bounce orbit expansion frequency and the plasma toroidal rotation frequency. If this is the case, the mentioned energy integrals become singular, its Cauchy principal values being used instead of it. The NTV quantity magnitude due to the magnetic field broken symmetry. On the other hand, the latter quantity explicitly depends of the magnetic flux perturbations (namely the NTMs in our case) that are calculated by solving the perturbed equations in the whole space. The calculated solution provides the same NTM perturbed magnetic flux quantity that is used for the EM torque calculations.

Following Ref. [1] we have obtained a perturbed particle distribution function, to be used to calculate the perturbed pressure tensor $\mathbf{p} = p\mathbf{I} + p_{||}\mathbf{nn} + p_{\perp}(\mathbf{I} - \mathbf{nn}) = p\mathbf{I} + \boldsymbol{\pi}$, (p is the scalar perturbed pressure, **I** the unit tensor and $\mathbf{n} = \mathbf{B}/B$ the equilibrium magnetic field unit vector). We have obtained an analytic expression of the perturbed and the equilibrium canonical momentum, the magnetic moment, the particle energy and the equilibrium (Maxwellian) particle distribution function, respectively, the particles temperatures, the plasma toroidal angular rotation frequency and the trapped particles bounce and bounce-averaged toroidal precession frequencies. Having the traceless stress tensor $\boldsymbol{\pi}$**,** the NTV torque quantity is calculated

$$\langle \mathbf{B}_{total,z} \cdot \boldsymbol{\pi} \rangle = \sum_{m,n} \Big\{ [f_{mn}(r)\Phi_{NTM}^{mn} + g_{mn}(r)\Phi_{NTM}^{mn\prime}] S_n^0 \big[(2-s)\Phi_{TM}^{mn*} + r\Phi_{TM}^{mn'*}\big] \quad (1)$$

$$\left. + \sum_{\substack{j=-3 \\ j\neq 0}}^{3} h_{mnj}(r, S_n^0, S_n^2)\Phi_{NTM}^{mn\prime}\left[(2-s)\Phi_{TM}^{m+j,n*} + r\Phi_{TM}^{m+j,n'*}\right] + \bar{h}_{mnj}\big(r, \Lambda_{|j|}, \Lambda'_{|j|}, \Lambda''_{|j|}\big) S_n^0 \Phi_{NTM}^{mn\prime}\Phi_{TM}^{m+j,n'*} \right\}$$

All the coefficients are analytically derived. $\Lambda = 1/[1 + \varepsilon(2\kappa^2 - 1)]$ is a parameter depending on the trapped bouncing particles pitch angle, κ. The above perturbed fluxes $\Phi_{(N)TM}^{mn}$ are related to our calculated perturbations $\Psi_{(N)TM}^{mn}$ by means of $\Psi_{(N)TM}^{mn} = (i/q_s)(m - nq_s)\Phi_{(N)TM}^{mn}$, where m and n are the perturbation mode numbers and q_s the corresponding magnetic surface safety factor. The outer and inner calculated magnetic island perturbed flux functions are [2]

$$\Psi_{TM}^{mn}(t) = A_s^{mn} + B_s^{mn} e^{-in\Omega_{err}t} + \sum_{p=1}^{6L} C_{ps}^{mn} e^{\tau_p t} \quad (2)$$

and

$$\Psi_{NTM}^{mn}(t) = \frac{1}{\tau_{FKR}^{5/4}} \left\{ \frac{A_s^{mn}}{\Gamma(9/4)} t^{5/4} - \frac{iB_s^{mn}}{n\Omega_{err}} \left[\frac{t^{1/4}}{\Gamma(1/4)} \left(4 + e^{-in\Omega_{err}t} E_{3/4}(-in\Omega_{err}t)\right) - \frac{e^{-in\Omega_{err}t}}{(-in\Omega_{err}t)^{1/4}} \right] \right. \quad (3)$$

$$\left. - \sum_{p=1}^{6L} \frac{C_{ps}^{mn}}{\tau_p} \left[\frac{t^{1/4}}{\Gamma(1/4)} \left(4 + e^{\tau_p t} E_{3/4}(\tau_p t)\right) - \frac{e^{\tau_p t}}{\tau_p^{\ 1/4}} \right] \right\}$$

A_s^{mn}, B_s^{mn}, C_{ps}^{mn} and τ_p are analytically derived functions of ideal plasma, wall, coils, error field (static and/or rotational) and initial perturbations parameters. Specific index notations are used [3]. Having (2) and (3) inserted into (1) we now are able to evaluate the NTV torque quantity. We have calculated it in the absence of any particles/plasma resonance in order to obtain results corresponding to usual operating modes. If the latter resonance would be considered the NTV effect would easily overcome the resonant EM effect. If we choose to compare our study to the experimental results from the Ref. [4] for AUG plasma toroidal rotations of about 35 kHz, our calculated results show a NTV torque that indeed has a lower effect compared to the resonant EM torque, but not so low as the experimental results seem to indicate.

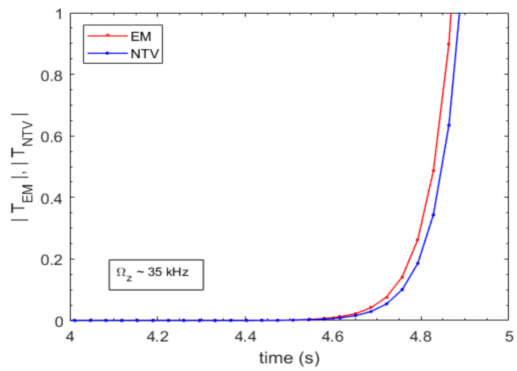

Figure 1: 3/2 EM versus NTV torques evolution at high rotation

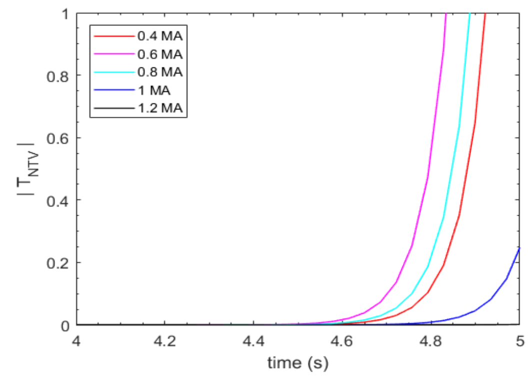

Figure 2: 3/2 NTV torque for different plasma currents

Figure 1 shows the normalized values of both torque quantities evolution. We have used the experimental data of #33959 AUG discharge. The absolute value of the both quantities is drawn. Both EM and NTV torques are negative, i.e. destabilizing.

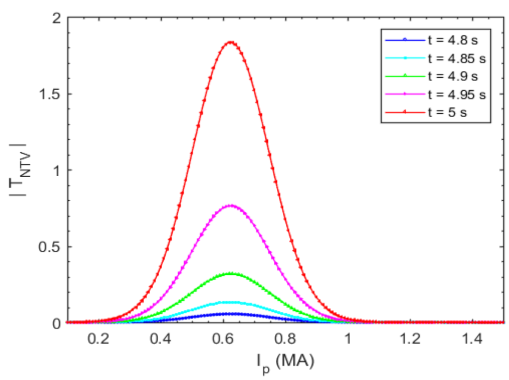

Figure 3: 3/2 NTV torque dependence of plasma current at fixed moments of time.

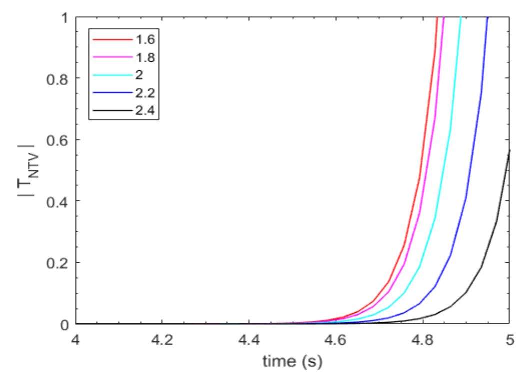

Figure 4: 3/2 NTV torque evolution for various plasma normalized β_N values.

The NTV torque is sensitive to the amplitude of the current injected into the plasma, as it can be seen in Figure 2. There is no monotone variation vs. the plasma current, therefore an extremum value exists corresponding to the maximum strength of the NTV torque. Figure 3 shows a current about 0.6 MA driving the maximum neoclassical viscosity effect for the 3/2 mode of perturbation case. On the other hand, Figure 4 indicates the decreasing NTV torque as the plasma normalized β_N increases. It seems that a higher plasma pressure prevents and mitigate the non-resonant coupling to strengthen. As expected, contrary to the EM torque case, we have found out that the NTV torque evolution is slightly affected by the B-coils generated currents or by the phase difference between the AUG rows of coils that usually have a higher impact on the resonant coupling mechanism between the plasma mode and the B-coils generated external perturbations.

References

[1] F.Porcelli, R. Stankiewicz and W. Kerner, Phys. Plasmas 1, 470 (1994).

[2] I.G. Miron, "Modelling of seed magnetic island formation", P2.060, 43rd EPS Conference on Plasma Physics, July 4-8 2016, Leuven, Belgium.

[3] I.G. Miron, Plasma Phys. Control. Fusion 50, 095003 (2008).

[4] S. Fietz et al, Nucl. Fusion 55, 013018 (2015).

ASSESSMENT OF THE EFFICIENCY OF SYNCHRONIZATION EXPERIMENTS IN TOKAMAKS BASED ON RECURRENCE PLOTS

T. Craciunescu[1], A. Murari[2,3], E. Peluso[4], M. Gelfusa[4]

[1]*National Institute for Lasers, Plasma and Radiation Physics, Bucharest-Magurele, Romania*
[2]*Consorzio RFX (CNR, ENEA, INFN, Universita' di Padova, Padova, Italy*
[3]*EUROfusion Programme Management Unit, JET, Culham Science Centre, Abingdon, UK*
[4]*Associazione EUROfusion—University of Rome "Tor Vergata", Roma, Italy*

WPJET1-C

The time series analysis and the determination of causal-effect relationship represent an important topic in various fusion plasma studies like: i) the investigation of instabilities, including the assessment of disruption causes, ii) the study of plasma dynamics and of the impurity control, particularly important since the installation of the new ILW iii) the L-H transition, for which several models have been proposed but a dynamical theory is still unavailable.

ELMs play a crucial role in present-day tokamak operation and their control is a very important factor for the development of reactor scenarios. Moreover, the Type-I ELMy H-mode has been chosen as the standard operation scenario for ITER. The control of ELMs is very important as they determine a significant reduction of the energy confinement. The confinement degradation, which occur during a time interval of the order of a millisecond, leads to significant particle expelling and to a large heat deposition on the vessel wall. At the scale of the next generation of devices these phenomena will determine an unacceptable vessel wall erosion level. Various forms of ELM pacing based on external perturbations, have been proposed. One of the most promising is the pacing of ELMs by injecting small pellets of frozen fusion fuel into the plasma edge at high frequency [1]. An illustration of the time series describing the sequence of ELMs and the pellet injection is presented in Fig. 1. In order to determine the efficiency of the control method it is therefore important to assess the synchronization of the two time series. The main difficulty of the problem resides in the fact that ELMs are quasi periodic phenomena. After a sufficiently long time interval the ELMs will reoccur independently on pellet injection, as a natural effect of the plasma dynamic. Therefore, the evaluation of the effectiveness of ELM pacing techniques should determine the time interval when their triggering effect has a real effect.

An approach based on recurrence plot [3] has been developed. Recurrence plots construct a sparse binary matrix from a time series in order to allow the easy visualization of the information that characterizes the behavior of trajectories in the phase space. Each time when the trajectory is visiting roughly the same point in the phase space is marked in the recurrence plot matrix by a unit value:

$$R_{ij}(\epsilon) = \Theta\left(\varepsilon - \left\|\overrightarrow{x_i} - \overrightarrow{x_j}\right\|\right), i, j = 1, \dots, N \qquad (1)$$

where: $\overrightarrow{x_i}$ and $\overrightarrow{x_j}$ are the point in phase space, i and j indexes the corresponding time points, N is the total number of points, ε is a threshold defining the size of the neighborhood and $\Theta(x)$ is the Heaviside function. A multivariate extension of RP is the joint recurrence plots (JRP). For two sub-systems characterized by independent RPs, the joint recurrence plot is defined as their Hadamard product. An example for a discharge devoted to ELM pacing is presented in Fig. 2

Besides allowing the visualization of the dynamical system periodicities, RPs allow the definition of several quantities indicators. The indicators are constructed starting from the distribution of diagonal, vertical and horizontal lines appearing in the RP. In this paper this recurrence quantification analysis (RQA) is performed by mean of the entropy of the diagonal length which is defined by the following relation:

$$ENTR = \sum_{l=l_{min}}^{N} p(l) ln\, p(l) \qquad (3)$$

Where $p(l) = \frac{P(l)}{\sum_{l=l_{min}}^{N} P(l)}$. The definition of ENTR is based on the frequency distribution of the diagonal lengths in the RP. Therefore it accounts for the complexity of the RP with respect to the diagonal lines. For uncorrelated noise (low complexity) ENTR has small values while for RPs developing an increased number of longer diagonals ENTR has higher values.

RP requires the calculation of a distance. The most used approach is based on the Euclidean distance, due to its simple geometric meaning and its straightforward implementation. However, the experimental data is always affected by noise and can include outliers. In order to cope with this problem we have recently proposed [3] to use the Geodesic Distance on Gaussian Manifolds (GDGM), which takes into account intrinsically the additive Gaussian noise accompanying the experimental data. In the view of the GDGM concept the individual measurements are interpreted as Gaussian distributions. Therefore a Gaussian probability density function (pdf), characterized by a specific mean μ and standard deviation σ, can be associated to each point in the time series data. In this view the distance between two time series points is the distance between the corresponding Gaussian distributions.

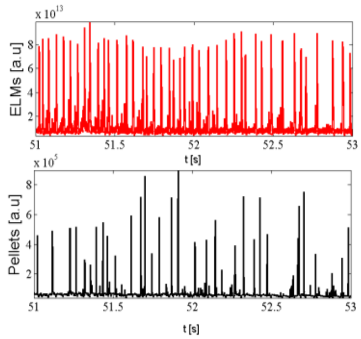

Illustration of ELM and pellets injection time series: Dα signals identifying the occurrence of ELMs (top) and Dα signal showing the time slices when the pellets enter the plasma (bottom).

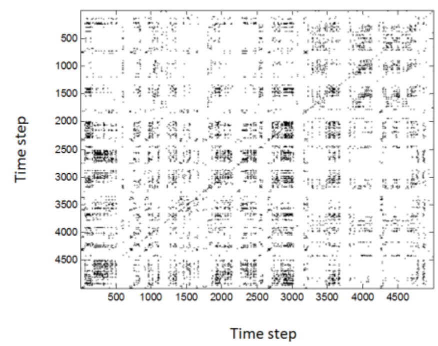

Fig. 2. Example of recurrence plot for discharge 82439 devoted to ELM pacing with pellets.

The methods based on RP has been tested on JET discharges with sufficient statistics and for cases when plasmas are sufficiently stationary. The time series used in the experiments rely on the measurement of the Dα emission, which has been used to determine both the occurrence of the ELMs and the arrival time of the pellets in the plasma. The results obtained are consistent with An illustrative example is presented in Fig. 3. RP identifies two lag times (2.9 ms and 3.7 ms) corresponding to maximum efficiency of pellets triggering. The result is consistent with those provided by other methods [4]. It shows also that the time resolution allows the detection of two phases during a single shot.

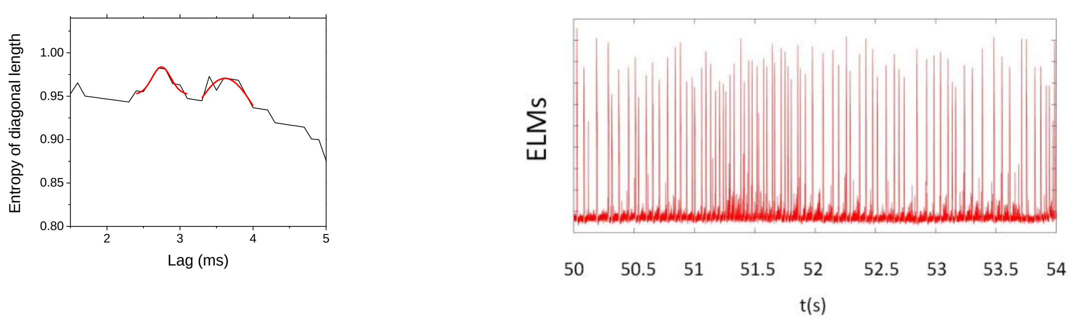

Evolution of RP entropy of diagonal length (left) for the JET discharge 82854. The peaks fitting is indicated in red. The two different phases of this discharge can be identified visually on the D⍰ plot - a phase of increased frequency appears around about 51 and 52 ms. (right).

References

[1] P.T. Lang, et al, ELM pacing investigations at JET with the new pellet launcher, Nucl. Fusion, 51, 033010 (16pp), 2011

[2] N. Marwan, et al, "Recurrence plots for the analysis of complex systems", Physics Reports vol. 438, pp. 237– 329, 2007.

[3] T. Craciunescu, A. Murari, Geodesic distance on Gaussian manifolds for the robust identification of chaotic systems, Nonlinear Dyn., Vol. 86, no. 1p 677–693, 2016.

[4] A. Murari et al, Application of transfer entropy to causality detection and synchronization experiments in tokamaks, A. Murari et al 2016 Nucl. Fusion 56 026006 2016 Nucl. Fusion 56 026006

POST-MORTEM ANALYSES OF SELECTED SAMPLES CUT FROM TILES EXPOSED TO JET PLASMA

E. Grigore, C.P. Lungu, C. Porosnicu, C. Ruset, M. Gherendi, I. Tiseanu, M. Lungu, I. Jepu, O.G. Pompilian, P. Dinca

IAP - National Institute for Lasers, Plasma and Radiation Physics, INFLPR

WP-JET2_P

The activities carried out by IAP in the framework of WPJET2 project were in accordance with the Project Management Plan (PMP). The main results corresponding to project deliverables for 2017 are synthesized below.

1. Sectioning of selected Be tiles from the JET wall into pieces for surface analyses (IBA, TDS, SIMS and metallography)

A number of tiles were cut in small parts in order to be analyzed by IBA, TDS, SIMS and metallography. Some of IBA measurements were performed by Iva Bogdanovic, RBI, Croatia and Rodrigo Mateus from IST, Portugal, and were compared with TDS measurements. The metallographic analyses show a very clear Ni layer and eroded or melted beryllium deposited as top layer of marker tiles.

2. Sectioning of W lamellas from Tile 5 retrieved from JET divertor

W Lamellae (A23, C3, C13, C14, C22, C23 and A02 – a non exposed lamella) were cut with a dedicated milling machine using a diamond cutting edge disc. The temperature during cutting was monitored and kept below 50 °C. The cutting plans for W lamellae were drawn by CCFE. SEM analyses on the samples surfaces revealed zones with high quantity of redeposited material as sample 13 from C13 marker lamella and melted/eroded zones on the other analized samples.

3. Cutting the Inconel *IWC* tile

An Inconel exposed tile (IWC-106) and a similar one unexposed were cut using the special cutting machine and a hardened blade. The temperature during cutting was monitored and kept below 40 °C. Samples were delivered in due time to CCFE. The detailed cutting plan was issued in collaboration with the CCFE specialists (Anna Windowson and Ionut Jepu).

4. TDS of samples cored from W-coated tiles

A number of four samples cored from W-coated tiles were measured using thermal desorption spectroscopy (TDS). The measurements for each sample were made at a base pressure of $3 \cdot 10^{-8}$ mbar, rising temperature with a rate of 10 K/min. up to 1323 K. The main desorption of deuterium occurred between 500 K-1000 K. A maximum content ($7.96 \cdot 10^{17}$ of D atoms) was found in the sample 14ING1C poz 8d and a minimum content was found in the sample 2BNG4C poz 6d ($7.81 \cdot 10^{16}$), both from the (2012-2014 campaign).

5. XRD and TDS analyses of the Be samples sectioned from JET tiles

XRD analysis on samples cut from Be limiters were performed using a Rigaku system (CuKα radiation) with parallel beam optics. XRD spectra revealed two distinct composition patterns on the limiters plasma-facing surfaces: pure Be in the erosion zone and Be-W, Be-Ni, Be-Cr, Be-O mixed compounds (Be_2W, $Be_{12}W$, $Be_{22}W$, BeNi, Be_2Cr, BeO) on the curved surfaces. XRD measurements performed on sample 182 revealed besides BeNi, Be, BeO compounds the presence of: CrO_2, and Fe_3O_4 oxides and Be_2Cr intermetallic compound.

TDS measurements on samples taken from Be limiters exposed to the fusion plasma were performed using a heated quartz tube which was in direct link with a Pfeiffer Vacuum Quadrupole Mass Spectrometer (QMS). The main desorption of deuterium occurred between 600 K-1000 K reaching its maximum in most cases around the temperature of 800 K. This high temperature of release for deuterium indicates that all samples have traps with high binding energy. These defects were produced most likely due to irradiation damage. Additionally a series of small peaks were observed in the temperature range of 1000 K-1200 K. For particular samples (335, 182, 228, 234, 270) a relative sharp increase in the deuterium desorption rate started at 1200 K. This could be attributed to defects from the bulk just beneath the damaged area, because deuterium can diffuse deeper into the bulk at higher temperatures. The lack of low temperature peaks below 625 K proves that the deuterium and tritium removal procedure employed (heating the walls at 623 K) is very efficient preventing deuterium trapping and accumulation in low energy binding states.

6. GDOES depth profiles of the elements, including deuterium, into the W-coated samples exposed to JET plasma

The specific objective for this task was to determine the depth profile of D, together with the other elements (W, Mo, Be, C and O), into the depth of W coatings exposed to JET plasma. Since the reference samples for D calibration are not available on the market these samples had to be produced in our laboratory and then used to calibrate the D channel of the GDOES machine.

A number of 5 samples (Φ7 x 10 mm) cored from JET divertor tiles exposed during 2011-1014 (14IN G1C, 14BN G6D) and 2012-2014 (2IW G3A, 14ON G7A, 14ON G8A) campaigns were analyzed by GDOES. The influence of plasma exposure on the structure of the W/Mo coating in particular locations of the divertor tiles where the samples are cored from was investigated. Special attention was paid to Be deposition and penetration through the carbon fibers and to D depth profile into the W/Mo coating. The results were correlated with the GDOES depth profiles measured on the Ti witness samples coated in 2009-2010 together with the divertor tiles installed in JET. The following aspects can be emphasised:

- Be has contaminated both inner and outer divertor tiles, but clearly a strong deposition of Be occurred on Tiles 1 and 3.
- The thickness of Be layer varies from about 2 μm on Tile 8 to about 44 μm on Tile 3.
- The maximum concentration of Be is on the surface (or near to the surface) where from it drops gradually to the substrate. This maximum was about 90 at.% for Tile 1 and Tile 3, and only 55 at.% for Tile 8.
- It is difficult to say that there is an erosion of the outer divertor (Tile 7 and 8). After three years of operation (2011-2014) the outer W layer of the marker tiles is still in place. It was covered by Be, more on tile 7 and less on Tile 8, but it seems that it was not removed. The outer Mo layer is in place too. On the other hand it is true that the strike point was not so much on Tile 7.
- D penetrates into the coating, but its profile does not seem to follow that of Be. On the Tile 3 where the Be deposition is very strong, the deuterium concentration is the lowest (0.2-0.6 at.%). On the Tile 8 with the lowest Be deposition, the D concentration is highest (3.2 at.%). Small peaks of D can be seen at the interfaces.
- It is important to notice that the concentration of D found by GDOES is in very good agreement with those found by Matej Mayer by NRA. He found D concentrations in the range of 1 – 3.5 at.%.

7. Supplementary work, Determination of erosion on Tile 5 during the ILW-2 campaign

The W layer thickness on marker lamellae from Tile 5 exposed to JET during the second ILW campaign (ILW-2) was measured by micro-beam X-ray fluorescence (µXRF). The principle of the method is to correlate the attenuation of the Mo interlayer Kα characteristic line with the thickness of the W layer. The method was calibrated with W/Mo reference samples produced by Combined Magnetron Sputtering and Ion Implantation technique and also by Monte Carlo simulation of X-ray line production and attenuation.

Before plasma exposure the W layer thickness on W/Mo markers measured by µXRF was in the range of (3.6 $\pm$ 0.2) x 10^{19} at./cm^2. This was in very good agreement with the GDOES measurements: 5.6 μm W and 6 μm Mo. After plasma exposure the same markers were analyzed on lamellae from stacks A, B, C and D from rows 2, 13 and 22. The results were compared with those obtained on the same lamellae by Rutherford Back Scattering (RBS). The beam spot size at RBS was about 1 x 1 mm while µXRF was performed with an X-ray beam with the diameter of about 20 μm.

The following comments can be made. No significant erosion was measured on the lamellae from row 2, on lamellae from stacks A and B on rows 13 and 22. An erosion of about $1\cdot10^{19}$ at./cm^2 (1.6 μm) was detected on lamella from stack C, row 13 and on lamella from stack D, row 22. More erosion (about 2.4 μm) was measured on lamella from stack C, row 22 and about 3.2 μm on lamella from stack D, row 13. The erosion was correlated with the position of the outer strike point that in this campaign was mainly on stacks C and D. These results are in good agreement with those obtained by RBS.

Methods for complex investigation of fusion materials

E. Grigore, C. Ruset, M. Gherendi, C. Lungu, C. Porosnicu, O.G. Pompilian, P. Dinca, B. Butoi, I. Tiseanu, M. Lungu

IAP- National Institute for Lasers, Plasma and Radiation Physics, INFLPR

WPJET2-C

The activities performed within the framework of this project are in the support of the *IAP* (Romanian Eurofusion Research Unit) activities carried out in the *WPJET2* project. The *WPJET2* project is aimed to study the impact of the new *ILW* configuration on the Plasma Facing Components (*PFC*) from the material perspective.

The present project aims to approach the following issues:

- To extend the capabilities of *GDOES* equipment in order to include deuterium (D) in the list of elements available for quantification and to implement *GDOES* as a method for depth profile measurements of D,
- To implement a method to measure the tritium content on the surface of sectioned samples at *IAP*
- To optimize and to use *microXRF* (X-ray fluorescence) technique for investigation of samples exposed to fusion plasma.

In order to address the above mentioned objectives few activities were performed at this stage of the project. The main activities and results are summarized below.

I. Production and characterization of D containing coatings

The implementation of Glow Discharge Optical Spectrometry (*GDOES*) as an instrument for Deuterium (D) depth profile measurement for samples sectioned from Plasma Facing Components (*PFC*) exposed to fusion plasma implies the calibration of the spectrometer for D quantification. The calibration process uses D containing samples produced in the form of coatings with different D inclusions. Different deposition methods and coatings type have been tested in order to get samples with a wide D content, uniformly distributed within the coatings. The experiments showed that a good candidate that has a high retention capability for hydrogen and its isotopes is Zr. Combined Magnetron Sputtering and Ion Implantation (*CMSII*) method has been used for deposition of Zr+ D coatings whereas High Power Impulse Magnetron Sputtering (*HiPIMS*) method has been used to produce W+D coatings.

Thermal Desorption Spectroscopy (*TDS*) was used as the main instrument in initial characterization of the coatings. This method supplied quantitative information about D content within the coatings. The *TDS* experiments indicated that for Zr+D coatings the D released is proportional with the D flow rate used in the deposition process. The D starts to be released from the Zr coatings at ~400^0 C and reached a maximum at ~ 800^0 C. For the W+D coatings obtained by *HiPIMS* it was observed that the deposition parameters affect the D and Ar retention in the following manner. A low duty cycle of the *HiPIMS* discharge supports the gas retention (both Ar and D). The difference in D and Ar release (in terms of pressure) is about 2 orders of magnitude at high duty cycle. It was also noticed that increasing the pulse length leads to a shift of the Ar release temperature up to 850^0 – 900^0 C.

The *NRA* measurements indicated for the W+D coatings obtained by *HiPIMS* a maximum D content of 10 at. %.

II. Tritium content determination in metallic samples by total combustion

Tritium content determination on metallic specimens was performed using the following procedure: oxidizing the samples in two stages, quantitative retention of the resulted tritiated water vapours and determination of collected water activitiy in a measure chain with liquid scintillator counting (*LSC*).

The samples were inserted in a tandem of 2 tubular ovens with digital control of thermal regime. The first oven is dedicated to sample degassing/ calcination / oxidation (programmable temperature in the range 200^0 C- 1000^0 C). The second oven, that contains a catalytic bed of CuO wires, has to totally oxidize the combustion/calcination gases resulted in the first stage and has a constant thermal regime of 800^0 C. The tritiated water resulted was collected in bubbling ampoules and measured using a tritium monitor with ion chamber RS400-HTO. A liquid scintillator spectrometer *TRICARB TR2800* measured the activity of radionuclides, low energy beta emitters. Measuring range was 1 - 16000 Bq and maximum detection efficiency of 55%. Specific activities obtained by total combustion of 10 analyzed metallic samples are shown below.

Table 1 Specific activities obtained by total combustion of the analyzed metallic samples

ID FI	*Sample code*	*Sample weight (g)*	*SL content (Bq)*	*A LSC (Bq)*	*A LSC with low (Bq) content*	*A/Sample (Bq)*	*Mass activity (Bq/g)*
1	355	0,1249	0,592	83,640	83,048	1245,720	9973,739
2	295	0,5699	0,441	44,499	44,058	660,870	1159,624
3	366	0,9669	0,526	211,666	211,140	3167,100	3275,520
4	350	0,4167	0,440	277,814	277,374	4160,610	9984,665
5	309	0,5108	0,550	451,315	450,765	6761,475	13237,030
6	289	0,1147	0,368	15,772	15,404	231,060	2014,473
7	274	0,5077	0,459	157,110	156,651	2349,765	4628,255
8	262	0,4300	0,382	25,601	25,219	378,285	879,733
9	196	0,4386	0,360	36,305	35,945	539,175	1229,309
10	188	0,4549	0,458	68,115	67,657	1014,855	2230,941

III. Validation and calibration of the microXRF measurement method applying Monte Carlo simulations for the X-rays production and the transport

The X-ray fluorescence (*XRF*) method has the main advantage, over other complementary methods, of being non-destructive regarding to the investigated samples. In this reporting period optimization studies of the *XRF* geometry with calibration standard samples and Monte Carlo numerical simulations of the generation and transport of characteristics X-rays were performed. The main goal of these studies was the quantification of the matrix effects and fluorescence saturation curves that are necessary in the interpretation on the experimental data. Calibration curves that correlate the layer thickness of the coating with the substrate material and X-ray lines yields were determined.

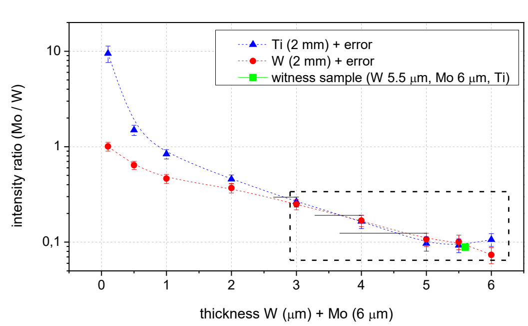

Figure 1 - K Mo/L W line intensities in relation to W layer thickness

Monte Carlo simulations were particularly useful for the evaluation of the W thickness in a W coating with Mo interlayer on bulk substrates. The ratio of W L lines and Mo K line is correlated with the W layer thickness (*figure 1*). The influence of the substrate material is perceptible at thin W layers. The simulation curve was experimentally confirmed for a layer structure of W 5.5 µm , Mo 6 µm on a Ti substrate.

These results will be used in the mixed *ITER*-like materials (W, Be or steel) erosion studies

JET GAMMA-RAY SPECTROMETER UPGRADE (GSU)

T. Craciunescu[1], V. Braic[1], D. Croft[2], M. Curuia[1], V. Kiptily[2], R. Lucock[2], R. Naish[2], S. Soare[1], V.L. Zoita[1]

[1]Institute of Atomic Physics, Bucharest, Romania
[3]CCFE, Culham Science Centre, Abingdon, United Kingdom

WP-JET4

The upgrade of the beam–line for the JET tangential gamma–ray spectrometer (KM6T in JET nomenclature) consisted in the design, manufacturing and installation of a complex system of shields and attenuators for both neutron and gamma radiations in order to maximize the signal-to-background ratio at the spectrometer detector. The resulting Radiation Field Components Assembly (RFCA), will contribute also to the improvement of the definition of the spectrometer Field-of-View. This major KM6T upgrade has involved the following activities:

- Manufacture and installation of additional modules for KM6T Tandem Collimators in order to fulfil the requirements for DT operation;
- Design, manufacture and installation of gamma-ray shields for minimizing the flux of parasitic gamma radiation reaching the detectors;
- Design, manufacture and installation of a set of lithium hydride (LiH) neutron attenuators with the aim of reducing the fast neutron flux at the gamma-ray detector position.

The KM6T components at the gamma-ray detector end of the spectrometer beam-line are shown in Fig. 1. The gamma-ray source (plasma) is on the left at about 25 m. The figure represents a vertical cross-section through the KM6T beam-line axis showing from left to right: KX1 X-ray spectrometer vacuum chamber, movable gamma-ray shield with the associated neutron attenuator, fixed gamma-ray shield, two internal attenuators, gamma-ray detector on the detector holder, mild steel shielding discs, HDPE shielding plug, concrete beam dump.

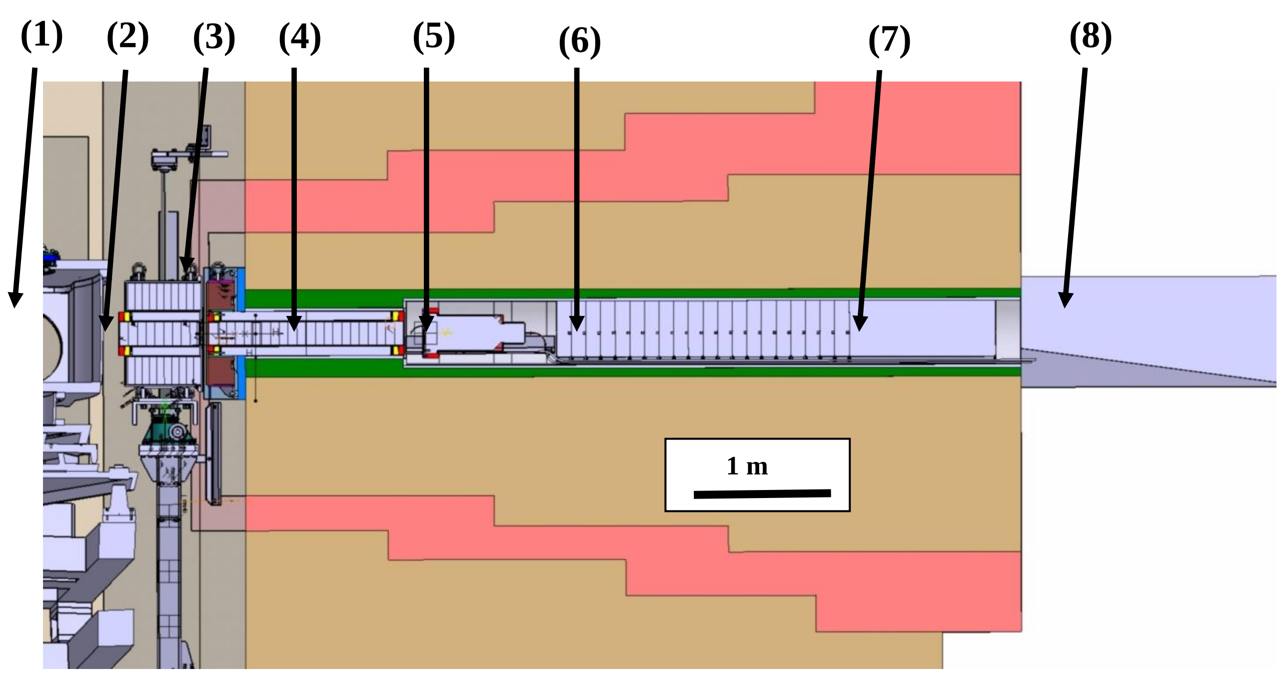

Figure 1. KM6T components at the detector end of the spectrometer beam-line.
KX1 X-ray spectrometer vacuum chamber (1), movable gamma-ray shield with the associated neutron attenuator (2), fixed gamma-ray shield (3), two internal attenuators (4), gamma-ray detector on the detector holder (5), mild steel shielding discs (6), HDPE shielding plug (7), concrete beam dump (8).

The gamma-ray shields (one movable and one fixed) and a set of three LiH neutron attenuators have been manufactured during the first half of 2017. The movable gamma-ray shield together with an external neutron attenuator is remotely operated by means of a jack system driven by and electric motor. The operation is performed through a command and control unit based on a Programmable Logic Controller (PLC).

The RFCA components have been pre-assembled at IAP (Figure 2) and a series of in-house operating tests have been successfully carried out prior to the delivery to JET in July 2017.

The installation at JET and preliminary testing of the Radiation Field Components Assembly for the KM6T gamma-ray spectrometer involved a long series of complex activities which addressed individually and collectively all the components and sub-assemblies presented above. Specific hardware and software activities have been dedicated to the installation and testing of the command and control unit for the movable gamma-ray shield and external neutron attenuator.

Extensive experimental tests have shown that the entire assembly operated locally from the control system installed in a dedicated cubicle in the J1D diagnostics hall performs according to the design requirements.

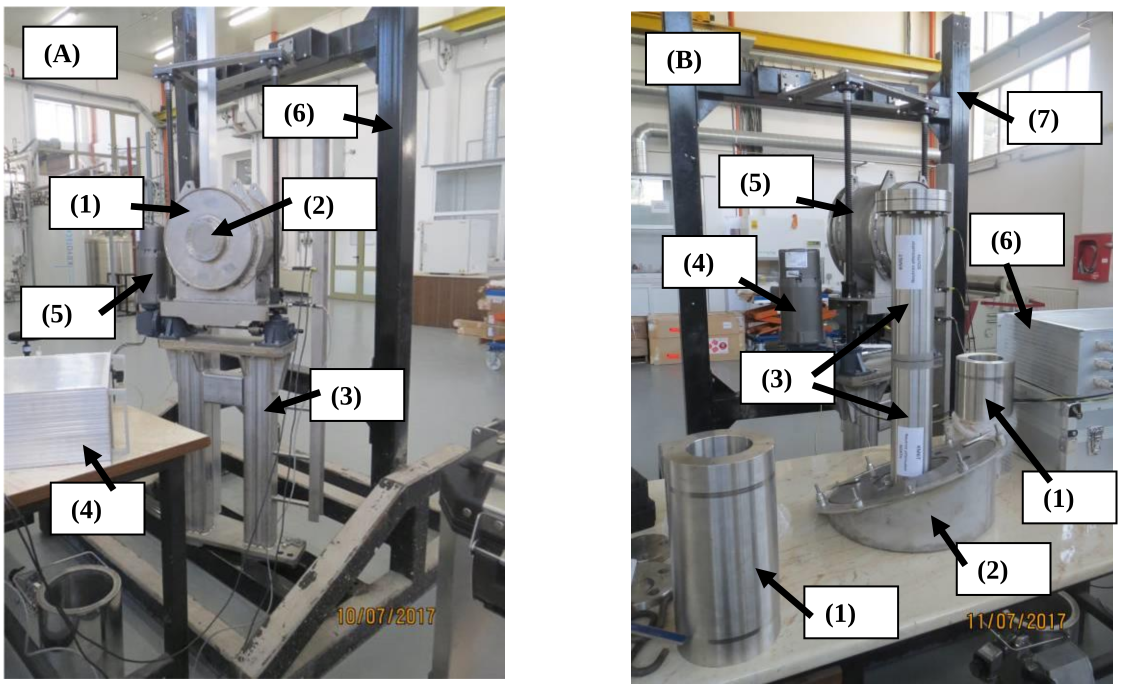

Figure 2 - Overall view of some RFCA components installed at IAP on the in-house test stand.
***(A)**: Movable gamma-ray shield (1); External neutron attenuator (2); Movable shield support (3); Command and control unit (4); Jack system electric motor (5); Test stand (6). **(B)**: Attenuator sleeves (1); Fixed gamma-ray shield (2); Internal neutron attenuators (3); Jack system electric motor (4); Movable gamma-ray shield (5); Control unit (6); Test stand (7).*

IAP Romania is coordinating the project consoritum which includes the following partners: CCFE UK, ÖAW Austria, CNR Italy, IPPLM Poland, IST Portugal, SFA Slovenia. The main achievements of the partners are: construction and installation of the detectors based on LaBr3 and CeBr3 crystals (CNR and IPPLM), construction and installation of the data acquisition system (IST), development of software for spectra visualisation, analyisys and PPF production (CNR), modelling of the time-dependent distributions of confined alpha-particles and intensity of alpha-induced gamma-emission and synthetic gamma-diagnostics code validation (OEAW and CCFE), estimation of the activation of components (SFA).

Tomographic examination of DEMO TF conductor prototypes

Ion Tiseanu, Daniel Dumitru, Teddy Craciunescu, Cosmin Dobrea, Adrian Sima, Mihail Lungu

National Institute for Lasers, Plasma and Radiation Physics, INFLPR

WPMAG-P

The superconducting magnet system of a fusion reactor is based on the Cable-in Conduit Conductor (CICC) which is a highly complex structure with packed, multistage twisted superconductor and copper strands in a cooling configuration. Using 3D X-ray tomography (XCT) which recently becomes quite effective in providing accurate geometrical parameters such as local void fraction, strand twisting pattern as well as their statistics. In the framework of Magnetic System Work Program (WPMAG), a numerical modelling and experimental activities for the optimization of the X-ray computer tomography technique where performed by Microtomography group of INFLPR. The numerical modelling consists of Monte Carlo simulation of the X-ray generation and transport in the tomographic configuration in order to assess the feasibility of X-ray CT analysis of relatively large structures of DEMO TF conductors. The superconductor/resistive joint were analysed for two different configurations with respect to X-ray source type and delivered energy. Thus, it was able to simulate several cases of deviation of strands microstructural integrity (defects) such as holes or pinched/deformed strands. The experimental activities were performed in order to optimize the examination by X-ray computer tomography of a new multi-stage CEA DEMO cable that is still in the development stage. An automated algorithm based on a photometric analysis was developed for strand detection and centroid estimation then applied on tomographic reconstructions. In addition, a technique to enhance the spatial resolution of the computer tomography analysis is developed with the aim to visualize the 3D microstructure of individual and triplets of Nb3Sn strands.

Monte-Carlo simulation of DEMO TF conductor tomography analysis

In 2017 a survey of X-ray tomography analysis and numerical modelling was conducted on the DEMO magnet system (ENEA -W&R and CEA). A feasibility study of XCT analysis of a TF joint sample that involves a ENEA DEMO TF conductor with a very high level of compaction was carried out by Monte Carlo simulation of the complete tomography configuration. It proved that X-ray computed tomography at energy beam over 300 keV is suitable for DEMO TF cables and joints inspection. The simulations cover different scenarios of deviation and microstructural integrity of the conductor.

Figure 1. Left: X-ray simulated spectra for 300 and 450 keV electron beams. Right: Photo of ENEA DEMO TF cable and its

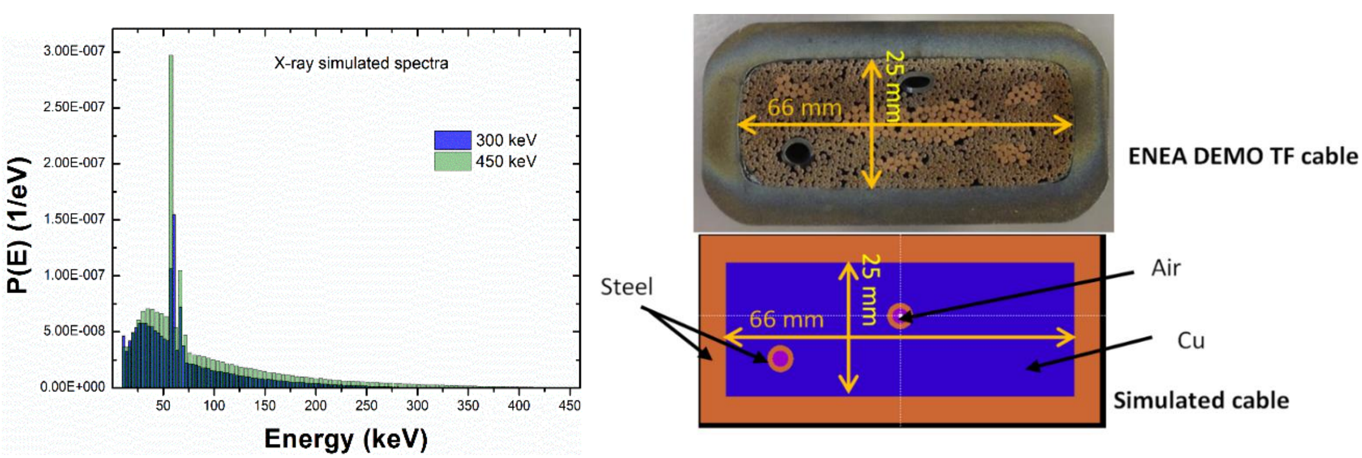

corresponding geometry simulation

Monte Carlo simulation of the X-ray generation and transport in the tomography configuration was performed using the code PENELOPE 2014.

The simulations were realised in two steps: 1) X-ray spectra were simulated for a tungsten target hit by electron beams of 300 and 450 keV, figure 1-left. The PENELOPE2014 code provides the X-ray spectra with characteristic tungsten lines which is very important for detailed simulation. 2) In the second step it was simulated the transport of photons in a tomography

configuration consisting in a microfocus X-ray source with the energy spectrum calculated at the first step. The simulation of the overall geometry of the ENEA TF cable is presented in *figure 1-right*. The numerical modelling was optimized in order to analyse a complex part of TF DEMO cable/joint which is the most difficult to penetrate by X-rays, considering that the results can also be applied to less complicated structure of TF joints. The geometry (*figure 1-right)* was used to verify the photons transmission trough the superconductor thick slab.
However, this geometry is not appropriate for strands inspection because the interior of the conductor is represented as homogeneous bulk of Cu. The simplified simulation of the cable represents an object of 2x2.5 cm thickness and is composed of 24 wires of 1 mm diameter which are embedded into homogeneous Cu material. To obtain a more detailed approach it was added 0.5 cm of steel jacket around Cu material. The detector was defined as a box of 9x9x0.05 cm made of gadolinium oxysulfide (GOS) and the X-ray source was defined as a cone beam with 5^o aperture. The simulation of defects detection was implemented for several possible configurations for both 300 and 450 keV electron beams. Comparing all the simulations, it was observed that for both tomography configurations it was able to identify the type of the defect based on the signal intensity. Furthermore, it was analysed the effect of the jacket thickness to the signal intensity. Reducing the jacket thickness from 0.5 cm to 0.25 cm for simulated TF cable, an increased signal was detected.

Structural integrity assessment of the CEA DEMO multi-stage cable by X-ray tomography

In 2017 a newly designed CEA DEMO multi-stage cable made of mix of soft and hard copper, without the exterior jacket, was available for XCT. In the current stage of fabrication, the cable is very favourable for X-ray computer tomography (XCT) analysis due to the absence of jacket which further reduce the SNR by increased X-ray absorption. Via image processing and photometric analysis, a strand detection and positioning algorithm was developed based on detection of local maxima and fitting on a 2D elliptical Gaussian distribution. This algorithm is very successful in strand detection, the rate of detection is very high (fig.2 c). With few adjustments, that are currently in progress, it is possible to accomplish a higher precision for 100% detection and localization of strands.

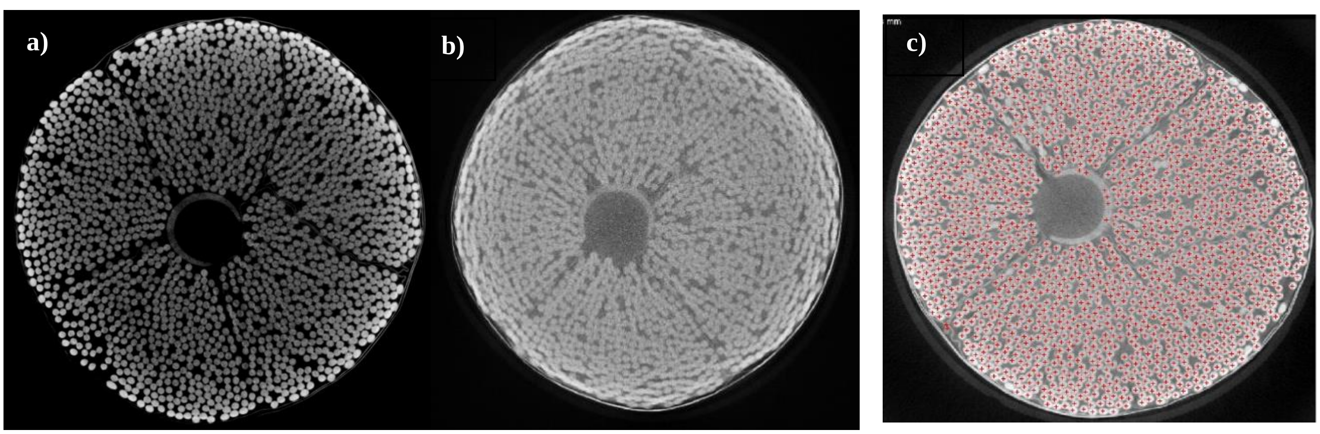

Figure 2. Tomography cross-sections of CEA DEMO multi-stage cable: a) low X-ray scattering; b) high X-ray scattering conditions; c) Application of the strand detection algorithm on the least favourable (high X-ray scattering) with >98% strands detection rate (red dots).

Development of high resolution tomography examination for the diagnosis of deformation of superconducting wires and cables subjected to mechanical tests

Ion Tiseanu, Teddy Craciunescu, Adrian Sima, Cosmin Dobrea, Mihail Lungu

National Institute for Lasers, Plasma and Radiation Physics, NILPRP

WPMAG-C

The aim of the current project was to obtain tomography reconstructions with micrometre –scale resolution of the high-performance superconductor strands that are developed for the fusion technology magnetic confinement system. Nb_3Sn superconductor strands were analyzed by combining the digital radiography with a TDI - Time Delay Integration detector (8192x256 squared pixels 27 µm) for non-homogeneity detection with *X-ray computed tomography* (XCT) technique (flat-panel detector 1929x1536 squared pixels of 75 µm) for in-depth investigation. The combination of the two methods is implemented within the X-ray microtomography laboratory of NILPRP (*Fig 1.a*).

Using the TDI detector in an XCT system is not practical for efficient tomography scans but it still presents the advantage of delivering good quality radiography images. Thus, a great number of manufacturing imperfections can be pointed out by means of TDI detector with a high accuracy (*Fig 1.b*).

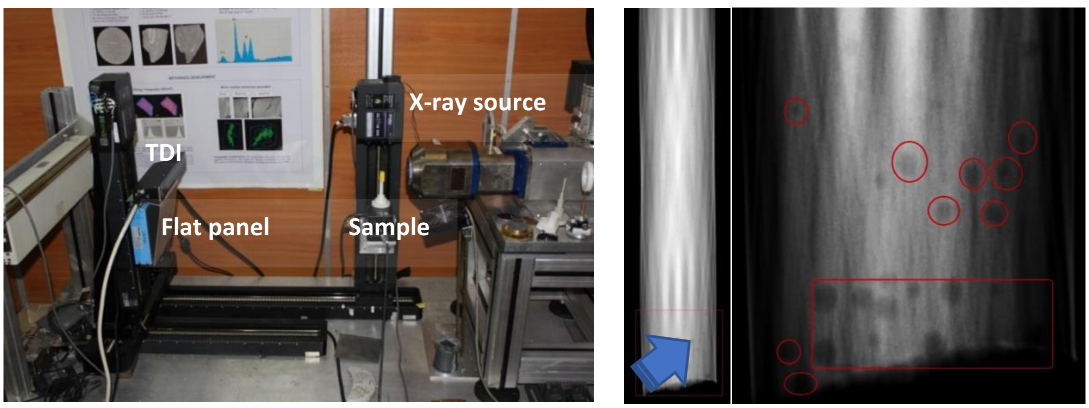

a) *b)*

Figure 1 – NILPRP XCT setup with TDI and flat panel (a); Digital radiography of a Nb_3Sn strand (b);

Fig 2 b shows that the tomographic image almost matches the accuracy of a SEM picture (*Fig 2.a*). The actual strand diameter of 1 mm is also precisely determined by coordinate measurement on reconstructed image (*Fig 2.b*).

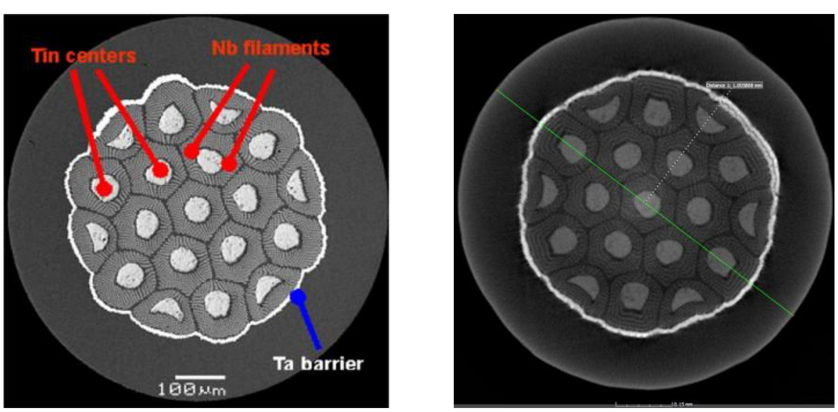

a) *b)*

Figure 2 - SEM image of Nb_3Sn strand (a); High resolution microtomography with space resolution similar to SEM images (b);

The XCT images also serve for defect detection as for example the small voids in the Sn deposits or the Ta barrier imperfections (*Fig 3*).

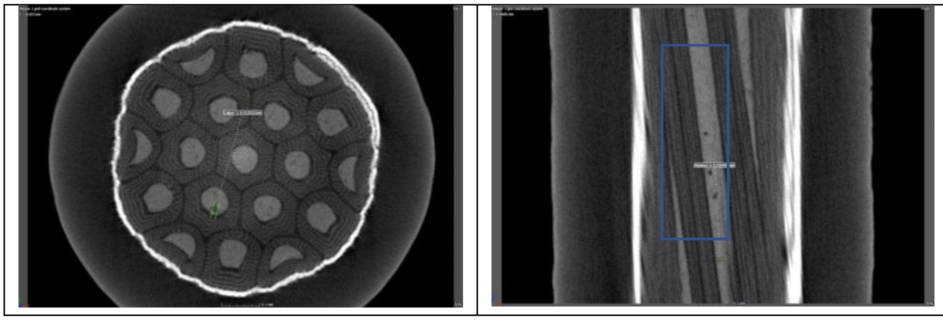

Figure 3 - Geometry imperfections visualized by XCT on a Nb_3Sb strand;

Further improvement of the space resolution is attempted in an extended FOV - Field Of View XCT measurement also known as asymmetric scanning technique. A symmetric scanning configuration implies that the X-ray source, the rotation axis of the scanned object and the middle of the detector are on the same imaginary plane. For an asymmetric scanning configuration, the detector is shifted for that the X-ray incidents beam to pass through half of the object. Therefore, the scanning process benefits from a new virtual detector with twice as much pixels per each line. The reconstructed images revealed that the asymmetric scanning technique has a better potential to increases the image contrast and the analysis resolution. As an advantage, the static noise accumulated from the XCT scanning remains the same as in a symmetric measurement configuration.

Comparisons between symmetric and enhanced FOV scans on individual and triplets of Nb_3Sn strands were made (*Fig. 4 a, b*). The triplet strands sample is formed by three WST-19 Nb_3Sn strands, joined together in a carbon fiber jacket that is highly transparent to X-rays. This configuration simulates a real winding scenario used for building strong magnets. In this case, the XCT scanning process requires a higher power applied on the X-ray source in order to penetrate the twisted strands.

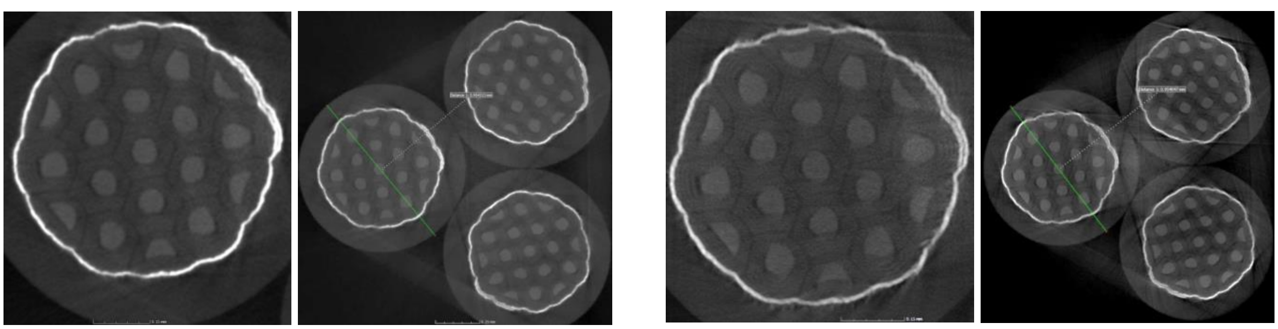

a) b)

Figure4 – Tomographic cross-sections of individual and triplet of strands for symmetric (a) and asymmetric (b) XCT scanning;

According to *figure 4 a, b*, for the symmetric scanning case (voxel resolution 1.36 µm), the image is slightly blurred due to poor resolution. However, the 19 Tin deposits and Ta barrier around are clearly visible. The images obtained by asymmetric scan (voxel resolution 0.66 µm) are noticeably sharper.

Conclusions

We report the microtomography analysis on individual and multiplets (triplet) of Nb_3Sn strands with an enhanced field of view scanning method. The triplet strands sample simulates a real winding scenario used for building strong magnets. The main objective was reached, that is, improving the voxel resolution to the point where inter-strand contact density could be reliably measured. The reconstructed images sustain that the asymmetric scanning technique has a better potential to increases the image contrast and the analysis resolution.

PROCESSING AND CHARACTERIZATION OF HIGH HEAT FLUX COMPOSITE MATERIALS

A. Galatanu[1], M. Galatanu[1], G. Ruiu[1], M. Enculescu[1], J. Reiser[2]

[1]*National Institute of Materials Physics, Atomistilor 405A, Magurele, Romania*
[2]*Institute for Applied Materials (IAM-AWP), Karlsruhe Institute of Technology (KIT), Eggenstein-Leopoldshafen, Germany*

WP-MAT

In 2017 our work was devoted to the development of various interface materials and joining technologies for the divertor heat sink components, as well as for thermo-physical properties characterizations for materials developed in the HHFM sub group. Important progresses have been achieved in both materials processing and joining techniques for W and Cu based heat sink materials. Concerning the materials processing, the main focus was on thermal barriers which have been produced not only with different planar shapes but also as ring shaped materials with a graded concentration. These can be implemented in W-monoblock divertor components. For potential W-based structural materials, various W-laminates have been produced and sent to our partners for investigations. The most important result for the moment is provided by the cross check performed at KIT on our FAST produced W-V laminates. Prolonged exposure at high temperature did indeed not shown the presence of Kirkendall effect (as also observed in our own investigations) and this suggest that our processing method might provide a better route for such materials.

W laminates are layered composites created from W and other metal thin foils, considered as possible structural materials for DEMO divertor. In this frame our work is focused on the fabrication of W laminates with different metals using a FAST route and the investigation of their structural and thermal properties. FAST joining of metallic materials is a technology which combines diffusion bonding and electrical point welding (due to discharges across contact surfaces on micrometric scale) on the whole contact surface at once, while the whole sample is heated by Joule effect. The main advantages of this techniques are its versatility concerning the sample shape and the process speed. However, as both our own results and those obtained by the KIT group have shown, a prolonged exposure of such layered composites to high temperatures (1000 hours at 1000 C) results in a strong intermixing of Ti with W and in a lesser manner of V with W. In addition, the KIT group has reported also a Kirkendall effect in the case of W-V laminates. These can be correlated to a decrease of mechanical properties, putting in doubt such a solution for future DEMO components. To elucidate possible material dependencies for W-V laminates between our and KIT results, we have reproduced the last year annealing experiments using current state of the art Plansee W foils. Similar specimens, produced in NIMP by FAST route have been also sent to KIT to cross-check the annealing effects.

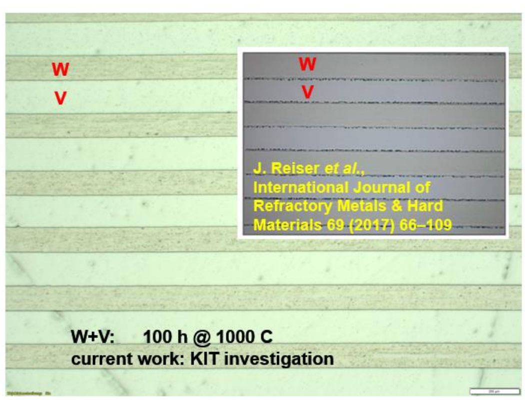

Figure 1. KIT analysis performed on W-V laminates produced by FAST and showing the absence of Kirkendall pores.

The cross-checking tests performed at KIT on these samples and using the same conditions previously used for KIT diffusion bonded samples show that no Kirkendall effect is present in the FAST processed samples. A relevant analysis picture is depicted in figure 3. Thus the absence of Kirkendall effect can be ascribed either to the joining method, or to the

V foils. In the next step we'll apply the FAST method on specimens produced with KIT foils to most likely exclude this possibility. On the other hand, previous work has shown that a thin Cr layer deposited on the W surface can prevent the inter-diffusion of W and Ti in case of prolonged exposure at high temperature of W-Ti laminates. Now we have produced such specimens with current state of the art Plansee W foils. Cr layers of about 150 nm have been deposited by RF sputtering on both sides of W foils and then these foils have been joined by FAST in an alternate order with Ti foils. These specimens have been exposed in NIMP at 1000 C for 1000 hours in vacuum and similar specimens have been sent to KIT for a cross-check experiment.

As interface materials for the divertor components, in 2017 the main focus has been on the improvement of thermal barrier materials in order to achieve lower thermal conductivities and ring shaped samples suited for the W-monoblock concept. Our thermal barrier materials are Cu-ceramic composites produced by SPS (spark plasma sintering). For such composites, the SPS phenomenology is complicated and difficult to quantify. If the volume fraction of metal is high, the current will flow through the metal increasing its temperature. Thus if the melting temperature of the metal is considerably lower than the melting temperature of the ceramic, the metal part will be overheated resulting in a catastrophic melt of the sample. On the other hand, if the ceramic volume fraction is high, one can expect that above a threshold ceramic concentration the sample will be in the best case only partially sintered (e.g. metal-metal connections and eventually metal-ceramic connections). This limitation was expected to occur also in the case of Cu-ZrO2 composites. To increase the composition range we have chosen to use nanometric oxide powders which should allow a better dispersion in the Cu matrix. As in the case of Cu-Al2O3 or Cu-Y2O3 composites, a maximum oxide concentration of about 50% volume was expected. Surprisingly, in the Cu-ZrO2 case, we have been able to consolidate specimens with ZrO2 volume concentrations up to 90 %. Up to a volume concentration of about 80% ZrO2 a SPS average temperature of 830 ºC can be used to obtain well consolidated materials. Higher temperatures can be used at lower ZrO2 content (like e.g. 930 ºC, up to 70%). The unexpected good sintering behaviour at high ZrO2 concentrations can be explained by the formation of honeycomb-like structure of Cu as shown in the left part of figure 2.

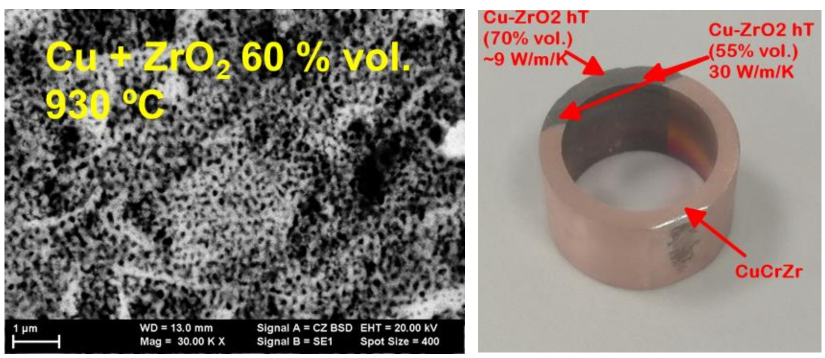

Figure 2. Morphology of Cu-ZrO2 composites with high oxide content (left) and a ring shaped thermal barrier based on such materials (right).

For the DEMO W monoblock divertor concept very low thermal conductivity values are needed and the Cu-ZrO2 composites can achieve easily values below 10 W/m/K in all the temperature range from RT to 1000 ºC. In this respect, the present materials outperform all the previous produced composites. Since the thermal barrier materials should be joined both to W armour and the CuCrZr heat sink it is desirable to have as thermal barrier a material able to mitigate the effects of the CTE mismatch in W and CuCrZr. The dilatometry measurement results show that these materials fulfil this criterion. One of the biggest advantages in having Cu in the thermal barrier composites is given by the fact that Cu can be easily joined to both W and other Cu alloys by various methods like diffusion bonding, brazing, FAST (field assisted sintering technique) joining or HRP (hot radial pressing, already used for ITER and DEMO divertor components. For low concentration Cu-ZrO2 thermal barriers a one step process can be applied, meaning to join together all 3 materials in a single run. However, for high concentration ZrO2 thermal barriers, in order to avoid the melting of either CuCrZr or/and Cu-ZrO2 material a two-step process is needed.

FEM-BASED OPTIMIZATION OF HEAT FLOW THROUGH DIVERTOR COMPONENTS AND DEVELOPMENT OF CHARCTERIZATION TECHNIQUES FOR HIGH HEAT FLUX MATERIALS

A. Galatanu[1], M. Galatanu[1], B. Popescu[1], C. Ticos[2], I. Tiseanu[2]

[1] *National Institute of Materials Physics, Atomistilor 405A, Magurele, Romania*

[2]*National Institute for Laser, Plasma and Radiation Physics, 077125 Bucharest, Romania*

WP-MAT

This complementary project aims to support our research unit activities in WP-MAT, developing investigation techniques and addressing both fabrication technology problems and materials behaviour under severe conditions, closer to that expected in a fusion reactor. In 2017 NIMP produced samples with specific geometries from W-metal laminates and W-thermal barrier-CuCrZr mock-ups for irradiation and samples of Cu based thermal barriers and Cu-W materials for XRCT experiments. In order to optimize the materials selection and components design simulations on the heat flow across W-monoblock divertor components have been carried out. P1-Ticos finished the development of the electron irradiation set-up and exposed to a pulsed 6 MeV electron beam layered composite samples made of W, Cu-ZrO2 and CuCrZr. P2-Tiseanu performed XRCT on various samples in order to improve the image contrast.

To achieve realistic conditions for HHF materials for irradiation and plasma jets test to be performed first by NILPRP project partners and then further by EUROfusion partners in WP-MAT, the samples must fulfil adequate conditions, related to shape, composition and properties. Here the most important aspect is related to the joints between different materials, because their failure or low performance might produce erroneous results for the materials investigated. In 2017 we have prepared multi-layered samples containing W, Cu-composites and CuCrZr-X alloys. The samples have been produced using SPS with the already established procedure.

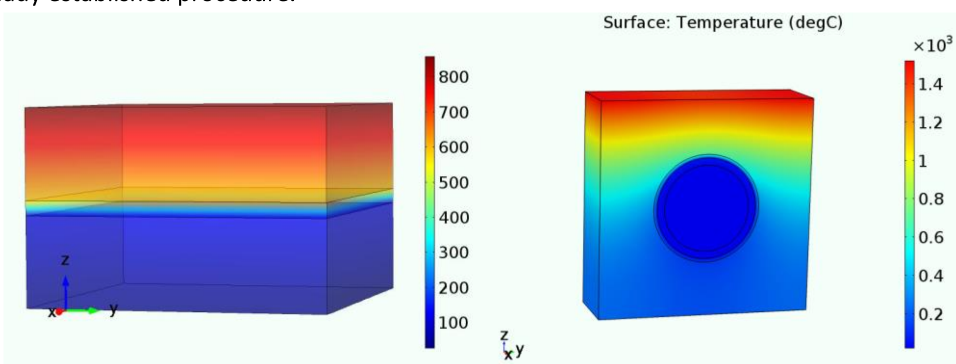

Figure 1. HHF test simulation compared with realistic DEMO conditions simulation

On the other hand, to realize realistic mock-ups for screening tests it is also important to simulate the component behaviour in realistic DEMO conditions. Using FEM simulations it is possible to analyse the heat flow and the temperature evolution in various conditions for the DEMO monoblock divertor components. Figure 1 illustrates the difference between a simple test mock-up produced for HHF tests (to be performed on NIMP samples in Julich) and realistic divertor conditions as resulting from the current DEMO design proposal for W-monoblock divertor.

Moreover, as shown in figure 2, such simulations are able to compare different geometric conditions and thus provide an input both in the design of thermal barrier material properties and mock-up construction design.

In the case of its divertor, an expected heat flux of about 10-20 MW/m2 should be extracted. Thus, a full W armour is considered as the most viable option, while the following heat sink part will be most likely constructed from Cu or ODS Cu alloys pipes, similar to the ITER full-W divertor design. W has a rather high ductile-brittle transition temperature (DBTT), around 300-400 °C as measured by impact bending tests. This value sets the lowest limit of its operating temperature window, while the upper limit can be derived from recrystallization constraints at about 1200 °C. In fact, the optimum operating temperature for W is considered to be around 800-1200 ºC, taking into account recovery considerations. On the other hand, for the heat sink materials CuCrZr alloys has a temperature operating window between 180°C and about 300°C.

The interface material between them should in an ideal case keep both materials in their respective operating temperature ranges and also compensate the large difference between the W and Cu thermal expansion coefficients (CTE). Thus it is important to analyse the divertor component behaviour in order to produce mock-ups as close as possible to the ideal design.

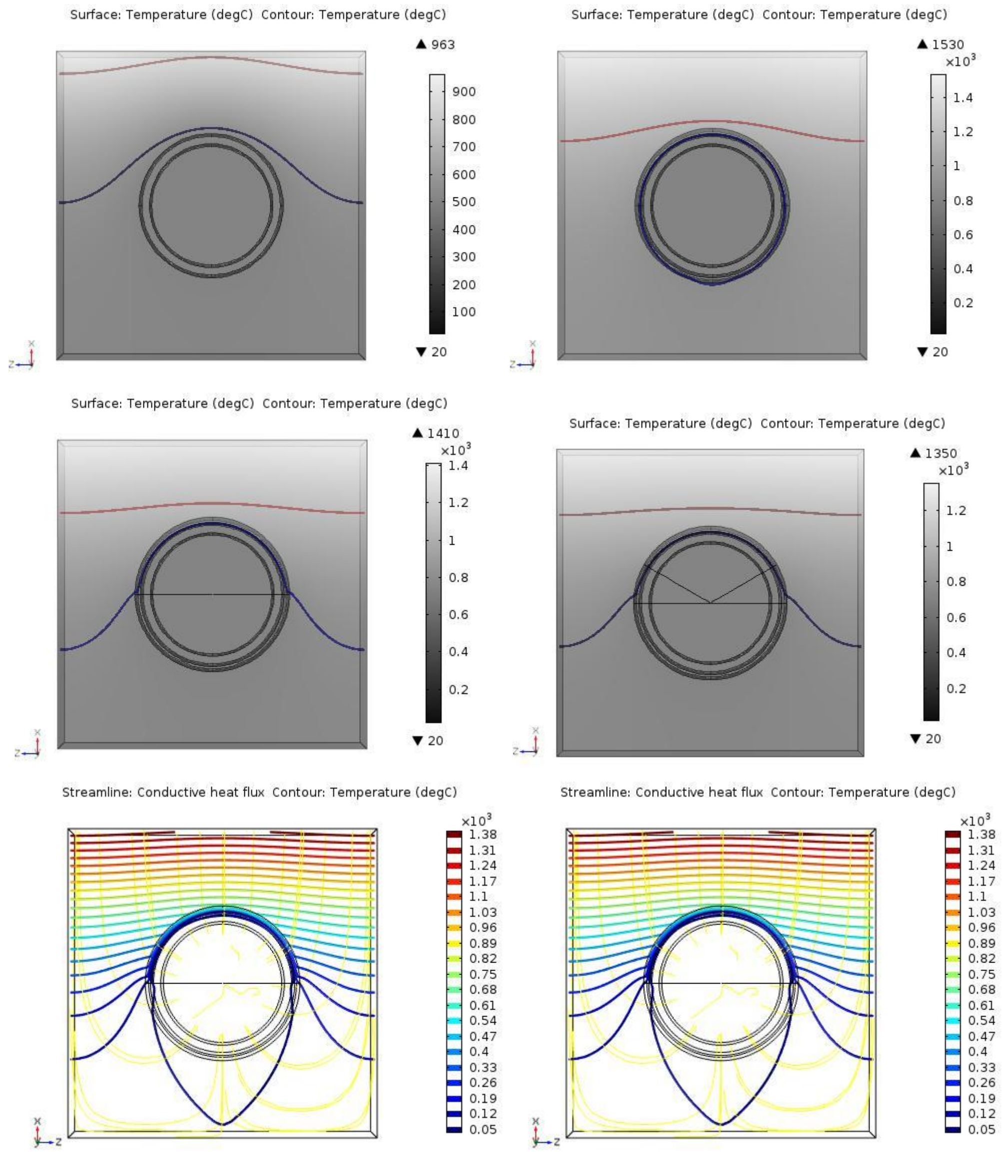

Figure 2. Simulation of the temperature behaviour of the DEMO monoblock divertor component under steady state conditions 10 MW/m2 and 150 C water active cooling. In the upper and middle panels, the blue line represents the 300 C limit and the red one represents thes 800 C.

As it can be seen from figure 2 (upper panel), in the absence of a TB interlayer, most of W will be below the optimum temperature. On the other hand, a full circular thermal barrier (with a thermal conductivity of 10 W/m/K) will keep both materials in the desired operating temperature windows, but the upper part of W will recrystallize due to the high surface temperature. A half circular barrier barrier will reduce the surface temperature at the price of having the lower part of W in a brittle state. Including different TB properties (like 10 and adjacent 30 W/m/K) can obviously improve the temperature distribution and then varying the geometric conditions the best option can be chosen. Of course it is very important to optimise also the thermomechanical stresses, which will require more sophisticated simulations to be performed in the next stages.

DEVELOPMENT OF IRRADIATION SET-UPS AND IRRADIATION OF BI-COMPONENT SAMPLES

C.M. Ticos[1], A. Galatanu[2], M. Galatanu[2], A. Scurtu[1], N. Udrea[1], D. Ticos[1], M. Dumitru[1], M.L. Mitu[1], I. Nicusor[1,2]

[1]National Institute for Laser, Plasma and Radiation Physics, 077125 Bucharest, Romania
[2]National Institute of Material Physics, Bucharest 077125, Romania

WPMAT-C

1.Irradiation of composite samples at the 6 MeV LINAC.

We exposed to a pulsed 6 MeV electron beam samples made of composites containing CuCrZr produced by our partner institution NIMP. The samples had a top layer of W followed by a layer of $Cu-ZrO_2$ acting as a thermal buffer and a third layer of CuCrZr (also called elmedur XS). The W layer had a thickness 0.5 mm for one sample and 2 mm for the second sample. We irradiated samples made of CuCrZr (Cu 98.9 %, Cr 1.0 %, Zr 0.1 %) with diameters 10 mm and 25 mm diameter, respectively, and a 5 mm thickness. The irradiation was carried out in air and in vacuum at 4×10^{-2} torr.

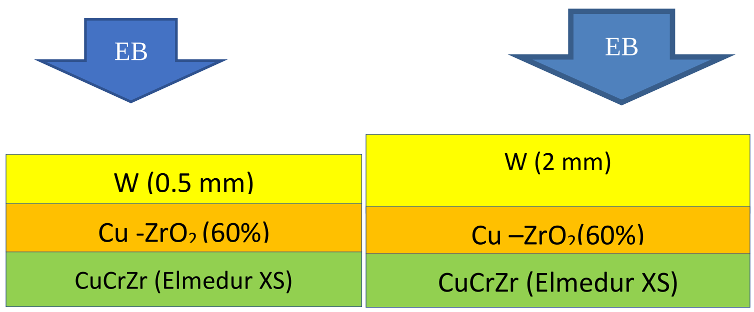

a) b)

Fig. 1. Exposure of the two composites to 6 MeV electron beam (EB): a) sample 1 with a top W layer with thickness 0.5 mm and b) sample 2 with a top W layer with thickness 2 mm.

The electron fluence measured with a Radiabeam Faraday Cup FARC-04-2M was ~1.3×10^{12} el/cm^2 per pulse. The LINAC operated at a frequency of 53 Hz. The irradiation time was set to 5 minutes corresponding to 15.9×10^3 pulses and a total cumulated fluence $\sim2.07\times10^{16}$ el/cm^2. Before and after the irradiation a SEM analysis of the W samples surface was carried out as presented in Fig. 2. An image of the rough surface of the sample before irradiation is presented in Fig. 2 a). Its aspect is arising from the process of fabrication with scratches all over the surface. After irradiation one can observe the formation of small holes over the full surface with diameters ranging from 60 to 125 nm, as shown in Fig. 2 b) whose resolution is 12.5 nm/pixel .

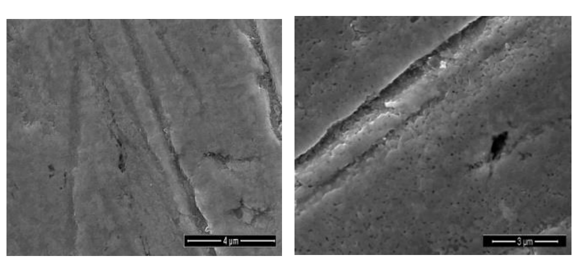

Fig. 2 High resolution images of sample 1 surface (W 0.5 mm-$CuZrO_2$-CuCrZr): a) before irradiation; b) after 5 min irradiation; nanometer- size holes are present on the irradiated surface.

2. Irradiation of CuCrZr at the 6 MeV LINAC.

We irradiated samples made of CuCrZr (Cu 98.9 %, Cr 1.0 %, Zr 0.1 %). The samples had diameters of 10 mm and 25 mm diameter and a 5 mm thickness. They were irradiated by an electron beam with energy 6 MeV in air and vacuum at

4×10^{-2} torr. The electron flux was 6.6×10^{14} el/cm^2 per minute of irradiation. Elongated structures are visible after irradiation as shown in Fig. 3.

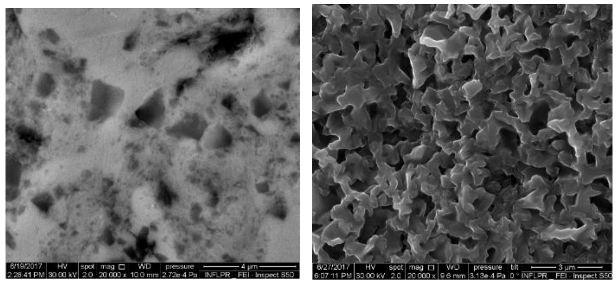

a) *b)*

Fig. 3 High resolution image of CuCrZr (Cu 98.9 %, Cr 1.0 %, Zr 0.1%) 10 mm sample surface before irradiation in a), and after 8 min of irradiation in b).

3. EDS analysis of samples made of sintered W exposed to plasma jet.

Exposure of samples made from pure (99.9 %) sintered W to plasma jets was carried out previously by our team. The samples with 12.5 mm in diameter were put in a dense plasma jet produced by a coaxial plasma gun operated at 2 kJ. We found that cracks and craters were produced in the surface due to surface tensions during plasma heating. Nanodroplets and micron size droplets could be observed on the samples surface. Initially these nano/microdroplets were thought to be made of W due to surface vaporization and rapid condensation. However, an energy-dispersive spectroscopy (EDS) analysis revealed that the composition of these droplets coincided with that of the gun electrode material, i.e. stainless steel [1].

Four types of samples were prepared by spark plasma sintering from powders with the average particle size ranging from 70 nanometers up to 80 µm. The sample nW was made entirely from a single type of nanometric powder with APS = 70 nm. The sample uW66 consisted of a mixture of nanometer and micrometer powders with weight concentrations 34% and 66% and an APS = 70 nm and 1.5 µm, respectively. The sample Wtaf was made entirely from a micrometer powder with APS = 80 µm while the sample Wtaf66 was a mixture of two micrometer powders with weight concentrations 34% and 66% and an APS = 80 µm and 1.5 µm, respectively.

The main parameters such as the electron temperature and density of the plasma jet were measured with a triple Langmuir probe. The plasma power load to the sample surface was estimated to be ≈4.7 MJ m^{-2} s$^{-1/2}$ per shot. The electron temperature and density in the plasma jet had peak values 17 eV and 1.6 × 10^{22}m^{-3}, respectively.

An EDS analysis of the nW sample and the gun electrode material is shown in Fig. 4. The peaks shown in Fig. 4 a) at 1.77, 8.39, 9.67, 9.96 and 11.29 keV are the $M\alpha_1$, $L\beta_1$, $L\beta_2$ and $L\gamma_1$ lines, respectively, of W as expected. In the second plot of the same figure 3 a) the X-ray spectrum of SS alloy 304 is shown with the main peaks corresponding to Fe, Cr, and Ni. Fig. 4 b) shows an EDS scan of the nanodroplets region of the exposed surface. Here the lines from both SS and W demonstrate that the origin of the nanodroplets is from the sputtered metal of the coaxial gun electrodes.

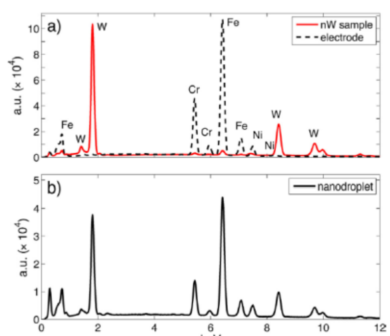

Fig. 4 a) EDS spectra of the bare electrode and pristine sample nW, before expo-sure; b) X-ray spectrum of a region containing nanodroplets found on the surface after 10 plasma shots.

IAP/IFIN-HH CONTRIBUTION TO PPPT NUCLEAR DATA DEVELOPMENT: EVALUATION OF NEUTRON CROSS SECTIONS, RADIATION DAMAGE DATA AND BENCHMARKING

M. Avrigeanu[1], V. Avrigeanu[1]

[1]*Horia Hulubei National Institute for Physics and Nuclear Engineering (IFIN-HH)*

WP-MAT

The Romanian partner (IFIN-HH) of the Consortium on Nuclear Data Development and Analysis has had the full responsibility for three Activities of the Task **MAT-5.7.1-T001** within Work Package 'Materials' (**WPMAT**) of the Power Plant Physics and Technology' (**PPPT**) Department of the *EUROfusion Consortium* (*European Consortium for the Development of Fusion Energ*y, concerning the presentation of the results obtained in IFIN-HH on (1) evaluation of fast-neutron induced alpha emission data on the basis of consistent nuclear model calculation of reaction cross sections, namely by using model parameters established through analysis of distinct independent data and performed for all available data for various reaction channels and isotopes of structural materials including EUROFER and SS-316, (2) evaluation of deuteron-induced reaction cross sections of Cr52 up to 50 MeV on the basis of the proper account of contributions of all involved reaction mechanisms as the breakup, stripping, pick-up, pre-equilibrium and evaporation processes, including the assessment of the related procedures recently involved in TALYS (http://www.talys.eu/) nuclear model calculations, and (3) update of the d-induced TENDL data library with cross-section data elaborated previously on the basis of improved models for the interaction of deuterons with low and medium mass nuclei (conducted in collaboration with EPFL/PSI producing and maintain the TENDL data libraries.

Firstly, the IAP/IFIN-HH contribution to PPPT nuclear data development has included the advanced evaluation of the optical model potential for alpha particles relevant for the evaluation of gas production and radiation damage data. Evaluation of fast-neutron induced alpha emission data on the basis of consistent nuclear model calculation of reaction cross sections, namely by using model parameters established through analysis of distinct independent data and performed for all available data for various reaction channels and isotopes of structural materials including EUROFER and SS-316 has been concerned in this respect. Finally, a suitable agreement has been obtained between all available measured cross sections of fast-neutron induced reactions on the stable Zr isotopes (e.g. Fig. 1), for incident energies up to ~22 MeV, and model calculations with no empirical rescaling factors of the γ and/or nucleon widths.

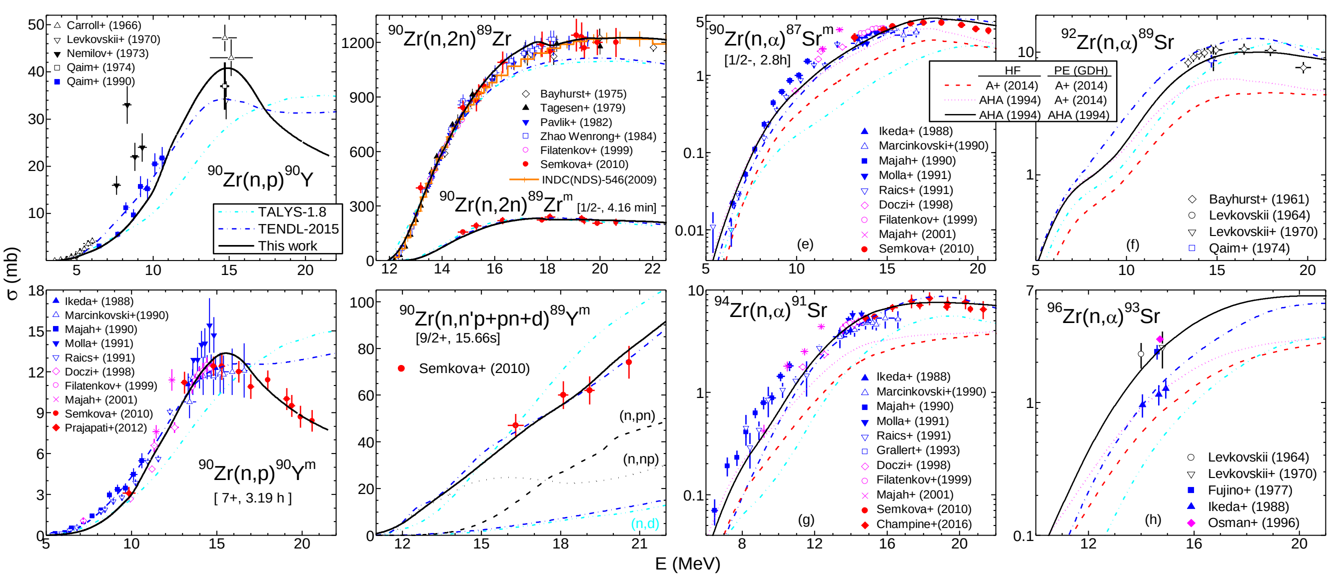

Figure 1. Comparison of measured, evaluated and calculated cross sections of (a-d) neutron-induced reactions on ^{90}Zr, and (e-h) the (n,α) reactions on ^{90,92,94,96}Zr [1].

Secondly, the IAP/IFIN-HH contribution to the PPPT nuclear data development has included the evaluation of deuteron-induced reaction data of structural materials and update of the d-induced TENDL data library as required for activation analyses of the IFMIF-DONES facility (PPPT project ENS). The evaluation of deuteron-induced reaction cross sections of ^{52}Cr up to 50 MeV on the basis of the proper account of contributions of all involved reaction mechanisms as the breakup, stripping, pick-up, pre-equilibrium and evaporation processes, including the assessment of the related procedures recently involved in TALYS nuclear model calculations, has also been concerned in this respect. The overall agreement of the measured data and model calculations validates the description of nuclear mechanisms taken into account for deuteron-induced reactions on ^{52}Cr, particularly the BU and DR that should be considered explicitly. Additional analyses of deuteron interactions with ^{50,53,54}Cr isotopes are requested for the complete description of experimental ^{nat}Cr(d,x) excitation functions.

Thirdly, the IAP/IFIN-HH contribution to PPPT nuclear data development has included the evaluation of deuteron-induced reaction data of structural materials and update of the d-induced TENDL data library as required for activation analyses of the IFMIF-DONES facility (PPPT project ENS). The update of the d-induced TENDL data library with cross-section data elaborated previously (2009-2016) on the basis of improved models for the interaction of deuterons with low and medium mass nuclei has also been concerned in this respect, to be completed by EPFL/PSI producing and maintaining the TENDL data libraries. Finally, 123 files of tabular residual cross sections in the TENDL-2015 format, corresponding to the results published previously for deuterons with the incident energies up to 50-60 MeV and target nuclei ^{27}Al, ^{54,56,57,58}Fe, ^{58,60,61,62,64}Ni, ^{63,65}Cu and ^{93}Nb (e.g. Fig. 2) are provided.

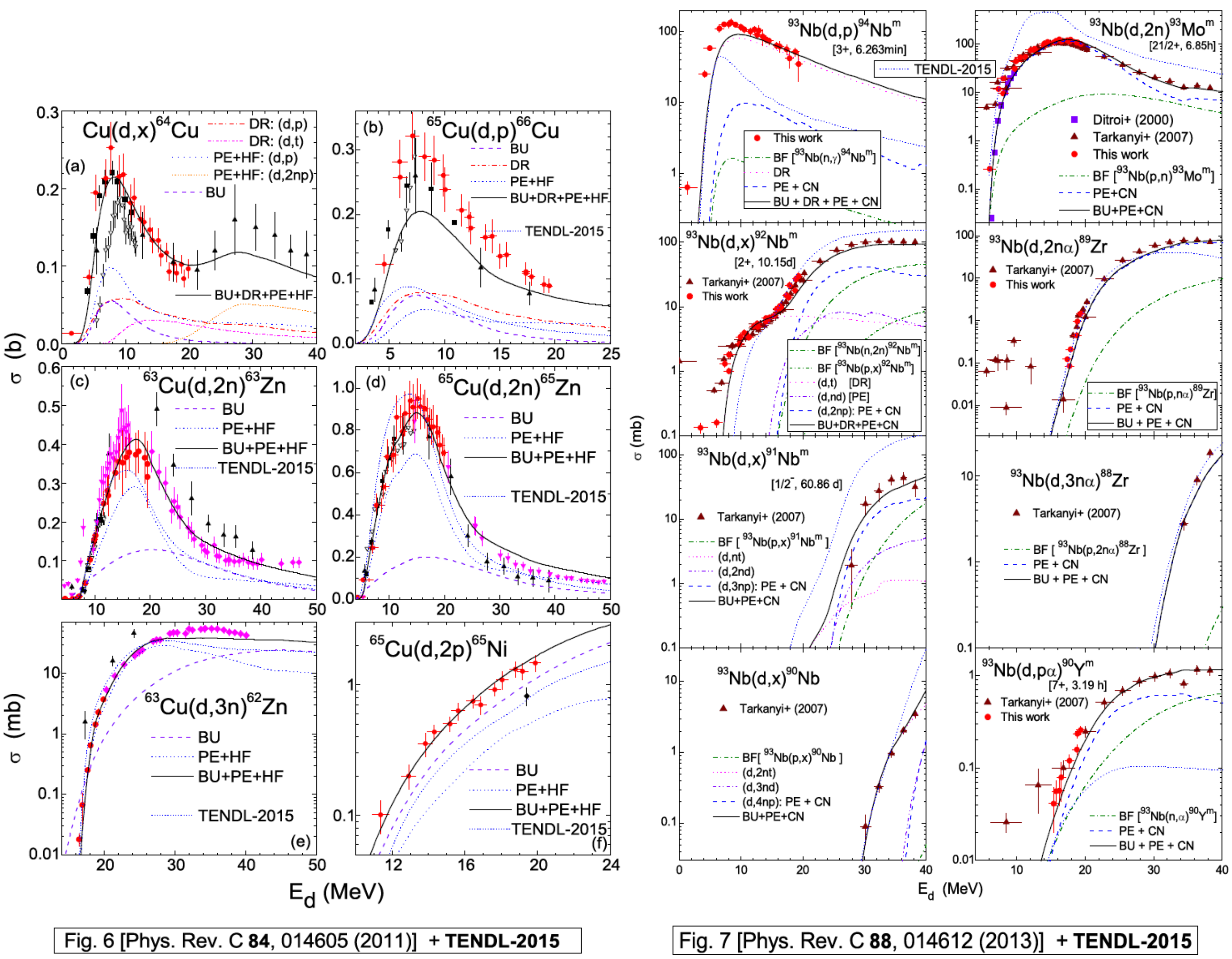

Figure 2. Comparison of measured, evaluated (TENDL-2015) and calculated cross sections of deuteron-induced reactions on ^{63,65}Cu (left) and ^{93}Nb (right) target nuclei [Final Report on Deliverable MAT-5.7.1-T001-D003].

Production of reference Be based coatings for PFC.SP2, PFC.SP3 si PFC.SP5

C. Lungu, C. Porosnicu, O.G. Pompilian, P. Dinca, B. Butoi, C. Staicu

IAP- National Institute for Lasers, Plasma and Radiation Physics, INFLPR
WPPFC-P

The activities performed within the framework of this project are in the support of the *IAP* (Romanian Eurofusion Research Unit) activities carried out in the *WPPFC* project. The WPPFC tasks presented here, are based on the production of reference Be based coatings for PFC.SP2, PFC.SP3 si PFC.SP5.

Be-C layers with O and D gas inclusions were obtained by a combination of High Power Impulse Magnetron Sputtering (HiPIMS) and Direct Current Magnetron Sputtering (DCMS) techniques co-deposited in a reactive gas mixture with Ar-D-O. Structural and compositional studies on these layers were performed after the deposition. The structural characterization of the films was performed using X-ray diffraction (XRD). Elemental depth profiles respectively elemental area densities were determined by means of Rutherford Backscattering Spectrometry (RBS). Experimental deuterium desorption spectra were obtained with a Thermal Desorption Spectroscopy (TDS) system.

I. Production and characterization of Be D containing coatings

Non-doped and Deuterium-doped (5 at%) Beryllium sample were obtained using Direct Current Magnetron Sputtering (DCMS) technique. The choice of using DCMS regime instead of HiPIMS was taken due to the large grains (µm sized) expelled from the target surface and plasma instability in the later regime during in – situ oxygen seeding. Deposition of beryllium and low oxygen doped beryllium samples with and without deuterium seeding was performed using a water-cooled magnetron head equipped with a high purity beryllium target in a circular chamber with a diameter of 60 cm operated in ultrahigh vacuum conditions 10-6 mbar with a turbo-molecular pump. Before each deposition a degassing procedure was performed consisting of a glow discharge cleaning of the walls in argon atmosphere. The experimental set-up used for the depositions is represented in Fig.1.

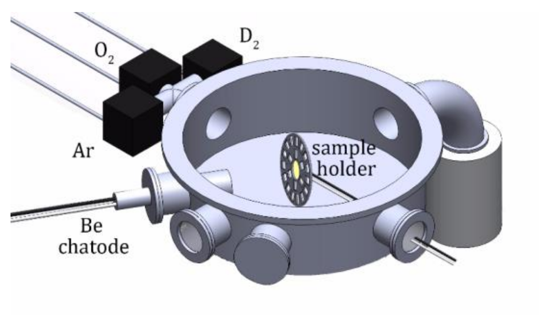

Fig. 1 *The schematic view of the deposition system used for obtaining Be-C layers with D and O gas inclusions*

Silicon (12X15mm) and mirror finished graphite, molybdenum and tungsten (12X15 mm) were used as substrates for these coatings. The substrates were distributed on a fixed sample holder placed inside the reaction chamber and positioned in front of the sputtering source at a distance of 10 cm. In order to obtain the best uniformity possible a circular sample holder with the diameter comparable with the sputtering target was used. The deposition rates were monitored in-situ, not based on calibrations like in previous experiments, using a QMB placed in the centre of the circular holder. This allowed for a free adjustment of the plasma parameters during deposition and also a precise final thickness of 400 nm.

II. Characterisation of the obtained layers

SEM measurements were carried out on Be co-depositions with well-defined thickness values of 500 nm obtained by D flux variation to analyse sample morphology. From SEM images obtained for co-deposited samples with D flux of 2 and 4 ml/min respectively, a diminished morphology of surface can be seen corresponding to Be dense films growth. At 10 ml/min it can be seen a change in morphology, thus observing a granular surface. At a Ar:D (1:1) ratio, on the film surface there can be seen micrometre particles most likely ejected from Be target. From the obtained images for Be co-depositions on W substrate it can be seen an irregular morphology on the surface for all analysed samples. The observed gaps on the surface as well as irregular morphology of sample surface are due to W rough layers. It can also be seen that, at high D flows the number of micrometric particles sputtered from Be target is greater in comparison with low D flows.

Rutherford back-scattering spectrometry was applied to determine atomic composition for Be co-depositions. The samples were mounted on a goniometric holder, adjustable on 3 axes with a 0.01o precision. To limit beam divergence there were used slots. The detector, with an energetic resolution of 22 keV used to detect proton back-scattering, was 165^0 angled depending on the beam. A wide 0.4 mm2 monoenergetic ion beam with 2.549 MeV energy was focused on the sample. The accumulated load was measured with a Faraday cage and the final value was set at 10 μC. The atom density on surface, depth profile as well as layer thickness were obtained by experimental spectra simulation using SIMNRA programme. From the spectra it can be seen the signal corresponding to D in the are of channel 100. It is observed that this signal becomes more intense once with D flux increase. This fact confirms that D accumulates inside the sample once with D flux increase, used to obtain the co-depositions. It must be mentioned that it was not observed a saturation of the signal in the measured samples.

One of the important results of the study is that for the first time in the existent literature regarding deuterium retention in fusion related materials, the deuterium inventory inside the sample was high enough to be quantitatively observed in RBS spectra. The quantitative results offered by these measurements for deuterium are orientatively given because there is not yet a quantitative calibration to show precise data regarding deuterium content in the sample. RBS spectra excellently show the intense signal generated by beryllium presence in the samples. This signal is between 500 and 600 respectively. Visually, it can be seen a decrease in Be signal intensity once with deuterium flux increase. Thus, a higher D flux in the deposition chamber during the co-deposition leads to a lower sputtering efficiency of beryllium target. It can be seen a sample oxygen contamination mostly due to its exposure to atmospheric air after deposition process. Taking into consideration the low oxygen concentration we can assume that the level of gaseous impurities during co-deposition was minimum. Also, it can be seen an increase with a factor of 2 of deuterium signal specific to samples prepared with high D flux in comparison with those obtained at low flux.

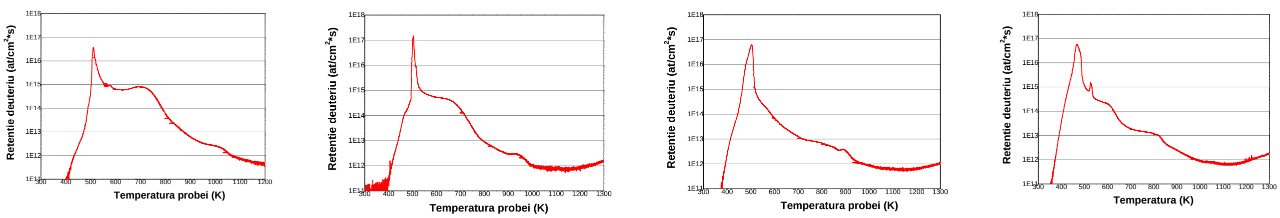

D_2 2ml/min flow *D_2 4ml/min flow* *D_2 10ml/min flow* *D_2 20ml/min flow*

Fig. 2. RBS experimental spectra vs SIMNRA simulated spectra

Thermal desorption spectroscopy (TDS) measurements: D desorption spectrum from beryllium co-deposition obtained with a D flux of 2ml/min shows the presence of an intense desorption peak with its maximum at 510.9K. This peak can be associated to desorption from states created by deuterium oversaturation inside the sample and most likely to sample porosity. Also, the presence of a maximum of low intensity can be seen at 579K. D desorption from pure beryllium at this temperature is usually in literature attributed to deutera molecule dissociation from beryllium. The presence of a wide desorption shoulder is observed in the range 630 K-730K most likely due to deuterium trapping release from beryllium oxide traps.

For beryllium co-deposition obtained at a flux of 4 ml/min, it is observed in the desorption spectrum the presence of an intense maximum that occurs at 502K as well as a desorption shoulder that starts at 639K. Also, it can be seen a deuterium release at high temperatures with a maximum at 942K specific either to high energy trapping release or due to D systematic trapping and release mechanisms.

The desorption spectrum of the sample obtained at D flow of 10ml/ min shows the presence of the same desorption maximum characteristic to other desorption spectra with the centre at 502K and 895K respectively.

For the sample obtained at a 20ml/min flow it can be seen a textured desorption spectrum from deuterium traps point of view. Thus, it can be seen the presence of a very intense desorption maximum at 465K, and a desorption peak at 523K. Also, it can be seen the presence of a desorption shoulder specific to beryllium oxide trapping release that starts at 630K and a desorption shoulder specific to high energy beryllium trapping between 770K-840K.

Production of W- based reference samples with gas inclusions

E. Grigore, C. Ruset, M. Gherendi

IAP- National Institute for Lasers, Plasma and Radiation Physics, INFLPR
WP-PFC-P

The working plan for 2017 for the *WPPFC* project and assigned to *IAP* required activities concerning the production and the characterization of W based reference coatings with different gas inclusions too. The main results are summarized in the following report.

The production of the coatings was performed by using 2 deposition methods: Combined Magnetron Sputtering and Ion Implantation (*CMSII*) and High Power Impulse Magnetron Sputtering (*HiPIMS*). The same deposition method, *CMSII* has been used for deposition of W coatings of *JET* tiles and its principle has been discussed in the previous reports of the project. Its advantages in producing coatings with thickness in the range of 10-20 µm, with remarkable properties in terms of adhesion and resistance to high heat fluxes are well known. The *HiPIMS* deposition method was selected as preliminary experiments showed that the D content within the W coatings produced so far by *CMSII* method was confined to 1.3 at. %. As far it concern the *HiPIMS* deposition method it is characterized by a high pulse power density at the sputtering target, which is typically two orders of magnitude greater than the average power density.

The chemical composition (elemental depth profile) of the coatings was performed by using Glow Discharge Optical Emission Spectrometry (*GDOES*). Thermal Desorption Spectrometry (*TDS*) measurements were also performed in order to evaluate the gas content (D, Ar, N) released from the coatings. Time of Flight Elastic Recoil Detection Analysis (*TOF-ERDA*) was performed on a series of samples at *RBI* Croatia by Dr. Iva Bogdanovic. *TOF-ERDA* measurements were done using 20 MeV 127 I^{6+} beam. Angle between sample surface and beam was 20°. Spectrometer was placed at 37.5°. The analysis of *TOF-ERDA* spectra was done using program Potku.

The produced samples were used for further experiments by other Eurofusion Research Units within the framework of *WPPFC* project.

W+ D coatings

The W coating with D inclusion has been produced by *HiPIMS*. The duty cycle in the case of *HiPIMS* deposition is very low and consequently the deposition rate, compared with *CMSII*. Compared with deposition rate in the case of *CMSII*, where a deposition rate of 2.5 µm/h (41.6 nm/min) is common, the deposition rate in the case of *HiPIMS* is 0.048 µm/h (0.8 nm/min) and that is why in order to get thicknesses of the coatings according to the required specifications the deposition time is considerable higher. After deposition, the coatings were subjected to *TDS* analysis. The *TDS* measurements supply the first information about the gas content within the coatings. Although the *TDS* cannot supply information concerning the gas distribution within the coatings, it remains a valuable instrument for a first assessment of the gas content within the coating. From the *TDS* a spectrum for W+D coatings obtained by HiPIMS it was observed that the D starts to be released at ~ 200^0 C and has a maximum at ~ 410^0 C. Also two release peaks belonging to Ar have been observed at ~ 450^0 C and ~ 900^0 C.

For the same coating, the *TOF-ERDA* measurement indicated the following composition of the coating: H 2.0 ± 0.4 at.%, D 12 ± 2 at.%, C 1.6 ± 0.4 at.%, N 4.4 ± 0.7 at. %, O 9 ± 1 at.%, Ar 9 ± 1 at.% and W 62 ± 4 at.%.

W-Al+D coatings

W-Al coatings were obtained by *CMSII* deposition method. The specifications for this type of coatings were: thickness 2 µm, Al content 10 at.% and D 5 at.%. From *GDOES* depth profile analysis performed on W-Al+D coatings it was noticed an Al concentration of ~ 10 at.% uniformly distributed within the coatings. The D profile within the coating reveals also a relatively uniform distributed concentration. The coating thickness was ~ 3.2 µm.

In this case, the *TOF-ERDA* measurement report the following composition: H 1.4 ± 0.2 at.%, D 2.5 ± 0.5 at.%, C 1.1 ± 0.2 at.%, N 1.0 ± 0.2 at. %, O 1.2 ± 0.2 at.%, Al 6.4 ± 0.5 at.%, Ar 11.3 ± 0.8 at.% and W 75 ± 4 at.%.

TDS analysis was performed at 700^0 C and 950^0 C. During the *TDS* experiments it was noticed that the D start to be released from the coating at ~ 600^0 C and reaches a maximum at ~ 650^0 C. In this case the Ar released from the coating is insignificant compared with D.

W-N+D coatings

W-N coatings with different N content have been produced by using *HiPIMS* deposition method. The specification asked N content of 5 at.% and 10 at.% with and without D inclusions. In the case of W-N+D coatings the *GDOES* depth profile indicated a thickness of ~3 µm. For the W-N+D coating with high N content, the composition as determined by GDOES was D~ 40 at. % and N ~17 at. %. It should be emphasized that although the D was introduced at the same flow rate with that corresponding to W+D coating, the D content within the W-N coating is almost twice. That indicates that N support the D retention into the W coating.

The *TDS* experiments were conducted in a different manner taking into account that besides the D, the N released from the coating is of interest too. It is know that the wall of the analysis chamber trap N when exposed to air. That is why this N is released from the wall during the heating of the samples is superposed with the N released from the sample. Consequently the sample chamber was outgassed for 30 min. at the same temperature used in the *TDS* experiments and then the samples of interest were analyzed without breaking the vacuum. The *TDS* analysis indicated that for both samples with low and high N content, the D starts to be released at 200^0 C and continues up to ~ 650^0 C. The N trapped within the coatings showed 2 regions: the first region corresponds to N released at ~400^0 C and the second region corresponds to N released at ~800^0 C. This feature indicates different energies for N bonding in W coatings. The low temperature N release peak is higher for the coating with a low nitrogen content compared with the coating with a higher N content where the high temperature release peak is more pronounced.

TOF-ERDA analysis performed on W-N samples with D indicated the following results:

- for a lower N content coating: H 1.4 ± 0.3 at.%, D 19 ± 2 at.%, C 1.8 ± 0.3 at.%, N 23 ± 1 at. %, O 8.0 ± 0.9 at.%, Ar 2.3 ± 0.8 at.% and W 44 ± 2 at.%.

- for a higher N content coating: H 4.0 ± 0.6 at.%, D 20 ± 2 at.%, C 2.9 ± 0.5 at.%, N 33 ± 2 at. %, O 5.6± 0.7 at.%, Ar 1.6 ± 0.3 at.%, W 32 ± 2 at.%.

W-N coatings

Another series of W-N samples have been obtained without D inclusions. The specifications for the W-N coatings required the synthesis of W coating with a low N content (5 at.%) and with a higher N content (10 at.%). Compared with the same coatings with D content, these types of coatings were produced by *CMSII*. It has been observed that for low N coating, the *GDOES* analysis indicated a N content of 3.8-7.7 at.% whereas for higher N content the *GDOES* indicated a N content of 8.7-10 at.%.

Reference W coatings

A series of W coatings of 5 µm thickness deposited on Mo substrates were produced by *CMSII* and were then loaded with different gas inclusion at Differ and FZ Juelich.

CO-DEPOSITION OF W-AL THIN FILMS BY DUAL-HIPIMS

C. Costin, V. Tiron, V. Anita, G. Popa

Alexandru Ioan Cuza University, Faculty of Physics, Bd. Carol I nr. 11, 700506-Iasi, Romania

WP-PFC-P

Co-deposition of W-Al thin films by dual-HiPIMS in Ar-D_2 gas mixture

W-based thin films with different Al concentrations have been deposited by dual High Power Impulse Magnetron Sputtering (dual-HiPIMS) in Ar+D_2 gas mixture, to study the role of the film chemical composition on the fuel (D) retention. High-voltage pulses (-900 V / 5 μs) have been applied on each target (W and Al). The D_2 to D_2+Ar mass flow ratio was set to 50%, while the total gas pressure was kept constant at 1 Pa. The Si substrate was placed at 10 cm from each target surface; during deposition it was electrically grounded and unintentionally heated. Three samples have been prepared by adjusting the input power on each target: S1 (W: 80 at.% - Al: 20 at.%), S2 (W: 90 at.% - Al: 10 at.%) and S3: WAl with Al content gradient. The composition of the WAl coatings has been determined by depth profiling using Glow Discharge Optical Emission Spectrometry (GDOES). The GDOES profiles indicate the presence of deuterium in the WAl thin films, with the largest amount in the sample S1, the maximum concentration being 21 at.%, with an average value (estimated over the entire thickness) of 15 at.%. D retention in the WAl layer is manly related to the W in-depth concentration and less dependent on the Al one. Depth profiles for the sample S3 show that, by increasing the Al concentration in the WAl film, the amount of D tends to decrease. The depth profile of D has almost the same evolution as W in-depth profile. This behavior may be related to the fact that the D embedded in the layer comes mainly from the discharge developed in front of the W target, most probably as D^- ions (see the discussions of the second objective).

XRD studies were carried out in order to identify the crystallinity and various phases present in the W based thin films. Sample S1 is polycrystalline and preferentially oriented along (2 1 0) plane, while sample S2 is crystalline, being oriented along (2 1 0) plane. Sample S3 seems to be amorphous.

SEM images of the samples reveal very dense coatings with homogeneous microstructure, without indications of columnar growth, which is a sign of a high film packing. The main mechanism responsible for the film densification is the intense and energetic bombardment of the growing film with heavy particles. Previous studies have shown that during HiPIMS operation with short pulses, the fraction of the ionized W in the total flux is up to 50% and the energetic tail of W ions IEDF extends towards 100 eV [1].

Recently (see reference [2] and the discussions of the second objective), mass spectrometry measurements have shown that during HiPIMS sputtering of W in A-D_2 gas mixture, the total ion flux to the substrate is dominated by the negative ions D^- with a very high energetic tail in the IEDF, extending up to 500 eV. Therefore, the large amount of deuterium embedded in the WAl thin films may be related to the energetic bombardment with D^- negative ions.

Investigations on D^- ions

The measurements on the ion energy distribution function (IEDF) during co-sputtering of W and Al targets in dual-HiPIMS mode, in Ar-D_2 gas mixture, by using an energy resolving mass spectrometer (EQP 1000 Hiden Analytical), have shown the presence of a large fraction of D^- ions in the total ion flux to the substrate. The production of D^- negative ions occurs through the dissociative attachment from highly vibrationally excited molecules $D_2(v)$ [3]:

$$D_2(v) + e^-_{slow} \rightarrow D^- + D,$$

where $D_2(v)$ are produced through the following reactions:

$$D_2(v{=}0) + e^-_{fast} \rightarrow D_2^* + e^-_{fast}$$

$$D_2^* \rightarrow D_2(v) + h\nu.$$

This statement is sustained by the optical emission spectroscopy measurements which indicate the presence of D_α and D_β neutral spectral lines and Fulcher α-band (attributed to highly vibrationally excited D_2 molecules) in optical emission spectra of HiPIMS Ar-D_2 plasma.

Consequently, the production of D^- occurs through electron impact dissociation from highly vibrationally excited molecules $D_2(v)$ which, in their turn, are generated by fast electron collisions. It is expected that an increase of the input power and/or the $D_2/(D_2+Ar)$ mass flow ratio to lead to a higher electron density and temperature which, in turn, facilitates the occurrence of electron impact dissociative attachment reactions and generation of D^- negative ions.

Figure 1 shows the time-averaged IEDFs of D^- ions for dual-HiPIMS operation with W and Al targets, in three different Ar-D_2 gas mixtures (both targets operate at 100 W). The energy distribution functions of D^- ions show a maximum around 1 eV and a very high energy tail which extends towards 500 eV. The high-energy tail contains D^- ions produced in the ionization region of the HiPIMS plasma and repelled by the highly negative potential of the target. An increase of the input power and/or the $D_2/(D_2+Ar)$ mass flow ratio leads to an increase of both low and high energy part of the IEDF of D^-.

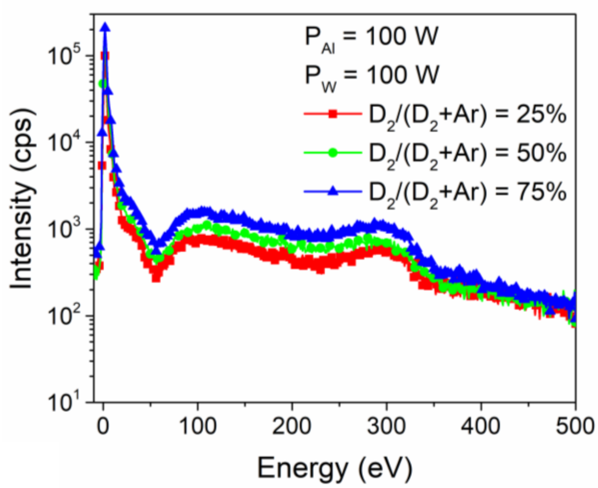

Figure 1 – IEDFs of D^- ions in dual-HiPIMS mode, for different Ar-D_2 gas mixtures (both targets operate at 100 W).

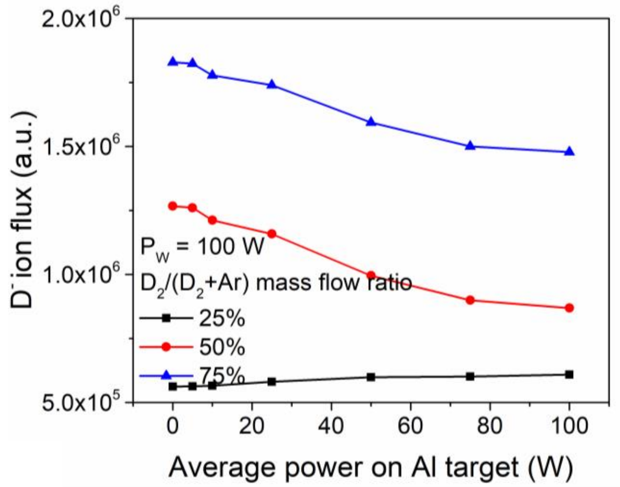

Figure 2 – D^- ion flux measured in dual-HiPIMS mode, at different input powers on the Al target and for different Ar-D_2 gas mixtures.

Figure 2 shows the D^- ion flux versus the average power on the Al target, measured during dual-HiPIMS operation with W and Al targets. The D^- ion flux was calculated as the integral of the IEDF. At low $D_2/(D_2+Ar)$ mass flow ratio (25%), the D^- ion flux increases with the input power on the Al target and tends to saturate above 50 W. At high $D_2/(D_2+Ar)$ mass flow ratio (50 and 75%), the D^- ion flux tends to slowly decrease as the average power on Al target increases. During standard HiPIMS operation (power on Al is turned off), the D^- ion flux linearly increases with the input power on the W target and with the increase of $D_2/(D_2+Ar)$ mass flow ratio. This behaviour may be related to the enhanced electron density and temperature which facilitates the occurrence of electron impact dissociative attachment reactions, leading to an increased population of D^- negative ions in the HiPIMS discharge.

References

[1] I.-L. Velicu, V. Tiron, C. Porosnicu, I. Burducea, N. Lupu, G. Stoian, G. Popa, D. Munteanu, Applied Surface Science 424 (2017) 397–406.

[2] Research report of the Complementary part of this project (2017).

[3] C. Gorse and M. Capitelli, Physical Review A 46 (1992) 2176.

Investigation of bulk W samples envisaging topography and morphology characteristics

B. Mitu, C. Stancu, V. Marascu, F. Stokker – Cheregi, G. Dinescu

National Institute for Lasers, Plasma and Radiation Physics, Romania

WPPFC-P

Several types of bulk tungsten samples (purity at least 99%), produced by various companies, have been studied in the current phase of the programme, as model for the bulk W involved in the construction of WEST divertor in Cadarache. The aim was to investigate typical properties of metallic W surfaces in their as-received state, respectively upon surface modification by means of mechanical polishing procedures, before any plasma exposure. The research was focused on a comparative analysis of the results regarding the surface morphology and topography, obtained by different investigation techniques, which address to nano, micro and macro scale of investigation. Large dimension components used in fusion devices with metallic plasma facing units can be characterized using the same approach.

I. Experimental approach

Thin foils (0,1 mm), rods (10 mm diameter), rectangular (30x30x4 mm) and circular (30 mm diameter) pieces targets were investigated. Contact profiler P-7 KLA-Tencor equipped with a diamond stylus of 2 microns radius, with a horizontal scan stage up to 150mm and vertical range up to 327 microns, and respectively AFM Park System Microscope, Model XE100, maximum horizontal scan range of 50×50 μm^2, and maximum vertical movement 8 μm were involved for topographic investigation at micro and nanoscale. Scanning Electron Microscopy (SEM) combined with EDAX module were used for morphological and compositional investigations.

II. Results and discussions

The optical microscopy investigations reveal that the surface presents texturing along the y direction, which are originating from the fabrication procedure, confirmed by the surface topography over large areas, provided by profilometry investigations. Additionally, the presence of holes noticed by SEM investigations show in 3D profilometry images typical dimensions in the range of hundreds of microns and depths of few microns, resulting into an overall roughness of hundreds of nm. (Figure 1).

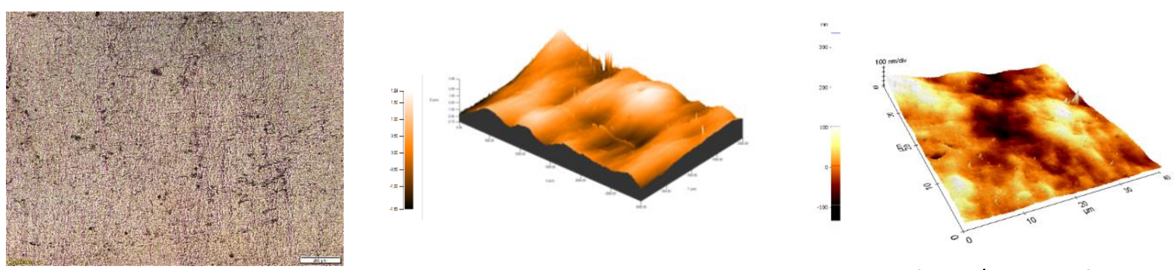

5x magnification
9000 x 6000 μm^2 area

RMS roughness = 289 nm
3000 x 2000 μm^2 area

RMS roughness = 43 nm
40 x 40 μm^{2}area

Figure 1 – Typical aspect of as-received W bulk samples - by optical microscopy, profilometry and AFM

The mirror polished samples (30 mm diameters disks) have also been investigated in a statistical manner. Although the general aspect of the samples is quite similar, revealing rounded shape features on the surface, and a few holes, the overall roughness varies on areas of 3000 x 1500 μm^2 up to 3 times from one sample to another (from 43 to 113 nm), similar to the behaviour encountered on tungsten materials exposed to a hollow cathode plasma [1]. The SEM images recorded on these samples show a generally smooth surface on which various defects are present, most of them in the form of superficial micro holes of large dimensions and deep small dimension nanoholes.

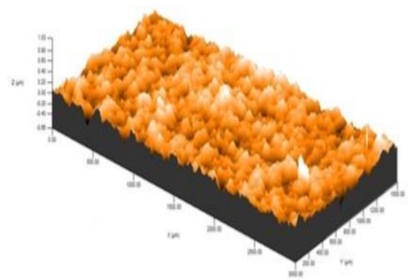

RMS roughness = 75 nm

3000 x 1500 μm^2

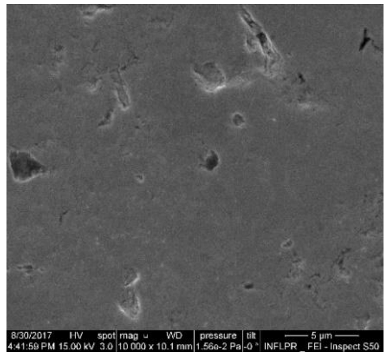

10000 x magnification

30 x 20 μm^2

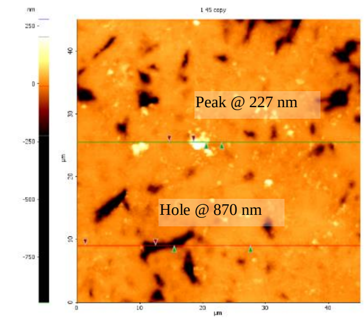

RMS roughness = 49 nm

45 x 45 μm^2

Figure 2 – Morphological and topographic investigation of polished W samples

The EDX measurements revealed a chemical composition of the samples of 76.74 at% tungsten, 21.39 at% oxygen, and a small amount of carbon, of 1.87 at%, originating from the superficial contamination of the sample. The large amount of oxygen determined from the EDX spectra indicates that a significant oxidation process takes place on the sample surface, in the as-received form, which may conduct upon hydrogen plasma exposure to the reverse reduction process, but also to the formation of defects, preferentially in the regions where features like drops and holes are present.

III. Conclusions

A combination of small and large scale investigations of the tungsten surfaces, combined with statistical analysis of the observed features is the ideal approach for the morphological and topographic characterization of the samples. At the same time, special attention should be paid on the modifications induced by high density plasmas onto various types of defects present on the tungsten surface, since the specificity of each defect may conduct to different behaviour of the surface once exposed to the plasma.

In the next stage tungsten surfaces exposed to plasmas with various characteristics will be investigated in order to reveal the surface modifications, especially in the pre-damaged tungsten surface. Due to schedule modifications of the experimental campaigns in WEST, the analysis of the materials exposed to plasmas will be completed at the end of C3-C4 campaign, upon dismantling the mock-ups.

References

[1] C. Stancu, F. Stokker-Cheregi, A. Moldovan, M. Dinescu, C. Grisolia, G. Dinescu, *Modification of W surfaces by exposure to hollow cathode plasmas*, Appl. Phys. A (2017) 123:618, DOI 10.1007/s00339-017-1235-4

Developments of characterisation methods development and reference samples characterization

C. Lungu, E. Grigore, C. Ruset, C. Porosnicu, M. Gherendi, O.G. Pompilian, P. Dinca, B. Butoi, C. Staicu

IAP- National Institute for Lasers, Plasma and Radiation Physics, INFLPR
WP-PFC-C

I) Characterization of reference samples and produced markers, Be and Be-W coatings with high D and N content using SEM and XRD

Pure Be 500 nm films were deposited on Si and W substrates in Ar-D reactive atmosphere using DC magnetron sputtering. The thickness of the films was strictly monitored during the entire deposition procedure using a quartz microbalance placed in the proximity of the substrates. This study aims to analyse the retention in the co-deposited BeD layers. Four co-depositions were performed at different D fluxes: 2; 4; 10; 20 s.c.c.m, to analyse the influence of the nuclear fuel on retention in co-depositions. The motivation for Be co-depositions is grounded on multiple studies that showed that nuclear fuel retention in Be co-depositions will represent the greatest part of the inventory retained in ITER. Structural analyses of the obtained samples were carried on by XRD measurements.

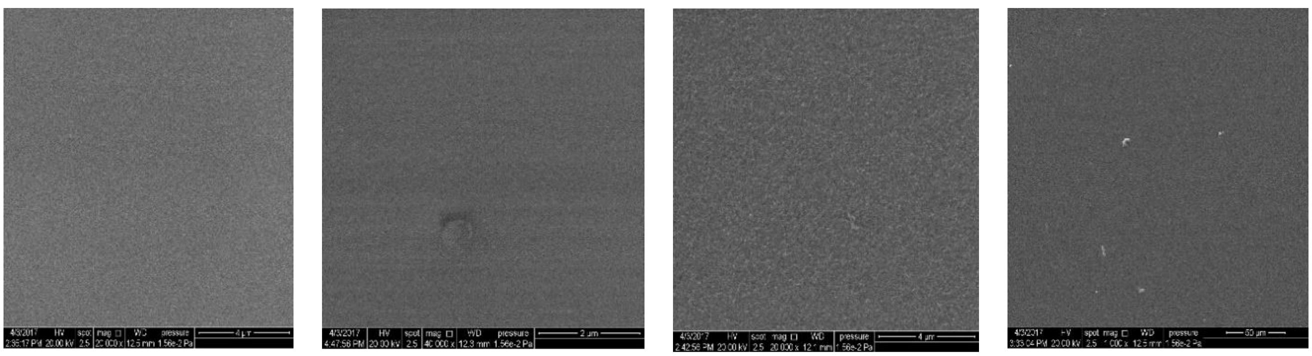

a) 2ml/min b) 4ml/min c) 10ml/min d) 20ml/min

Fig. 1 SEM images for Be co-depositions on Si substrate

SEM measurements were carried out on Be co-depositions with well-defined thickness values of 500 nm obtained by D flux variation to analyse sample morphology. SEM images are represented in Fig I 1.

From SEM images (fig.1) obtained for co-deposited samples with D flux of 2 and 4 ml/min respectively, a diminished morphology of surface can be seen corresponding to Be dense films growth. At 10 ml/min it can be seen a change in morphology, thus observing a granular surface. At a Ar:D (1:1) ratio, on the film surface there can be seen micrometre particles most likely ejected from Be target.

Be co-depositions structural analysis obtained in Ar-D by XRD measurements. To obtain precise results, the samples deposited on SI substrate were analysed to avoid inside the diffraction spectrum the presence of lines characteristic to W. The analysis was carried out using a diffractometer with X-ray source (CuKα) with wavelength of 0.154 nm. The measurement range 2θ was between 20^o-60^o. The results for these measurements are shown in Figure I 3.

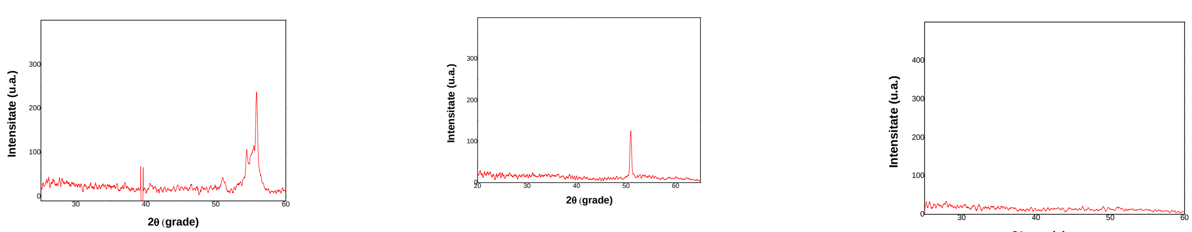

D_2 2ml/min flow *D_2 4ml/min flow* *D_2 20ml/min flow*

Fig. 2 Diffractograms for Be co-depositions on Si substrate

X ray diffractogram obtained for Be films in Ar-D atmosphere shows semi-crystallin nature of Be films obtained at 2 and 4 ml/ min respectively. Also, their intensity is very low due to small thickness of film (500 nm) and especially due to Be X ray transparency properties. At 2ml/min D_2 flow, the presence of the diffraction maximums can be seen, one centred 2θ of 51.14° and the other one at 53.14°. Both maximums correspond to Be metallic phase with hkl orientations for the first maximum (002) and (101) respectively. Comparing the diffraction maxims intensities, it could be seen a similarity with Be perfect crystal in literature with preferential growth on (101) orientation. But the sample obtained at 4 ml/min flow shows only one diffraction maximum corresponding to (002) orientation. Comparing the two samples it can be seen that D flow influences the crystalline growth. At a 20 ml/min flow the presence of a diffraction maximum cannot be seen. This amorphous behaviour can be determined either by gaseous inclusions present inside the crystalline structure of the deposited layers, either by a more intense ion gas bombardment.

II) Development of the methodology for W erosion investigation using GDOES technique.

In the present stage of this project the methodology for investigation of W erosion in *WEST* divertor using the *GDOES* technique was developed. The methodology for determination of W erosion in *WEST* divertor using *GDOES* technique involves the following steps:

Step 1. Production of the reference samples (not exposed to plasma) to be used for comparison with the real samples that will be cored from the tiles exposed in WEST.

This step consisted in coating with W of a number of 30 samples made of *FGG* together with 73 real tiles in 5 coating runs (IU-524, IU-525, IU-528, IU-534, IU-525). The samples were positioned in the coating run in 6 or 7 locations along the tiles. Ti and fine grain graphite (*FGG*) witness samples were employed. The *FGG* samples (Φ7x10 mm) are hold by special stainless steel holders. The W-coated Ti witness samples are used for quality control of the tiles coated in that run whereas the *FGG* coated samples will serve as reference samples in erosion measurements.

Step 2. Development of the GDOES method for analysis of W coatings deposited on FGG substrate

This step was finished in 2017. The results have been presented in previous report.

Step 3. Selection of the tiles to be used for determination of W erosion after plasma exposure.

The tiles must be selected from the list of 73 tiles for which there are witness samples not-exposed to plasma. Selection will be performed by *CEA* in collaboration with *INFLPR*. Both long tiles (Inboard Normal SIGRAFINE R6710P010D01) and short tiles (Outboard Normal SIGRAFINE R6710P010D01) should be selected. In this way the erosion on the entire lower divertor will be assessed.

Step 4. Coring of the samples from the tiles exposed to plasma.

Six samples (Φ7x10 mm) will be cored from each selected tile. Position of the cored samples will be close to the position of the witness samples in the coating run. The coring process will be performed at *INFLPR*.

Step 5. Determination of the W erosion

Cored samples will be analyzed by *GDOES* together with the witness samples. By comparing the *GDOES* depth profiles for the samples exposed and not exposed to *WEST* plasma the erosion of the W coating will be determined.

Microbeam X-ray fluorescence as a tool for erosion and re-deposition studies on PFC surfaces

I, Tiseanu, M. Lungu, C,. Dobrea, A. Sima

IAP- National Institute for Lasers, Plasma and Radiation Physics, NILPRP

WPPFC-C

Microbeam X-ray fluorescence technique was validated for erosion and re-deposition studies of ITER-like mixed materials.

In the XRF method, high accuracy identification for low concentration elements is not straightforward leading to the need of standard samples and additional simulations. Standard samples are co-deposited mixtures of ITER-like materials produced by the in-house *Thermoionic Vacuum Arc (TVA)*. Different coatings were produced in alloy and multilayer modes with TVA configured for maximum three targets (W, Fe and Cr) on Ti or C substrates (*figure 1*).

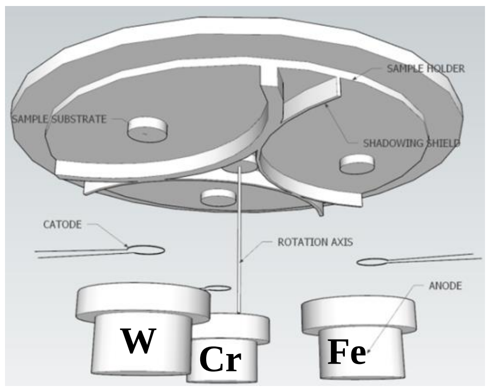

Figure 1 - TVA geometry setup. For alloy co-depositions were based on pure Fe, Cr and W anodes that were ignited in the same time. In order to obtain the multilayer samples, after each deposition process, the plasma ignition was interrupted and the substrate holder was rotated to have a direct view of a different substrate.

The co-deposited alloy obtained in the central area of the substrate holder was monitored to integrate an approximated concentration of W 2%, Cr 9% and Fe 89%. Five samples were deposited, three corresponding to the direct projection of each anode on a Ti substrate and two placed in the central area of the sample holder on C and Ti substrates.

The multilayer samples were obtained by rotating the substrate holder as gradient structures of W, Cr and Fe on Ti substrates. A total of six combinations of multilayer samples were produced.

Hence, *figure 2* shows the elemental analysis of the alloy samples. As shown in the inset, there is a good agreement of the compositions measured by XRF and the built-in quartz crystal microbalance (QCM) of the two samples.

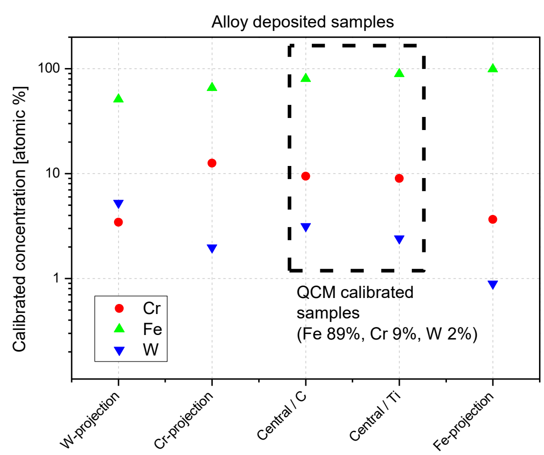

Figure 2 Elemental compositions of alloy samples co-deposited by TVA technique. In the inset one shows the good agreement of the results for samples with composition estimated by QCM.

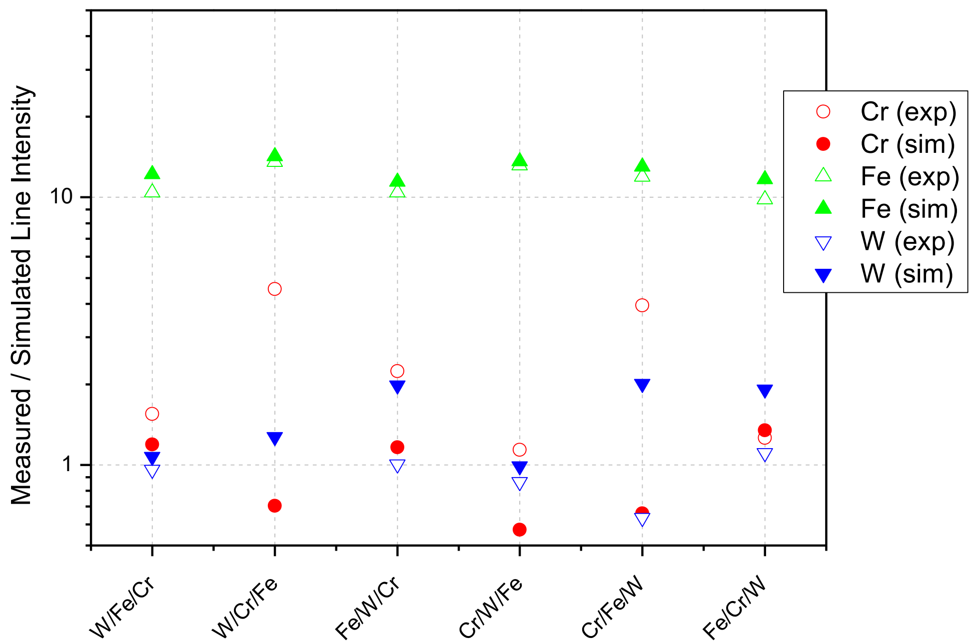

Figure 3 - Measured and Monte Carlo simulated X-ray line intensities for six different combinations of layer thicknesses

The composition and the thicknesses of the multilayer samples are more difficult to assess both by the XRF and QCM methods. In the reporting period we approach this problem by Monte Carlo simulations of the matrix effects of X-ray emission in the multilayer configuration. M-C simulations offer, always, the possibility to generate synthetic XRF calibration samples. The XRF geometry setup was realistically simulated in order to determine the fluorescence response for each element. As a limitation of the M-C simulation program, calculations can only be conducted on pure multilayer composition while the multilayer samples might include layers with gradient compositions.

However, as shown in *figure 3* there is a good qualitative agreement between the measured and simulated line intensities over six different combinations of layer thicknesses.

This result should be consolidated by application of a new fundamental parameters calculation module for absolute layer thickness measurement.

CHARACTERISATION OF W AND AL CO-SPUTTERED MATERIAL IN THE GAS PHASE BY MASS SPECTROMETRY IN DUAL-HIPIMS

C. Costin, V. Tiron, V. Anita, I. Mihaila

Alexandru Ioan Cuza University, Faculty of Physics, Bd. Carol I nr. 11, 700506-Iasi, Romania

WPPFC-C

Characterisation of W and Al co-sputtered material in the gas phase by Mass Spectrometry in Ar-He dual-HiPIMS

Mass spectrometry measurements were carried out in a dual High Power Impulse Magnetron Sputtering (dual-HiPIMS) device. The two cathodes were placed in an open magnetic field configuration, having W and Al targets (2 inch diameter). The average power on the W target was kept constant and set to 100 W, while the average power on the Al target was varied from 5 to 100 W, by independent manipulation of the pulsing repetition frequency. Other working parameters: applied voltage -1 kV, pulse duration 3 μs, gas pressure 1 Pa. The ion flux composition was investigated by measuring the ion energy distribution functions (IEDFs) of different plasma species using an energy resolving mass spectrometer (EQP 1000 Hiden Analytical). Both sputtering targets were positioned at 17 cm distance from the mass spectrometer, W target was positioned in front of the mass spectrometer, facing directly the nozzle, while Al target was positioned sideways to the W target, at an angle of 45° from the spectrometer head axis. Time-averaged IEDFs of Al^+, W^+, W^{++}, Ar^+, Ar^{++} and He^+ were recorded during Al and W co-sputtering in dual-HiPIMS. For each ion type, the flux was calculated as the integral of the IEDF. The total ion flux composition (expressed as percentage) was deduced by diving each ion specie flux to the total ion flux.

The influence of the average power on the Al target on the ion flux composition is shown in Figure 1 for a mass flow ratio He/(He+Ar) of 25%. He^+ ion flux is less than 1%. The ion flux composition changes with both the average power applied on the Al target and the sputtering gas composition, being more sensitive to the variations of the first process parameter, the input power. The composition of the total ion flux is dominated by Al^+ ions when the average power applied on the Al target is above 20 W. Figure 2 shows that, for the same sputtering gas composition, the total ion flux increases almost linearly with the increase of the power delivered to the Al target, while for the same power applied on the Al target, the total ion flux becomes larger as the Ar sputtering gas is replaced by He.

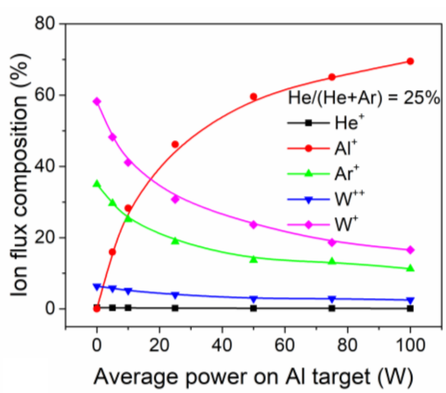

Figure 1 – Ion flux composition during dual-HiPIMS operation for different values of the average power applied on the Al target.

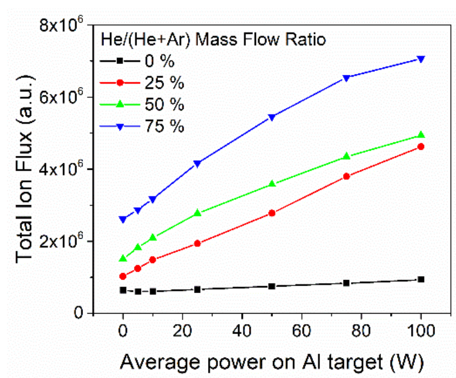

Figure 2 – Total ion flux measured during dual-HiPIMS operation for different values of the average power applied on the Al target and different sputtering gas compositions.

Characterisation of W and Al co-sputtered material in the gas phase by Mass Spectrometry in Ar-D_2 dual-HiPIMS

The experiments have been performed in D_2-Ar gas mixture in the same conditions as described above. The high electron density in HiPIMS D_2-Ar plasma is expected to enhance the dissociation of D_2 molecular gas, leading to multiple reaction products as D, D^+, D^-, D_2^+, D_3, D_3^+. The presence of multiple deuterium ion species (both positive and negative) has been confirmed by mass spectrometry measurements (Figure 3). The results in Figure 3 were obtained when operating only the W discharge (single HiPIMS mode) at an average power of 100 W.

The origin of deuterium positive ions D^+, D_2^+ and D_3^+ is in the vicinity of the target, in the ionization region, where the following reactions take place [1]:

$$D_2 + e^- \rightarrow D_2^+ + 2e^-$$
$$D_2^+ + D_2 \rightarrow D_3^+ + D$$
$$D_2^+ + D \rightarrow D_3^+$$
$$D + e^- \rightarrow D^+ + 2e^-.$$

D_2^+ and D_3^+ time-averaged ion energy distributions show only a peak at low ion energy of about 1 eV, which may be attributed to the above mentioned reactions. The time-averaged ion energy distribution functions are more different for D^+ and D^- ions which have a maximum around 1 eV and a very high energy tail which extends towards 500 eV. The high-energy tail structure is related to the D^- ions which are produced in the ionization region of the HiPIMS plasma from where they are repelled by the highly negative potential of the target. A fraction of the D^- energetic ions may be neutralized by collisions with plasma species and then ionized in their way towards the mass spectrometer leading to the occurrence of D^+ energetic ions.

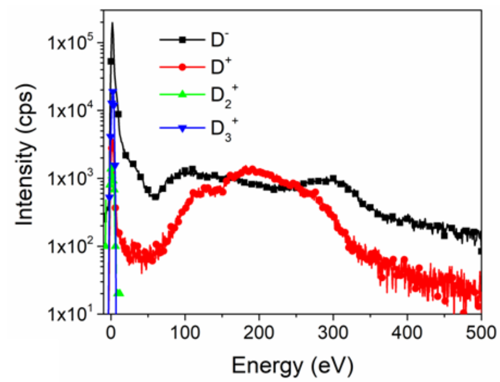

Figure 3 – IEDFs of deuterium ion species during single HiPIMS mode, with W target in Ar-D_2 gas mixture.

The ion flux composition during dual-HiPIMS operation with W and Al targets, for a mass flow ratio $D_2/(D_2+Ar)$ of 25%, is shown in Figure 4a. Only the most abundant ion species are plotted (D^-, D^+, Al^+ and W^+). The total ion flux is dominated by D^- ions when the average power applied on the Al target is below 60 W and by Al^+ ions for higher powers. Figure 4b shows that an increase of the input power on the Al target and/or the $D_2/(D_2+Ar)$ mass flow ratio leads to the increase of the total ion flux, similar behaviour as in the case of W and Al co-sputtered in Ar-He gas mixtures but with less pronounced increase, mainly due to the compound sputtering regime (specific for the presence of the reactive gas).

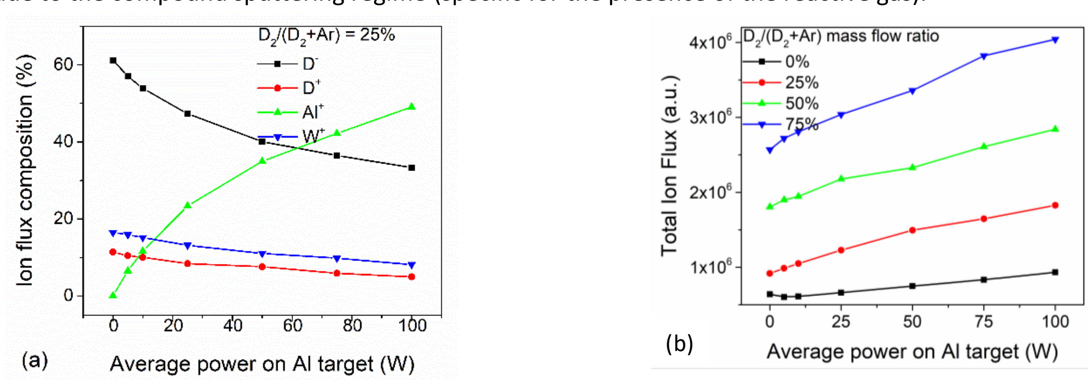

Figure 4 – (a) Ion flux composition and (b) the total ion flux during dual-HiPIMS operation with W and Al targets in Ar-D_2 gas mixtures, for different average powers applied on the Al target (100 W on the W target).

Probe measurements in the divertor region of COMPASS tokamak. Floating potential correlation analysis

This task was assumed under commitment appropriations (it was initially planned for 2018). Five probe arrays have been used for floating potential measurements. All arrays are installed in the divertor of COMPASS tokamak, 3 consisting of Langmuir probes and 2 consisting of Ball-pen probes. The correlation of the floating potential signals measured by different probes was investigated by normalized cross-correlation signal analysis. All measured signals exhibit large fluctuations. The correlation analysis allows calculating the frequency of these fluctuations and also allows evidencing the spatial propagation of the fluctuations. The analyzed signals, showed a fluctuation frequency of 5.68 kHz. The fluctuations of the floating potential propagate in poloidal direction, from the low field side to the high field side region, with an estimated velocity of about 0.3 km/s.

References

[1] C. Gorse and M. Capitelli, Physical Review A 46 (1992) 2176.

Optimization of treatment in respect to discharge stability and tungsten electrodes temperature using various helium/hydrogen plasma ratios

C. Stancu, V. Marascu, T.Acsente, M.Bazavan, G. Dinescu

National Institute for Laser, Plasma and Radiation Physics, 409 Atomistilor Str., PO Box MG-36, Magurele-Bucharest, 077125, Romania

WPPFC-RO

Outline

5. General objectives of the project
6. The objectives of the activities in the present stage of the project
7. Results
8. Conclusions

4. General objective of the project

The main objective of the project is the investigation of the tungsten surface when exposed to the helium/hydrogen discharges in well characterized and stable conditions in respect to sample temperature and plasma properties.

5. The objectives of the activities in the present stage of the project

In this stage of the project we focused on the discharge optimization in respect with treatments performed at stable exposure and temperature using various helium/hydrogen plasma ratios and on the modification of tungsten surfaces after exposure to these plasmas.

6. Results

In the previous stage of the project (2016) we demonstrated that hollow cathode discharges can be successfully used for simultaneous exposure of tungsten samples to high temperature and helium containing plasmas. An identified drawback of this approach was the short time stability of discharge, which affected the concluding on long term experiments. For the present stage it was proposed to address this problem, elaborating a new setup leading to optimization of the treatment.

3.1 Experimental setup

The new configured experimental setup consists in a water cooled vacuum chamber (Kurt Lesker company) pumped by a rotary pump which ensure an initial vacuum of $8*10^{-3}$ mbar. The chamber is equipped with CF ports and cooper gaskets. On the CF ports the viewports, the gauge, gas tube admission, and the connection to vacuum pump were mounted. In order to have a constant gas flow, the gas admission was realized by computer-controlled mass flow meters. To keep the stability of the hollow cathode plasma, a fine controlled valve which can keep the constant pressure was mounted between the chamber and the pump. The holder supporting the parallel plate hollow-cathode configuration was also actively cooled by water during plasma exposure. The electrodes were realized from tungsten plates (30x15x0.1 mm and 30x15x3 mm) placed face to face separated by a gap of 3 mm. The parameters used for tungsten exposure to plasma were: RF power = 300 W, pressure = 5-25 mbar, exposure time = 30 min. Tungsten surfaces were exposed to the hollow cathode discharge in He and in He with different concentration of H_2 (10-50%).

3.2. Discharge stability

Using the new presented configuration, we were able to generate and keep the hollow cathode discharge stable for more than 1 h. During plasma exposure procedure, we measured on the tungsten plates constant temperatures (around 1200^{o}C-1280^{o}C in the lateral of the electrodes), and more than 1500^{o}C in the zone were the plasma have the maximum intensity.

.

3.3 Tungsten surface investigation

The modification of the tungsten surfaces was investigated by optical microscopy and by profilometry (KLA Tencor P7 profilometer). The investigated zones were those that the tungsten has the highest temperatures (over 1500^{o}C measured by pyrometer). In case of profilometry, the following parameters were used to scan the surfaces: x=1000 µm, y=1000 µm, speed = 100 µm/s, y spacing = 5 µm, applied force = 2 mg. The measurements were realized in contact mode. When the tungsten surfaces were exposed to the He/H_2 mixture, the surface roughness increased by H_2 concentration increasing.

3.4. Evaluation of plasma parameters

During the tungsten plates exposure to plasma, optical emissions spectroscopy (OES) investigations were realized. The optical spectra were recorded using a Horiba Jobin Yvon FHR1000 spectrograph coupled with an ICCD Andor iDus DV420A-OE camera. From OES investigations we observe that the most intense lines lines corresponded to He. We found also the Balmer lines which correspond to Hγ, Hβ, Hα, some H_2 molecular bands, and some tungsten lines (400.87 nm, 404.56 nm, 407.43 nm, 424.43 nm, 426.93 nm, 429.46 nm), which have a low intensity.

The electronic temperature Te was approximated by the plasma excitation temperature. It was deduced from the ratio of the intensities of the W spectral lines. In the OES spectra recorded in the discharge were identified a number of WI transitions, their intensity strongly reducing (down to zero) when the amount of the H_2 is increased. Still, the transitions 5d5(6S)6s - 5d5(6S)6p (400.8749) and 5d5(6S)6s - 5d5(6S)6p (429.4605) present a recordable signal following to H_2 injection in the discharge. The estimated electronic temperature increased from 2895 K in sole He discharge up to 4297 K when 10% H_2 is added. Increasing the H_2 content to 25% and 50% the calculated electronic temperature increases up to 60000K respective 2300 K; these last two values are questionable due to the incertitude in evaluation of the integral intensities for very low emission lines. Indeed, for reliable results the lines should be well isolated, closed to each other in the spectra, and originating from upper energy levels with large energy difference. Here, it is mandatory to mention that the approach was affected by many errors, because the upper energy levels are closed to each other, and the hypothesis of thermal equilibrium is not verified. A better approach will be based on the analysis of profiles of hydrogen lines, which is foreseen in future investigations. These can be compared with previous results (2016) obtained by Langmuir probe measurements.

4. Conclusions

Optimization of treatment in respect to discharge stability and electrodes temperature having various helium/hydrogen plasma ratios was realized using a new wall water cooling vacuum chamber. A long-time operation in stable conditions (tested for more than 1 h) of the hollow cathode discharge was obtained. Tungsten samples were exposed to the hollow cathode discharge in He and in He/H_2 mixture with different concentration of H_2 (10-50%). As shown by optical microscopy, the surfaces were differently affected, in function of plasma gas mixture, and surface temperature. From profilometry measurements it was observed that the surface roughness increased with the H_2 concentration. OES spectra were recorded. From spectra it was observed that the most intense lines correspond to the He, but we found lines which correspond to hydrogen Balmer series (Hγ, Hβ, Hα), to H_2 molecules, and some tungsten lines with a low intensity. The tungsten lines, proved on surface erosion, and were used for evaluation of plasma parameters.

JT-60SA Conceptual Design development

S. Soare[1]

[1] *National Institute for Cryogenics and Isotopic Technologies, ICIT*

WP-SA

1. Introduction

The polarimeter system development started few years ago and has the unique capability to provide information on plasma magnetic structure of plasma using INTERNAL measurements. The operation principle is based on:

- the Faraday Rotation Effect; it is the only technique that can provide the magnetic field information using internal measurements during the entire plasma cycle (start-up, flat-top and ramp-down).
- the Cotton-Mouton phase shift; the plasma is birefringent so a laser beam passing through plasma become elliptically polarised due to the interaction of the laser beam with the perpendicular components to the propagation direction. So the two orthogonal components of the polarisations have a phase shift called Cotton-Mouton angle. Due to these two techniques the polarimeter diagnostic could be evolve at the status of basic machine control (protection and density feedback control). The vertical channels can provide absolute electron line-integrated measurements fringe jumps free similarly as is already used on JET fusion experiment[1].

The results obtained during 2017 refer to: laser wave-length selection and to q-profile reconstruction for last configuration; specific cases: **A)** partial system 9 horizontal + 1 vertical channel & **B)** minimum system 2 horizontal + 1 vertical channel.

2. Wave length selection

In the FIR domain there are only a small number of lasers available. In this study we concentrated in analysing two wavelengths: 194.7µm (using Deuterated Cyanide lasers such as JET or ToreSupra) and 118.8 µm (using a methanol laser as planned in ITER) as the lasers at these wavelengths are known to deliver large power in the range if 100-500mW. Sensitivity study simulation were performed by increasing artificially the number of channels to 17 (figure 1A) in order to obtain a better profile for the entire plasma radius (or range of normalised radius rho from 0 to 1) of the Faraday Rotation angle for the wavelength of 194.7 µm.

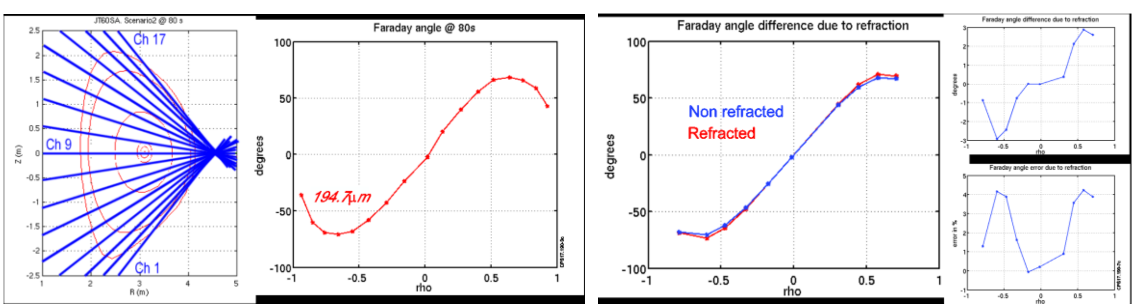

Figure 1a&1B Faraday rotation angle (double pass) estimated values at timeframe 80s in the flattop (right) on a poloidal 17 channel Polarimeter (left) that the instrument would actually measure / 1B Impact of beam deviation on Faraday Angle measurements

The advantage of increasing the wavelength of the laser radiation comes also with a negative effect: refraction. This effect is caused by the plasma refractive index and is varying with the square of the wavelength and not only causes the beam deviation but also introduces measurements errors on the Faraday angle.

After careful consideration it was decided to abandon further studies for the smaller wavelength of 118.8 µm because the Faraday angle was too small and low dynamic range for some scenarios even at flat-top.

Also, there were no strong negative implications for using 194.7 µm as the refraction as this wavelength is still small, Cotton-Mouton effect is measurable and does not affect the Faraday Angle measurement (figure 1B) and Gaussian beam expansion induces reasonable size of the corner cube reflectors (CCR) and vacuum windows.

3. q-profile reconstruction for last configuration

In figure 3 the last geometry configuration is displayed (corresponding to the final study) and clearly shows a different channel distribution for lateral channels, case A.

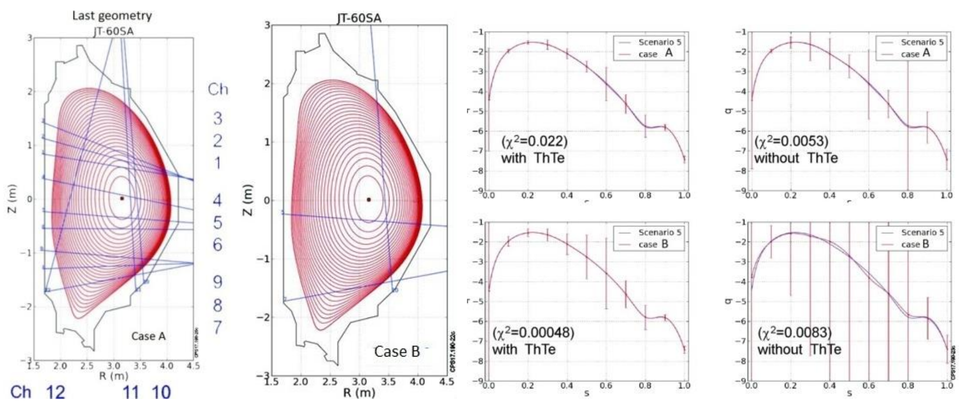

Figure 3A Last geometry proposed with channel number localisation at CCRs and windows (blue colour), case A and B / 3B q-profile for sensitivity study of the last configuration, cases A and B

For this study it was considered the possibility of the instrument not having all channels fully operational during operation. This leads to the worst case scenario having the minimum system left with 2 horizontal + 1 vertical channels, case B, fig. 3A.

Given the specific nature and effect in the reconstruction process of line integrate and point measurements, both results with and without including Thomson scattering information are shown in fig. 3B for both cases. Unfortunately, mechanical limitations in the laser-path access cannot provide additional or different vertical channels (up to five as in the previous studies) that might improve this result. Even though $_{\chi}2$ is quite small, the error bars can be large.

When running simulation in a partial system as Case A (10 channels) we obtain a similar result as in Case A (12 channels, full system). The minimum configuration of the polarimeter (Case B) contains only three channels and the reconstruction required twice the number of steps necessary for the solution for Case A as fewer diagnostics information provide a weaker constraint to the solution and degeneracy comes into play more strongly

4. Conclusions

A 194.7 µm FIR polarimeter system with up to twelve channels at last configuration can be envisaged in JT-60SA with a design that requires nine vacuum vessel windows. One vertical channel requires in-vessel mirrors and the impact of this channel needs to be investigated from a point of view of cost/benefit in short and long term.

PRELIMINARY THOMSON SCATTERING DIAGNOSTICS EVALUATION

S. Soare[1]

[1] *National Institute for Cryogenics and Isotopic Technologies, ICIT*

WP-SA

Thomson scattering diagnostics

Profiles of electron density, ion temperature, electron temperature and toroidal rotation will be measured by Thomson scattering systems (TMS), electron cyclotron emission diagnostics (ECE) and charge exchange recombination spectroscopy (CXRS) systems.

The development of the Thomson Scattering diagnostics is a shared work between Japan and EU. The EU part consists of: optical system including special stage and port plug including installation jig, Installation of optical system and port plug, optical fibres and polychromatorsystem including detector (APD) for 96 channels

The main components of the diagnostics are located in the horisontal port no. P18 and P1 with the YAG laser path falling into the field of view, fig. 1.

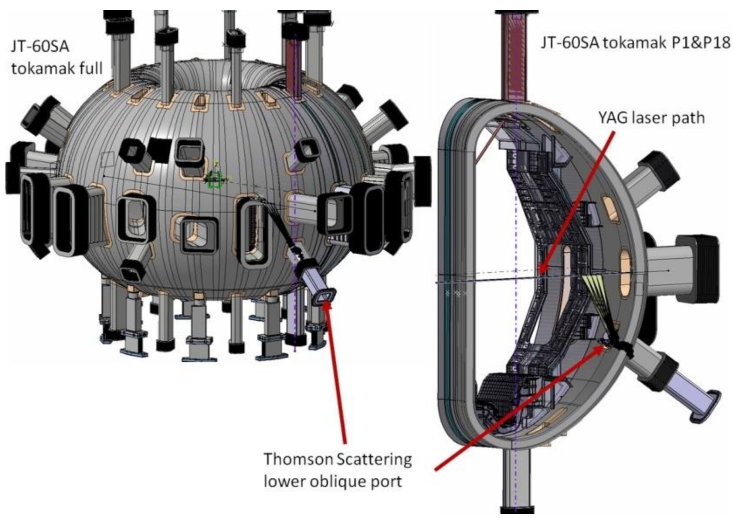

Figure 1 location of Thomson Scattering and YAG laser path

In accordance with this laser path, P1 lower oblique, P2 horizontal and P5 horizontal ports are assigned for collecting Thomson scattering light from the outer edge (high field side), core, and inner edge (low field side) of plasmas, respectively (fig. 2)

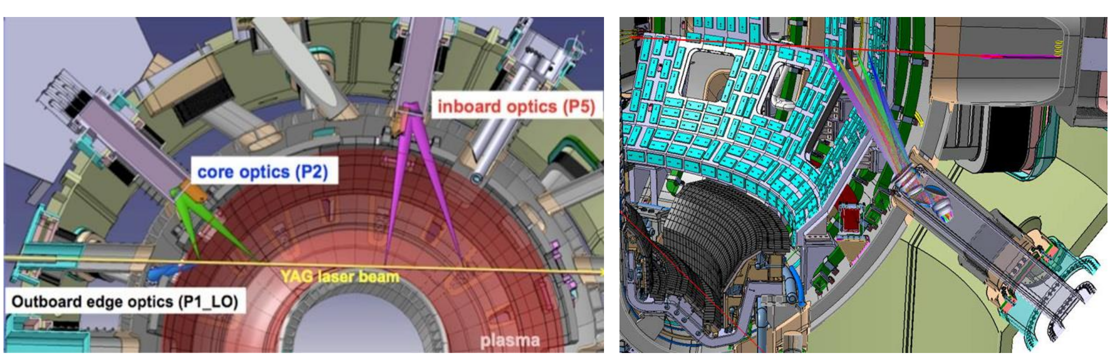

Figure 2 Collection of optics of Thomson scattering along YAG laser path, vertical section

The optics is based on compact lens system based on small Petzval lens (stop position) can be install in small port-plug and two flat mirrors, fig. 3A. The optics is located inside the port plug that has at the plasma end a cover glas and a vacuum mirror protected by a metallic cover driven by a pneumatic actuator, fig. 3B.

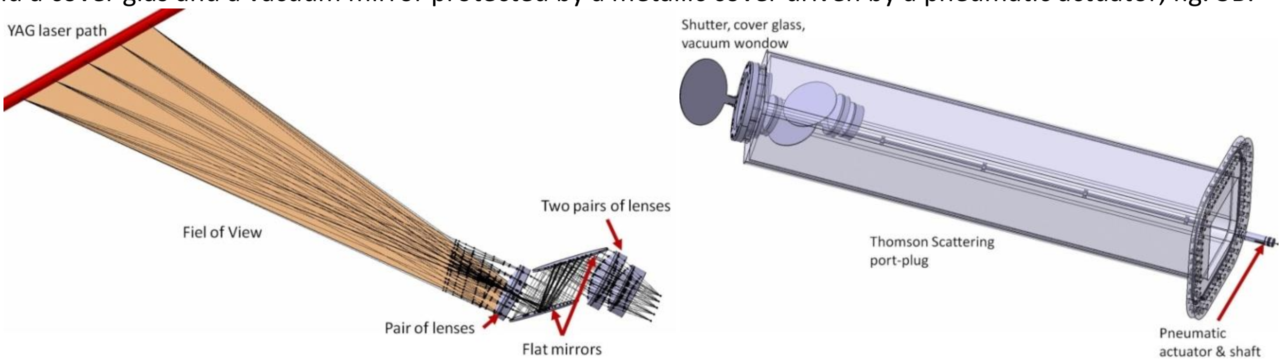

Figure 3A &3B Main components of optics & port plug

At the evaluation it was found that:

- clearances to the port plug are ranging from 19mm to 100mm, fig. 4.
- the acceleration assumed (earthquake) are: at the port of cryostat: 0.6G in horizontal direction + 0.4G in vertical direction; On the stage outside cryostat: 0.4G in horizontal direction only
- 5.5MA disruption generating

-

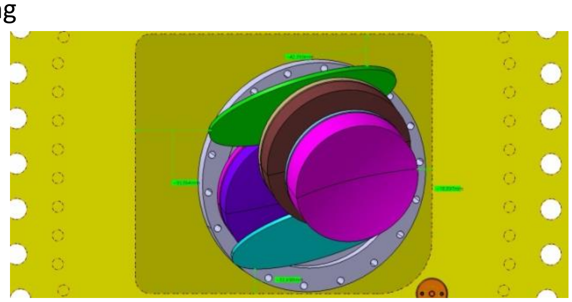

Figure 4 Clearances of the optics (mirrors and lenses) to the inner port plug surfaces

The differences between the design and the manufactured lower oblique port (P1) cryostat flange are up to 4 mm.

Conclusions

Port, port-plug, YAG laser path and optics CAD data exchange was done through the DMS system. An initial evaluation was carried out regarding the clearances between the existing components, i.e. optics and nearby items. Also the accelerations (earthquake) at the cryostat port level were received as well as the disruption characteristics.

POLARIMETER CAD MODEL UPGRADE / SIMULATIONS & UPGRADES

S.Soare[1]

[1] *National Institute for Cryogenics and Isotopic Technologies, ICIT*

WP-SA

1. Introduction

The polarimeter system development started few years ago and has the unique capability to provide information on plasma magnetic structure of plasma using INTERNAL measurements. The operation principle is based on the Faraday Rotation Effect: a magnetised plasma is optically active and a linear polarised laser beam sent through a plasma suffer a rotation of the polarisation plane due to the interaction of the field component along the propagation direction and the angle of rotation is called Faraday Rotation angle. These measurements are the only ones that can provide the magnetic field information using internal measurements during the entire plasma cycle (start-up, flat-top and ramp-down).

2. 2nd Study of channel localisation

The solution of the 1st study was deemed not feasible due to the following reasons: the channel trajectories were not in the same poloidal plan are not acceptable as this complicates the magnetic reconstruction AND the in-vessel components required for steering the beams (mirrors) for the vertical channels were very complicated and would have added a substantial cost to the system including a potential very difficult alignment (first commissioning at installation and re-commissioning in long term)

Therefore the work was dedicated to try to eliminate as much as possible the requirements for the in-vessel mirrors.

In this new configuration there are only three vertical channels from which two of them passing through the same window and pointing to two different corner-cube reflectors. The third vertical channel had still two in-vessel mirrors for beam steering as shown in figure 1A.

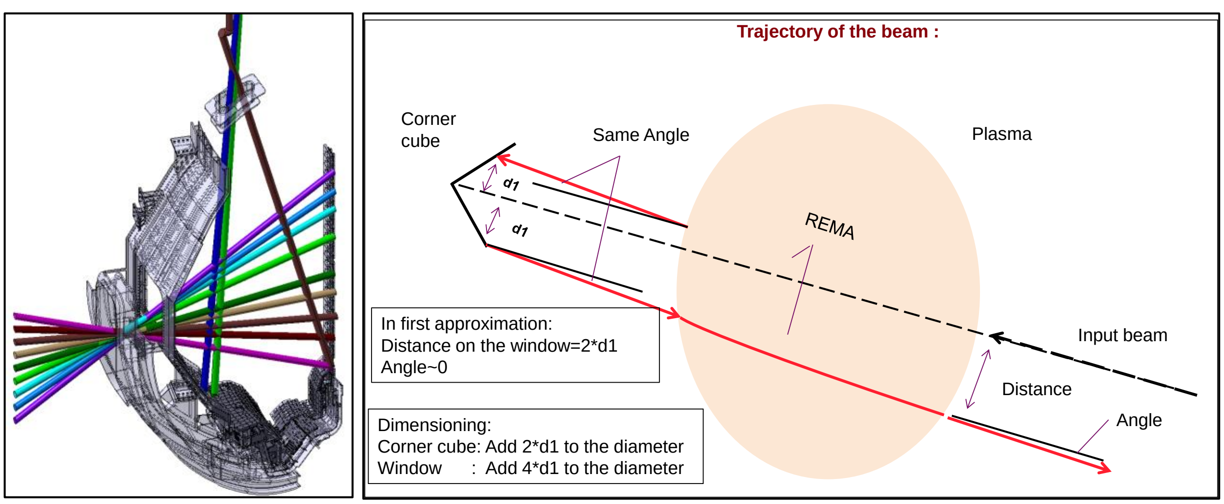

Figure 1A. 2nd study of polarimeter channels (most of the vacuum vessel is hidden); Fig. 1B Beam deviations due to plasma

Several calculations were performed on the deviation of an infrared beam at the CC reflectors using a plasma ray-tracing code developed for microwaves (FCE and Hybrid Heating called REMA4). The input required for these simulations were: plasma parameters (JT60 plasma equilibrium, electron density profile) AND beam (wave-length, mode, initial trajectory), figure 1B.

Figure 2A depicts an example of this simulation where is displayed the maximum deviation (4mm in this case) and electron density profile shape

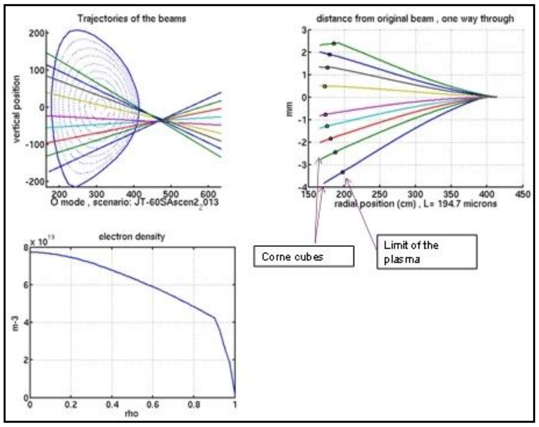

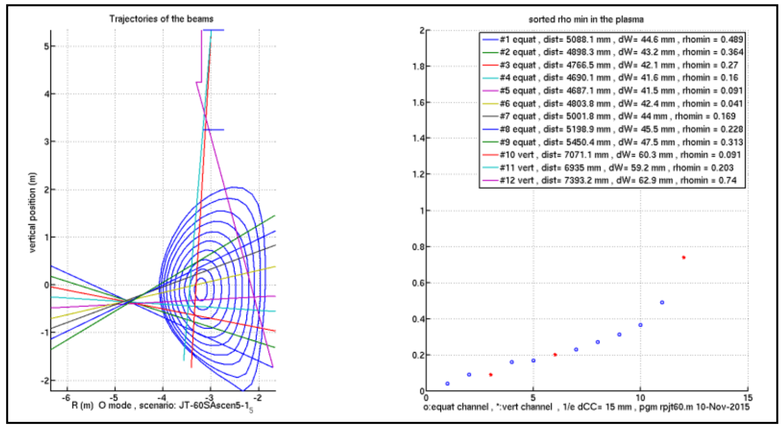

Figure 2A Example: beam deviation for lateral channels in a Scenario 2 plasma; Fig. 2B Positions of the beams in the plasma Scenario 5 (dist is the beam path from the CC to the windows, dW is the 1/e is the Gaussian beam diameter on the windows, rhomin = normalised radius tangent with the beam)

The Gaussian beams were calculated using Veron formulas, figure 2B. The conclusions of this 2nd study are as follows:

- To achieve 99% intensity propagation of the beam on the CC , the optical diameter of these components must be in the range of 45-50 mm
- Vacuum Windows diameter must be 120mm and 160mm and the centres spaced at minimum of 150mm and 200mm for lateral and vertical channels respectively
- There are not enough rho points in the interval [0.4-0.7] so further optimisation was required

3. Conclusions

A suitable CAD model for a random octant has been obtained from JAEA. On this model the no-go regions have been marked and should be observed in the future. Accommodating these strict geometric boundaries a polarimeter system model with a reduced numbers of channels (12) channels can be considered, at this time, suitable for JT60SA. Further modelling to refine the channels distribution will be done.

Romanian participation at EUROfusion WPISA and complementary research / WPISA-RO-P

V.Pais[1], V.Stancalie[1], C.Iorga[1]

[1] *National Institute for Laser, Plasma and Radiation Physics, Atomistilor 409, P.O.Box MG36, Magurele-Ilfov, 077125 Romania*

WPISA-RO-P

Development of modeling codes for ITER, requires a complex computation infrastructure. The current infrastructure is composed of a server cluster, having a large number of processing nodes, two parallel file systems and advanced mechanisms for access to resources. In this context, the European project WPISA (Infrastructure Support Activities) aims at improving the existing infrastructure by developing and integrating new modules and applications in order to better use existing hardware resources and to create a collaborative environment for creating complex simulation codes. In previous projects, a “portal” system was developed to allow the users to access resources offered by the computing cluster through a web interface.

The current project aims at improving the existing functionalities available through the “portal” and development of new applications that will be integrated in the “portal” as well.

The current stage of the project was focused on performing maintenance on the existing Portal infrastructure and migration of the software project management component, GForge, to the latest version. This was needed in order to be able to integrate new functionalities available.

The GForge platform is used to manage software projects. This includes: mailing lists, wiki pages, subversion repositories, project members list, trackers. Version 5 that was previously implemented is no longer supported by the producer. Therefore, new features and patches can’t be applied on this version.

Previously, work began on upgrading to version 6. However, due to changing the hardware platform of the Gateway cluster, moving it from Garching to Bologna on new hardware, the final integration was not completed. Furthermore, on the new Gateway there are different mechanisms for user authentication and authorization. This required to start the integration process from scratch.

The main steps for a successful upgrade involved: migrating the old database, migrating subversion repositories, migrating mailing lists. All these steps are not trivial to implement due to significant changes in software and database structure.

Apart from technical challenges, rigorous testing was needed in order to make the transition as easy as possible for existing users. Solving issues related to upgrading the various components involved direct communication with GForge Group.

The GForge system must be integrated with the Portal. Therefore, the Single Sign On component of the Portal must be used as the authentication source for GForge. The SSO integration feature for GForge changed from the 5 version. Therefore, some work was needed to perform the actual integration.

The old version of GForge used a file based configuration system, with configuration directives being written in various files. With the new GForge version, the configuration system was moved to the database and access to it was made available through a tool called “gf-config”. For the upgrade purposes, a dedicated tool was used to import the file based configuration settings in the database.

During the 2017 stage of the project, significant progress has been made towards completely migrating to the latest GForge version. There still remained more testing to be performed on the system in order to ensure an easy transition for users, without them noticing any issues.

Some changed or missing features that were discovered through our testing, could pose some problems to users, therefore additional work may be required to minimize the impact. This includes features such as: tracker items are always listed in ascending chronological order, a new submission to a tracker item is not emailed to the person posting it, when an email does arrive (due to a reply on a tracker item), the email does not contain all the conversation. These issues were opened with GForge Group developers and waiting on their comments. Nevertheless, these are not stopping issues, and the transition to the new version continued as planned.

A good collaboration with the GForge Group developers helped us speed up the migration process for specific GForge features. Similarly a good collaboration with the Gateway operating team helped us speed up the integration with the Gateway specific resources such as user authentication and authorization via specific mechanisms, such as LDAP. Through these fruitful collaborations it is expected to finalize all migration activities in 2018 and will be reported in the next year's report.

Construction of a portal interface based on noSQL database

V.Pais[1], V.Stancalie[1], C.Iorga[1]

[1] *National Institute for Laser, Plasma and Radiation Physics, Atomistilor 409, P.O.Box MG36, Magurele-Ilfov, 077125 Romania*

WPISA-RO-C

The present project aims to investigate the usage of noSQL databases for portal and data applications used in fusion research. These are new and innovative technologies for high performance databases, easily scalable for both storage and high speed requirements. Currently, a growing number of activities are investigating the use of such databases for their purposes. However, fusion related applications have specific characteristics, which may or may not fit with the specifics of this kind of databases. In this context, this project aims at investigating on various aspects related to fusion research and see how well noSQL databases can be used to increase performance of codes or to improve the user experience.

One of the key aspects of WPISA work package is to maintain a user interface for users to access the computing platform. This interface is presented in the form of a web Portal that integrates various tools running on the computing cluster available to users. Currently, this portal is using standard, proven, technologies, relying on traditional SQL databases, namely Postgres and MySQL databases, and other storage systems developed within the community. One of the specific goals of this project is to investigate how this portal will behave if the underlying data storage system is moved to a noSQL database.

Structuring atomic data into traditional database features, like tables, can be easily accomplished for user related tasks. However, for simulation codes it's usually better to have complete files (either text or binary). Especially in the case of binary files, these can be accessed efficiently in high performance computing (HPC) environments, using specific functionality, such as the one offered by MPI implementations. In any case, a database dedicated to storing atomic data, must offer both a traditional approach to modelling the internals of data files and the possibility to store complete text or binary files. Furthermore, access to stored resources must be allowed in a parallel way, in order to allow for usage inside HPC environments.

The first stage of this project was dedicated to identifying suitable noSQL databases and report on their potential for usage in fusion related applications and user interfaces. For this purpose, they must be able to handle Big Data issues and offer a high performance query engine as well as a stable and mature application programming interface (API). As a result from the analysis, the MongoDB noSQL database was selected for usage throughout the project.

Current work was focused on finalizing requirements and preparing data to be loaded in the portal.

A record in MongoDB is a document, which is a data structure composed of field and value pairs. MongoDB documents are similar to JSON objects. The values of fields may include other documents, arrays, and arrays of documents. The advantages of using documents are: a) documents (i.e. objects) correspond to native data types in many programming languages; b) embedded documents and arrays reduce need for expensive joins; c) dynamic schema supports fluent polymorphism.

Based on these characteristics of MongoDB, a document based data model was created. This model allows for both metadata and actual physics data to be stored inside the noSQL database. A total of 5 document collections (corresponding to tables in traditional databases) were needed for this purpose.

Expected usage requirements were formulated based on existing data handling applications, such as: a) only authenticated users are able to upload or edit data; b) all users are able to explore data; c) available information can be explored either by searches or by relations implemented using tags; d) A set of pre-defined tags must be prepared in order to facilitate the user's mission when uploading new data.

Part of constructing the application, data must be gathered and prepared to be loaded in the database. This involves both data files, associated metadata and metadata files as outlined in the previous report.

Because this project's aim is to test the applicability of MongoDB to fusion application, fusion related data needed to be identified and prepared for the application's purposes, such as: a) carbon collision strengths in the form of a data file containing target states, target states modified by degeny, Line Strengths (au), total collision strengths.; b) cross sections for electron impact excitation of 3P0-3P1 of ground configuration in C, containing two columns: coll.en (Ryd), cross section (a0^2); c) cross sections for electron impact excitation of 3P0-3P2 of ground configuration in C containing Cross sections (a0^2) as function of energy (Ryds). Transition 3P0-3P2 of ground configuration in C atoms. This data file contains two columns: coll.en (Ryd), cross section (a0^2); d) carbon calculations with DARC (this is the output from DARC, the Dirac Atomic R-matrix Codes, and contains levels energy (in a.u., Ryds, eV) contribution from: Coulomb, Breit and QED terms, radiative transition probabilities, line strengths, oscillator strengths in length and velocity frame); e) Other simulation results using the R-MATRIX codes; f) articles published by members of our research group related to fusion research aspects and especially related to the available data files.

These files were retrieved from various locations and uploaded inside the prepared MongoDB database. Furthermore, additional data, such as tags were prepared and added to the stored information.

The current stage of the project followed the modeling stage and prepared the database by loading data. The next stage of the project will focus on the actual implementation of the interface in order to allow the user to interact with stored information in order to perform queries and modifications as needed.

Romanian participation to EUROfusion WPEDU

G. Dinescu

National Institute for Laser, Plasma and Radiation Physics, 409 Atomistilor Str., PO Box MG-36, Magurele-Bucharest, 077125, Romania

Outline

9. General objectives of the project
10. The objectives of the activities in the present stage of the project
11. Results
12. Conclusions

7. General objective of the project

The project is part of Work Package Education of PhD and Pre-doctoral of the Education Programme (WPEDU) and its scope is to support doctoral and pre-doctoral students to realize their thesis research projects in the frame of fusion research institutions and universities, part of EUROfusion Consortium. It focusses on promoting education of young researchers and an appropriate spread over of the topics relevant for fusion engineering and physics

8. The objectives of the activities in the present stage of the project

In the reporting period the activity focused on the research doctoral and pre-doctoral activities, mentoring and training of the PhD and MSc researchers in the laboratories, in agreement with the specific of their research themes.

9. Results

3.1 Training in experienced teams working in fusion technology

The research plans of the young members of the project team were designed according to the existing expertise in the fusion research in the IAP Research Unit (research groups at Institute for Laser, Plasma and Radiation Physics, Institute for Materials Science, Institute for Nuclear Physics and Engineering). The performed activity on selected topics which referred to materials for Tokamak walls, techniques for coating deposition and characterization (from materials with relevance for fusion W, Be, nitrides, markers...), characterization techniques specifically applied to nuclear materials, study of particles and dust fabrication, transport and mobilization, theoretical studies concerning plasma confinement, etc:

3.2 Ensuring the educational path in agreement with the rules of the Doctoral programme

The educational path was assured, according to the MSC and PHD rules. Research experiments were designed and performed, such us that the team members elaborated the due Research Reports, Dissertations, PhD theses. All the students enrolled in the programme were mentored, monitored and supervised.

3.3. Finalized theses and recruitment of new team members

A PhD thesis was finalized, a Doctoral degree was granted. A ne MSC researcher was recruited.

4. Conclusion and future plans

We will continue the research, educational and training activities with all the young researchers we have enrolled in the project. In 2018 the main focus will be on finalizing theses and recruiting new PhD candidates. Also, we intend to increase the participation of young researchers to international scientific events.

Papers

[1] C.V. Atanasiu and L. E. Zakharov, Response of a partial wall to an external perturbation of rotating plasma, Phys. of Plasmas 20, 092506 (2013).

[2] C.V. Atanasiu, L.E. Zakharov, K. Lackner, M. Hoelzl, E. Strumberger, Simulation of the electromagnetic wall response to plasma wall-touching kink and vertical modes with application to ITER, 59th Annual Meeting of the APS Division of Plasma Physics, Milwaukee, WI, US, October 23-27, 2017 (oral presentation).

[3] C.V. Atanasiu, L.E. Zakharov, K. Lackner, M. Hoelzl, E. Strumberger, Wall currents excited by plasma wall-touching kink and vertical modes, JOREK Meeting, Prague - 20-24/03/2017 (oral presentation).

[4] C.V. Atanasiu, L.E. Zakharov, K. Lackner, M. Hoelzl, F.J. Artola, E. Strumberger, X. Li, Modelling of wall currents excited by plasma wall-touching kink and vertical modes during a tokamak disruption, with application to ITER, 17th European Fusion Theory Conference, Athens – Greece, October 9-12, 2017 (oral presentation).

[5] M. Avrigeanu and V. Avrigeanu, Phys. Rev. C 95, 024607 (2017); arXiv:1702.00560 .

[6] V. Avrigeanu and M. Avrigeanu, Phys. Rev. C 96, 044610 (2017); arxiv:1710.01140 .

[7] Baran V. V., Palade D. I., Vlad M., Spineanu F., Trapped Electron mode turbulence: test mode approach, JET pin board, submitted 2017.

[8] Brezinsek, S., Coenen, J.W., Schwarz-Selinger, T., Schmid, K., Kirschner, A., Hakola, A., Tabares, F.L., Van Der Meiden, H.J., Mayoral, M.-L., Reinhart, M., Tsitrone, E., Ahlgren, T., Aints, M., Airila, M., Almaviva, S., Alves, E., Angot, T., Anita, V., Arredondo Parra, R., Aumayr, F., Balden, M., Bauer, J., Ben Yaala, M., Berger, B.M., Bisson, R., Björkas, C., Bogdanovic Radovic, I., Borodin, D., Bucalossi, J., Butikova, J., Butoi, B., Čadež, I., Caniello, R., Caneve, L., Cartry, G., Catarino, N., Čekada, M., Ciraolo, G., Ciupinski, L., Colao, F., Corre, Y., Costin, C., Craciunescu, T., Cremona, A., De Angeli, M., De Castro, A., Dejarnac, R., Dellasega, D., Dinca, P., Dittmar, T., Dobrea, C., Hansen, P., Drenik, A., Eich, T., Elgeti, S., Falie, D., Fedorczak, N., Ferro, Y., Fornal, T., Fortuna-Zalesna, E., Gao, L., Gasior, P., Gherendi, M., Ghezzi, F., Gosar, Ž., Greuner, H., Grigore, E., Grisolia, C., Groth, M., Gruca, M., Grzonka, J., Gunn, J.P., Hassouni, K., Heinola, K., Höschen, T., Huber, S., Jacob, W., Jepu, I., Jiang, X., Jogi, I., Kaiser, A., Karhunen, J., Kelemen, M., Köppen, M., Koslowski, H.R., Kreter, A., Kubkowska, M., Laan, M., Laguardia, L., Lahtinen, A., Lasa, A., Lazic, V., Lemahieu, N., Likonen, J., Linke, J., Litnovsky, A., Linsmeier, C., Loewenhoff, T., Lungu, C., Lungu, M., Maddaluno, G., Maier, H., Makkonen, T., Manhard, A., Marandet, Y., Markelj, S., Marot, L., Martin, C., Martin-Rojo, A.B., Martynova, Y., Mateus, R., Matveev, D., Mayer, M., Meisl, G., Mellet, N., Michau, A., Miettunen, J., Möller, S., Morgan, T.W., Mougenot, J., Mozetič, M., Nemanič, V., Neu, R., Nordlund, K., Oberkofler, M., Oyarzabal, E., Panjan, M., Pardanaud, C., Paris, P., Passoni, M., Pegourie, B., Pelicon, P., Petersson, P., Piip, K., Pintsuk, G., Pompilian, G.O., Popa, G., Porosnicu, C., Primc, G., Probst, M., Räisänen, J., Rasinski, M., Ratynskaia, S., Reiser, D., Ricci, D., Richou, M., Riesch, J., Riva, G., Rosinski, M., Roubin, P., Rubel, M., Ruset, C., Safi, E., Sergienko, G., Siketic, Z., Sima, A., Spilker, B., Stadlmayr, R., Steudel, I., Ström, P., Tadic, T., Tafalla, D., Tale, I., Terentyev, D., Terra, A., Tiron, V., Tiseanu, I., Tolias, P., Tskhakaya, D., Uccello, A., Unterberg, B., Uytdenhoven, I., Vassallo, E., Vavpetič, P., Veis, P., Velicu, I.L., Vernimmen, J.W.M., Voitkans, A., Von Toussaint, U., Weckmann, A., Wirtz, M., Založnik, A., Zaplotnik, R., Plasma-wall interaction studies within the EUROfusion consortium: Progress on plasma-facing components development and qualification, Nuclear Fusion 57-11 (2017) 116041.

[9] S. Brezinsek, et all, Plasma-Wall Interaction Studies within the EUROfusion Consortium: progress on Plasma-Facing Components development and qualification/NUCLEAR FUSION Volume: 57 Issue: 11 Article Number: 116041 Published: NOV 2017".

[10] G. Carro, A. Muñoz, M.A.Monge, B. Savoini, A Galatanu, M. Galatanu, R. Pareja, Thermal conductivity and diffusivity of Cu-Y alloys produced by different powder metallurgy routes, Fusion Engineering and Design 124 (2017) 1156.

[11] S. Coda, J. Ahn, R. Albanese, .., I. G. Miron et al, Nucl Fusion 57, 102011 (2017)

[12] J. Coenen, G. Matthews, K. Krieger, D. Iglesias, P. Bunting, Y. Corre, S. Silburn, I. Balboa, B. Bazylev, N. Conway, I. Coffey, R. Dejarnac, E. Gauthier, J. Gaspar, S. Jachmich, I. Jepu, C. Makepeace, R. Scannell, M. Stamp, P. Petersson,

R. Pitts, S. Wiesen, A. Widdowson, K. Heinola, A. Baron-Wiechec, Transient induced tungsten melting at the Joint European Torus (JET), Physica Scripta, T170; Article Number: 014013, DOI: 10.1088/1402-4896/aa8789, Dec. 2017

[13] Croitoru A. M., Effects of magnetic drifts on ion transport in tokamak turbulent plasmas, Romanian Journal of Physics, submitted 2017.

[14] M. Curuia, T. Craciunescu, S. Soare, V.L. Zoita, V. Braic, D. Croft, A. Fernandes, J. Figueiredo, V. Goloborod'ko, G. Gorini, S. Griph, V. Kiptily, I. Lengar, S. Mianowski, J. Naish, R. Naish, M. Nocente, R. C. Pereira, V Riccardo, K. Schoepf, B. Santos, M. Tardocchi, V. Yavorskij, I. Zychor, Upgrade of the tangential gamma-ray spectrometer beam-line for JET DT experiments, Fus. End. Design, 123, 2017, 749-753

[15] P. Dinca, C. Porosnicu, B. Butoi, I. Jepu, V. Tiron, O. G. Pompilian, I. Burducea, C. P. Lungu, I.-L. Velicu, Beryllium-Tungsten Study on Mixed Layers obtained by m-HiPIMS/DCMS Techniques in a Deuterium and Nitrogen Reactive Gas Mixture Surface and Coatings Technology, Volume 321, 15 July 2017, Pages 397-402;

[16] M. Galatanu, M. Enculescu, A. Galatanu, Thermo-physical properties of Cu-ZrO2 composites as potential thermal barrier materials for a DEMO W-monoblock divertor, Fusion Engineering and Design 127 (2018) 179.

[17] M. Galatanu, M. Enculescu, G. Ruiu, B. Popescu, A. Galatanu, Cu-based composites as thermal barrier materials in DEMO divertor components Recent progress in fusion, Fusion Engineering and Design 124 (2017) 1131.

[18] G. Giruzzi et al., Physics and operation oriented activities in preparation of the JT-60SA tokamak exploitation, Nuclear Fusion Volume: 57 Issue: 8 Published: 2017, DOI: 10.1088/1741-4326/aa7962.

[19] S.G. Greculeasa, P. Palade, G. Schinteie, A. Kuncser, A. Stanciu, G.A. Lungu, C. Porosnicu, C.P. Lungu, V. Kuncser, Significant change of local atomic configurations at surface of reduced activation Eurofer steels induced by hydrogenation treatments Applied Surface Science, Volume 402, 30 April 2017, Pages 114-119

[20] K. Heinola, A. Widdowson, J. Likonen, T. Ahlgren, E. Alves, C. Ayres, A. Baron-Wiechec, N. Barradas, S. Brezinsek, N. Catarino, J. Coad, C. Guillemaut, I. Jepu, S. Krat, A. Lahtinen, G. Matthews, Experience on divertor fuel retention after two ITER-Like Wall campaigns, Physica Scripta, T170 Article Number: 014063, Dec. 2017

[21] K. Heinola, J. Likonen, T. Ahlgren, S. Brezinsek, G. De Temmerman, I. Jepu, G. Matthews, R. Pitts, A. Widdowson, Long-term fuel retention and release in JET ITER-Like Wall at ITER-relevant baking temperatures, Nuclear Fusion, Volume: 57 Issue: 8, Article Number: 086024, DOI: 10.1088/1741-4326/aa747e, Aug. 2017

[22] M. Hoelzl, P. Merkel, G.T.A. Huysmans, C.V. Atanasiu et al., Non-linear simulations of MHD instabilities in Tokamaks including Eddy current effects and perspectives for the extension to Halo currents, Journal of Physics: Conference Series 401, 012010 (2012).

[23] F.Iannone, G.Bracco, C.Cavazzoni, R.Coelho, D.Coster, O.Hoenen, A.Maslennikov, S.Migliori, M.Owsiak, A.Quintiliani, B.Palak, V.Pais, F.Robin, E.Rossi, I.Voitsekhovitch , "MARCONI-FUSION: The new high performance computing facility for European nuclear fusion modelling", 2018, Fusion Engineering and Design, Vol 129, Pages 354-358, 2018

[24] C. Iorga, V. Stancalie, "Atomic data and line intensities for the S V ion", 2017, ATOMIC DATA AND NUCLEAR DATA TABLES Volume: 115, Pages: 1-286; DOI: 10.1016/j.adt.2016.06.002;Published: MAY-JUN 2017

[25] Kazakov, Y.O., Ongena, J., Wright, J.C., Wukitch, S.J., Lerche, E., antsinen, M.J., Van Eester, D., Craciunescu, T., Kiptily, V.G., Lin, Y., Nocente, M., abais, F., Nave, M.F.F., Baranov, Y., Bielecki, J., Bilato, R., Bobkov, V., Crombé, K., Czarnecka, A., Faustin, J.M., Felton, R., Fitzgerald, M., allart, D., Giacomelli, L., Golfinopoulos, T., Hubbard, A.E., Jacquet, P., Johnson, ., Lennholm, M., Loarer, T., Porkolab, M., Sharapov, S.E., Valcarcel, D., Van Schoor, M., Weisen, H., Efficient generation of energetic ions in multi-ion plasmas by radio-frequency heating, (2017) Nature Physics, 13 (10), pp. 973-978.

[26] R.Kwiatkowski, G.Bołtruczyk, A.Brosławski, M.Gosk, S.Korolczuk, S.Mianowski, A.Szydłowski, A.Urban, I.Zychor, V.Braic, R.Costa Pereira, T.Craciunescu, D.Croft, M.Curuia, A.Fernandes,V.Goloborod'ko, G.Gorini, V.Kiptily, I.Lengar, J.Naish, R.Naish, M.Nocente, K.Schoepf, B.Santos, S.Soare, M.Tardocchi, V.Yavorskij, V.L.Zoita, CeBr3–based detector for gamma-ray spectrometer upgrade at JET, Fus. End. Design, 123, 2017, 986-989.

[27] Matti Laan, Antti Hakola, Peeter Paris, Kaarel Piip, Märt Aints, Indrek Jõgi, Jelena Kozlova, Hugo Mändar, Cristian Lungu, Corneliu Porosnicu, Eduard Grigore, Cristian Ruset, Jukka Kolehmainen, Sanna Tervakangas Dependence of

LIBS spectra on the surface composition and morphology of W/Al coatings, Engineering and Design, Volume 121, October 2017, Pages 296-30

[28] Louzguiti, A., Zani, L., Ciazynski, D., Turck, B., Duchateau, J.-L., Torre, A., Topin, F., Bianchi, M., Ricchiuto, A.C., Bagni, T., Anvar, V.A., Nijhuis, A., Tiseanu, I.

A. Lozguiti, L. Zani, D. Ciazynski, B. Turck, J.L. Duchateau, A. Torre, F. Topin, M. Bianchi, A.C. Ricchiuto, T. Bagni, V.A. Anvar, A. Nijhuis, I. Tiseanu, Development of a New Generic Analytical Modeling of AC Coupling Losses in Cable-in-Conduit Conductors

[29] M. Lungu, "Surface microanalysis of fusion plasma exposed samples", PhD thesis defend, University of Bucharest, Faculty of Physics (November 2017)

[30] Marin,A; Lungu,CP; Porosnicu,C Influence of gaseous environments on beryllium-tungsten and tungsten surfaces investigated by XPS Journal of Vacuum Science & Technology A: Vacuum, Surfaces, and Films,35, issue 6, Article number:061304 (2017)

[31] Alexandru Marin, Cristian P. Lungu, Corneliu Porosnicu, Influence of gaseous inclusions on aluminum-tungsten coatings investigated by XPS, Journal of Vacuum Science & Technology A: Vacuum, Surfaces, and Films,35, issue 6, Article number:061304 (2017)

[32] Mateus, R. , Hakola, A., Tiron, V., Porosnicu, C., Lungu, C.P., Alves,Study of deuterium retention in Be-W coatings with distinct roughness profiles, Fusion Engineering and Design, Volume 124, November 2017, Pages 464-467

[33] R. Mateus, A. Hakola, V. Tiron, C. Porosnicu, C.P. Lungu, E. Alves, "Study of deuterium retention in Be-W coatings with distinct roughness profiles", Fusion Engineering and Design, 124 (2017) 464-467.

[34] M Mayer, S Krat, A Baron-Wiechec, Yu Gasparyan, K Heinola, S Koivuranta, J Likonen, C Ruset, G de Saint-Aubin, A Widdowson and JET Contributors, Erosion and deposition in the JET divertor during the second ILW campaign, Phys. Scr. T170 (2017) 014058 (8pp)

[35] P. Merkel, E. Strumberger, Linear MHD stability studies with the STARWALL code, arXiv:1508.04911 (2015).

[36] H. Meyer, T. Eich, M. Beurskens, .., I. G. Miron et al, Nucl. Fusion 57, 102014 (2017)

[37] L. Moser, R. Doerner, M. Baldwin, C. Lungu, C. Porosnicu, M. Newman, A. Widdowson, E. Alves, G. Pintsuk, J. Likonen,A. Hakola, R. Steiner, L. Marot, E. Meyer, Investigation and plasma cleaning of first mirrors coated with relevant ITER contaminants: beryllium and tungsten, Nuclear Fusion, Volume: 57 Issue: 8 Article Number: 086019, Aug. 2017

[38] A.V. Muller, D. Ewert, A. Galatanu, M. Milwich, R. Neu, J.Y. Pastor, U. Siefken, E. Tejado, J.-H. You, Melt infiltrated Tungsten-Copper composites as advanced heat sink materials for plasma facing components of future nuclear fusion devices, Fusion Engineering and Design 124 (2017) 455.

[39] Murari, A., Craciunescu, T., Peluso, E., Gelfusa, M., Detection of causal relations in time series affected by noise in tokamaks using geodesic distance on gaussian manifolds, (2017) Entropy, 19 (10), art. no. 569

[40] Murari, A., Craciunescu, T., Peluso, E., Lerche, E., Gelfusa, M., On efficiency and interpretation of sawteeth pacing with on-axis ICRH modulation in JET, (2017) Nuclear Fusion, 57 (12), art. no. 126057

[41] M. Rubel, P. Petersson, Y. Zhou, J. Coad, C. Lungu, I. Jepu, C. Porosnicu, D. Matveev, A. Kirschner, S. Brezinsek, A. Widdowson, E. Alves, Fuel Inventory and Deposition in Castellated Structures in JET-ILW, Nuclear Fusion 57(6):066027 ·June 2017 DOI: 10.1088/1741-4326/aa6864

[42] C. Ruset, D. Falie, E. Grigore, M. Gherendi, V. Zoita, K.-D. Zastrow, G. Matthews, X. Courtois, J. Bucalossi, J. Likonen, JET Contributors, The emissivity of W coatings deposited on carbon materials for fusion applications, Fusion Engineering and Design, 114, 192–195, 2017

[43] M. I. Rusu, C. Pardanaud, Y. Ferro, G. Giacometti, C. Martin, Y. Addab, P. Roubin, M. Minissale, L. Ferry, F. Virot, M. Barrachin, C P Lungu, C Porosnicu, P Dinca, M Lungu, M. Köppen, P. Hansen, Ch. Linsmeier Preparing the future post-mortem analysis of beryllium-based JET and ITER samples by multi-wavelengths Raman spectroscopy on implanted Be, and co-deposited Be Nuclear Fusion 57 (2017) 076035 (15pp);

[44] Santos, B., Fernandes, A., Pereira, R.C., Neto, A., Bielecki, J., Craciunescu, T., Figueiredo, J., Kiptily, V., Murari, A., Nocente, M., Rigamonti, D., Sousa, J., Tardocchi, M., Giacomelli, L., Zychor, I., Broslawski, A., Gosk, M., Korolczuk,

S., Urban, A., Boltruczyk, G., Correia, C.M.B.A., Gonçalves, B., Control and data acquisition software upgrade for JET gamma-ray diagnostics, (2018) Fusion Engineering and Design, 128, pp. 117-121.

[45] F. Spineanu, M. Vlad, On the late phase of relaxation of two-dimensional fluids: turbulence of unitons, Focus on Turbulence in Astrophysical and Laboratory Plasmas, New Journal of Physics 19 (2017) 025004.

[46] V. Stancalie, "Photoionization of S3+ using the Breit-Pauli R-matrix method", 2018, Journal of Quantitative Spectroscopy & Radiative Transfer 205(2018) 7- 18, DOI: 10.1016/j.jqsrt.2017.09.027

[47] C.M. Ticos, M. Galatanu, A. Galatanu, C. Luculescu, A. Scurtu, N. Udrea, D. Ticos, M. Dumitru, Cracks and nanodroplets produced on tungsten surface samples by dense plasma jets, Applied Surface Science 434, 1122–1128 (2018).

[48] V. Tiron, I.-L. Velicu, C. Porosnicu, I. Burducea, P. Dinca, P. Malinský Tungsten Nitride Coatings Obtained by HiPIMS as Plasma Facing Materials for Fusion Applications Applied Surface Science, Volume: 416 Pages: 878-884 Published: SEP 15 2017;

[49] Torokhtii, K., Pompeo, N., Frolova, A., V. Pinto, A. Angrisani , L. Piperno, G. Celentano, T. Petrisor, L. Ciontea, R. B. Mos, M. Nasui, G. Sotgiu, G., Silva, E. Microwave Measurements of Pinning Properties in Chemically Deposited YBCO/BZO Films, IEEE Transactions on Applied Superconductivity, 27(4),7763761 (2017).

[50] I.-L. Velicu, V. Tiron, I. Mihaila, C. Costin, Pulsed magnetron sputtering: the role of the applied power on tungsten coatings properties, Recent advances in technology research and education, Proceedings of the 16th International Conference on Global Research and Education Inter-Academia 2017, in the series: Advances in Intelligent Systems and Computing, Vol. 660, Springer (2018) 183-190.

[51] Velicu, I.-L., Tiron, V. , Porosnicu, C., Burducea, I., Lupu, N., Stoian, G., Popa, G., Munteanu, D. , Enhanced properties of tungsten thin films deposited with a novel HiPIMS approach, Applied Surface Science, Volume 424, Part 3, 1 December 2017, Pages 397-406;

[52] Vlad M, Spineanu F, Random and quasi-coherent aspects in particle motion and their effects on transport and turbulence evolution, Focus on Turbulence in Astrophysical and Laboratory Plasmas, New Journal of Physics 19 (2017) 025014.

[53] Vlad M., Baran V. V., Spineanu F., Iterated self-consistent study of the evolution of ion temperature gradient driven turbulence, in preparation

[54] Vlad M., Spineanu F., Combined effects of hidden and polarization drifts on impurity transport in tokamak plasmas, JET pinboard, submitted 2018.

[55] Vlad M., Spineanu F., Hidden drifts in turbulence, JET pinboard, submitted 2018.

[56] Vlad M., Spineanu F., Quasi-coherent structures and flows in turbulent transport, Journal of Physics: Conf. Series 936 (2017) 012057.

[57] I.Voitsekhovitch, R. Hatzky, D. Coster, F. Imbeaux, D. C. McDonald, T. B. Fehér, K. S. Kang, H. Leggate, M. Martone, S. Mochalskyy, X. Sáez, T. Ribeiro, T.-M. Tran, A. Gutierrez-Milla, T. Aniel, D. Figat, L. Fleury, O. Hoenen, J. Hollocombe, D. Kaljun, G. Manduchi, M. Owsiak, V. Pais, B. Palak, M. Plociennik, J. Signoret, C. Vouland, D. Yadykin, F. Robin, F. Iannone, G. Bracco, J. David, A. Maslennikov, J. Noé, E. Rossi, R. Kamendje, S. Heuraux, M. Hölzl, S. D. Pinches, F. Da Silva & D. Tskhakaya, "Recent EUROfusion Achievements in Support of Computationally Demanding Multiscale Fusion Physics Simulations and Integrated Modeling", 2018, Fusion Science and Technology, pp 1-12, doi: 10.1080/15361055.2018.1424483

[58] A Weckmann, P Petersson, M Rubel , E Fortuna-Zaleœna, W Zielinski, B Romelczyk-Baishya, E Grigore, C Ruset and A Kreter, Ageing of structural materials in tokamaks TEXTOR liner study, Phys. Scr. T170 (2017) 014053

[59] L.E. Zakharov, C.V. Atanasiu, K. Lackner, M. Hoelzl, and E. Strumberger, Electromagnetic thin-wall model for simulations of plasma wall-touching kink and vertical modes, Plasma Phys. 81, (2015).

[60] L.E. Zakharov, S.A. Galkin, S.N. Gerasimov, Understanding disruptions in tokamak, Phys. of Plasmas 19, 055703 (2012).

[61] L.E. Zakharov, The theory of the kink mode during the vertical plasma disruption events in tokamaks, Physics of Plasmas 15, 062507 (2008).

Conferences

[1] Angrisani Armenio, L. Piperno, G. Luca De Marzi, V. Pinto, A. Mancini, F. Rizzo, A. Vanozzi, A. Rufoloni, A. Augieri, V. Galuzzi, R.B. Mos, L. Ciontea, M. Nasui, T. Petrisor jr., G. Celentano, Is Surface Decoration The New Black?" A Comparison Between Surface Decoration And Artificial Pinning Centers , 13th European Conference on Applied Superconductivity (EUCAS 2017), Geneve (Ch), 17-22/09/2017.

[2] C.V. Atanasiu, L.E. Zakharov, K. Lackner, M. Hoelzl, E. Strumberger, Simulation of the electromagnetic wall response to plasma wall-touching kink and vertical modes with application to ITER, 59th Annual Meeting of the APS Division of Plasma Physics, Milwaukee, WI, US, October 23-27, 2017 (oral presentation).

[3] C.V. Atanasiu, L.E. Zakharov, K. Lackner, M. Hoelzl, E. Strumberger, Wall currents excited by plasma wall-touching kink and vertical modes, JOREK Meeting, Prague - 20-24/03/2017 (oral presentation).

[4] C.V. Atanasiu, L.E. Zakharov, K. Lackner, M. Hoelzl, F.J. Artola, E. Strumberger, X. Li, Modelling of wall currents excited by plasma wall-touching kink and vertical modes during a tokamak disruption, with application to ITER, 17th European Fusion Theory Conference, Athens – Greece, October 9-12, 2017 (oral presentation).

[5] V.Avrigeanu and M.Avrigeanu, 6th Workshop on Nuclear Level Density and Gamma Strength, May 8–12, 2017,

[6] Avrigeanu, Int. School on Nuclear Physics and Applications, Sept. 10-16, 2017, Varna, Bulgaria (invited lecture); J. Phys. Conf. Ser. (in press).

[7] M.Avrigeanu and V.Avrigeanu, 6th Workshop on Nuclear Level Density and Gamma Strength, May 8–12, 2017.

[8] V. Baran, M. Vlad, F. Spineanu, Evolving the ITG driven turbulence with test modes, 17th European Fusion Theory Conference, Athens, Greece, 9-12 October 2017.

[9] V. Baran, M. Vlad, F. Spineanu, ITG driven turbulence: test mode approach, 17th International Conference on Plasma Physics and Applications, Magurele, Romania, 15-20 June, 2017

[10] Bogdan Butoi, Corneliu Porosnicu, Paul Dinca, Ionut Jepu, Oana Gloria Pompilian, Cristian Lungu; DCMS and HiPIMS deposition of W and WN thin films for deuterium desorbtion study, IBWAP 17th Constanta, 11-14 iulie 2017, S2 O4

[11] Costin, V. Anita, G. Popa, J. Scholten, G. De Temmerman, Advances in probe diagnostics for linear plasma generators, TIM 17 Physics Conference, May 25-27, 2017, Timisoara, Romania (invited lecture).

[12] Craciunescu, T., Murari, A., Peluso, E., Gelfusa, M., Lungaroni, M., Gaudio, P., Complex networks for the analysis of the synchronization of time series relevant for plasma fusion diagnostics,(2017) 2017 European Conference on Circuit Theory and Design, ECCTD 2017, art. no. 8093302, .

[13] T.Craciunescu, A.Murari, E.Peluso, M.Gelfusa, M.Lungaroni, P.Gaudio, Complex networks for the analysis of the synchronization of time series relevant for plasma fusion diagnostics, European Conference on Circuit Theory and Design ECCTD 2017, Catania, Sept. 4-6, 2017

[14] T. Craciunescu, A. Murari, V. kiptily, Frontiers in Tomography Reconstruction Methods for Tokamak Plasmas, 2nd European Conference on Plasma Diagnostics (ECPD) , 18-21 April 2017 Bordeaux, France

[15] A.Croitoru, F. Spineanu, M. Vlad, On secondary contributions to the formation of an internal transport barrier, Computational Plasma Physics Conference, 20-22 November 2017, York, UK

[16] A.Croitoru, F. Spineanu, M. Vlad, On secondary contributions to the formation of an internal transport barrier, Computational Plasma Physics Conference, 20-22 November 2017, York, UK

[17] A.Croitoru, Transport of cold ions in tokamak microturbulence, 17th International Conference on Plasma Physics and Applications, Magurele, Romania, 15-20 June, 2017

[18] C P Dhard, M Balden, S Brezinsek, J W Coenen, A Dudek, G Ehrke, D Hathiramani, S Klose, R König, M Laux, Ch Linsmeier, A Manhard, S Masuzaki, M Mayer, G Motojima, D Naujoks, R Neu2, O Neubauer, M Rack, C Ruset, T Schwarz-Selinger, T Sunn Pedersen, M Tokitani, B Unterberg, M Yajima and The W7-X Team, Preparation of erosion and deposition investigations on plasma facing components in Wendelstein 7-X, 16th International Conference on Plasma-Facing Materials and Components for Fusion Applications, Düsseldorf Neuss 16th –19th May 2017

[19] Dinca, C. Porosnicu, V. Tiron, B. Butoi, I. Jepu, O.G. Pompilian, I. Burducea, C.P. Lungu; The influence of nitrogen gas inclusions on deuterium retention and release properties of Be-W mixed layers; CPPA 2017, 15-20 iunie 2017, Magurele, Romania;

[20] Paul Dinca, Oana Gloria Pompilian, Corneliu Porosnicu Bogdan Butoi, Ion Burducea and Cristian P. Lungu; The influence of Ar/D ratio on D retention in Beryllium thin films obtained by direct current megnetron sputtering method; IBWAP 17th, 11-14 iulie 2017, Constanta, S2 O5

[21] M. Galatanu, M Enculescu, G. Ruiu, C. Stancu, G. Dinescu, A. Galatanu, "Functional interfaces in W-Ti and W-V laminates" , poster presented at IBWAP 2017 (July 11-14, 2017, Constanta, Romania).

[22] Galatanu, G. Ruiu, M. Enculescu, A. Galatanu, "FAST brazing technology for multi-layered composite materials processing", oral presentation at NUCLEAR 2017 -The 10th Annual International Conference on Sustainable Development through Nuclear Research and Education (May 24-26, 2017, Piteşti, România)

[23] Galatanu, M. Enculescu, G. Ruiu, A. Galatanu, "Thermophysical properties of W based plasma facing materials for fusion reactors", poster presented at 17th Conference on Plasma Physics and Applications (June 15-20, 2017, Magurele, Romania)

[24] M. Galatanu, M. Enculescu, G. Ruiu, A. Galatanu, "High temperature thermo-physical properties of Cu-based thermal barrier composites", poster presented at IBWAP 2017 (July 11-14, 2017, Constanta, Romania)

[25] M. Galatanu, M. Enculescu, G. Ruiu, B. Popescu, A. Galatanu"Thermal barriers for DEMO W-monoblock divertor", poster presented at 16th International Conference on Plasma-Facing Materials and Fusion Applications (May 15-19, 2017, Duesseldorf/Neuss, Germany)

[26] Ye.O. Kazakov, J. Ongena, V.G. Kiptily, E. Lerche, M. Nocente, M.J. Mantsinen, M. Schneider, D. Van Eester, Y. Baranov, J. Bielecki, R. Bilato, A. Czarnecka, T. Craciunescu, R. Dumont, J. Eriksson, J. Faustin, L. Giacomelli, C. Hellesen, Ph. Jacquet, N. Krawczyk, S.E. Sharapov, H. Weisen, J.C. Wright, S.J. Wukitch, A novel ICRF heating scenario with application to ITER and DEMO: theory and experimental verification on JET and Alcator C-Mod, International Conference on Research and Application of Plasmas, 18th to the 22nd of September in Warsaw, Poland

[27] S. Krat, M. Mayer, A. Baron-Wiechec, Yu. Gasparyan, K. Heinola, I. Jepu, C. Ruset, G. de Saint-Aubin, A. Widdowson and JET Contributors, Erosion, deposition and deuterium inventory of the bulk tungsten divertor tile during the second JET ITER-like wall campaign, 16th International Conference on Plasma-Facing Materials and Components for Fusion Applications, Düsseldorf / Neuss 16th –19th May 2017

[28] M. Lungu, C. Dobrea, I. Porosnicu, I. Tiseanu, XRF Thickness Calibration by Combined Monte Carlo Modeling and Reference Probes, The 17th International Balkan Workshop on Applied Physics, 11-14 July 2017, Constanta, Romania

[29] M. Lungu, C. Dobrea, I. Porosnicu, I. Tiseanu, Non-destructive analysis of fusion relevant tungsten coating by X-ray methods, 17th International Conference of Plasma Physics and Applications, 15-20 Iunie. 2017, Măgurele, România;

[30] M. Lungu, C. Dobrea, I. Porosnicu, I. Tiseanu, XRF thickness calibration by combined Monte Carlo Modelling and reference probes, The 17th International Balkan Workshop on applied Physics", 11-14 July, Constanta, Romania

[31] M. Lungu, C. Dobrea, I. Tiseanu, Optimization and calibration of non-destructive analysis methods applied on fusion relevant samples, Annual Scientific conference "Knowledge means Physics", Universitatea Bucureşti, Facultatea de Fizică, 23-24 June 2017, Bucureşti, România;

[32] M. Mayer, S. Krat, A. Baron-Wiechec, Yu. Gasparyan, K. Heinola, S. Koivuranta, J. Likonen, C. Ruset, G. de Saint-Aubin, A. Widdowson, and JET Contributors, Erosion and deposition in the JET divertor during the second ITER-like wall campaign, 16th International Conference on Plasma-Facing Materials and Components for Fusion Applications, Düsseldorf / Neuss 16th –19th May 2017

[33] G. Miron, the EUROfusionMST1 Team and the ASDEX Upgrade Team, Modelling the effect of resonant magnetic perturbations on neoclassical tearing modes, 17th European Fusion Theory Conference, P2.9, Athens, Greece, 9-12 October 2017.

[34] Mircea Nasui, Ramona Bianca Mos, Anca Tomolea, Traian Petrisor Jr., Amalia Mesaros,. Mihai Gabor, Lelia Ciontea, Petrisor Traian, Development of a fluorine-free polymer-assisted- deposition route for YBa_2Cu_3O7-x superconducting films, 13th European Conference on Applied Superconductivity (EUCAS 2017), Geneve (Ch), 17-22/09/2017.

[35] M. Nocente, Ye.O. Kazakov, V. Kiptily, J. Ongena, T.Craciunescu, J.Eriksson, J.Faustin, L.Giacomelli, G.Gorini,, C.Hellesen, E.Lerche, M.Mantsinen, S.Sharapov, M.Tardocchi, D.VanEester, Observation of MeV range ions in radio frequency heating experiments with the three ion scenarios at JET, 15th IAEA Technical Meeting on Energetic Particles in Magnetic Confinement Systems, 5 -8 September 2017 in Princeton, NJ, USA

[36] V. Pais, V. Stancalie, C. Iorga, "Sistematic studies of atomic spectra based noSQL databases", 2017, PLASMA 2017 International Conference on Research and Applications of Plasmas, 17-22 September 2017, Warsaw, Poland

[37] T. Petrisor Jr et al.,Vortex pinning study on epitaxial $YBa_2Cu_3O_{7-x}$ thin film grown on decorated MgO(001) single crystal substrates with La0.66Sr0.33MnO3 nano-islands, 13th European Conference on Applied Superconductivity (EUCAS 2017), Geneve (Ch), 17-22/09/2017

[38] Porosnicu, V. Tiron, P. Dinca, B. Butoi, I. Burducea, O.G. Pompilian, I. Jepu and C.P. Lungu, HiPIMS and Reactive Magnetron Sputtering Techniques Used for Obtaining Fusion Related Materials; 16th International Conference on Plasma-Facing Materials and Components (16th PFMC).

[39] Porosnicu, V. Tiron, P. Dinca, B. Butoi, I. Burducea, O.G. Pompilian, I. Jepu and C.P. Lungu; The Influence of Be and W Films Microstructure and Nitrogen Pre-Implantation on Fuel Retention; 13th International Symposium on Fusion Nuclear Technology (ISFNT-13), P3-152

[40] Porosnicu, V. Tiron, P. Dinca, B. Butoi, I. Burducea, O.G. Pompilian, I. Jepu, C. P. Lungu , HiPIMS and Reactive Magnetron Sputtering Techniques Used for Obtaining Fusion Related Materials CPPA 2017, 15-20 iunie 2017, Magurele, Romania;

[41] Ruset, E. Grigore, M. Mayer, H. Greuner, B. Böswirth, C. Luculescu, M. Gherendi, C.P. Dhard, M. Laux, C/Mo marker coatings for measurement of erosion in the stellarator Wendelstein 7-X , 16th International Conference on Plasma-Facing Materials and Components for Fusion Applications, Düsseldorf / Neuss 16th –19th May 2017

[42] Ruset, E. Grigore, M. Rasinski, E. Fortuna, J. Grzonka, M. Gherendi, C. Luculescu, N. P. Barradas, E. Alves, A. Hakola, Nano-porous coatings for gas retention studies, 17th International Conference on Plasma Physics and Applications, Magurele-Bucharest, Romania, 15-20 June, 2017

[43] Ruset, E. Grigore, M. Rasinski, E. Fortuna, J. Grzonka, M. Gherendi, C. Luculescu, N. P. Barradas, E. Alves, A. Hakola, Nano-porous coatings for gas retention studies, 17th International Conference on Plasma Physics and Applications, Magurele-Bucharest, Romania, 15-20 June, 2017

[44] Santos, A. Fernandes, R.C. Pereira, A. Neto, J. Bielecki, T. Craciunescu, J. Figueiredo, V., Kiptily, A. Murari, M. Nocente, D. Rigamonti, J. Sousa, M. Tardocchi, L. Giacomelli, I. Zychor, A. Broslawski, M. Gosk, S. Korolczuk, A. Urban, G. Boltruczyk, C.M.B.A. Correia, B. Gonçalves, 11th IAEA Technical Meeting on Control, Data Acquisition, and Remote Participation for Fusion Research, Greifswald, Germany.

[45] Scurtu, N. Udrea, C. Luculescu, M. Galațanu, A. Galaţanu, D. Ticoș and C.M. Ticoș, “Impact of Dense Plasma Jets on Tungsten Surfaces”, IONS Balvanyos 2017, International OSA Network of Students, 25-28 July 2017, Balvanyos, Romania

[46] Scurtu, N. Udrea, C. Luculescu, M. Galaţanu, A. Galaţanu, D. Ticoş, C.M. Ticoş, “Cracks and Nanodroplets Produced on Tungsten Surface by Dense Plasma Jets”. 17th INTERNATIONAL CONFERENCE ON PLASMA PHYSICS AND APPLICATIONS, June 15-20 Magurele, Bucharest, Romania

[47] Spineanu, M. Vlad, A. Croitoru, Formation of an Internal Transport Barrier due to neutral beam injection during current ramp-up in tokamak, 17th International Conference on Plasma Physics and Applications, Magurele, Romania, 15-20 June, 2017.

[48] Spineanu, M. Vlad, A. Croitoru, Formation of an Internal Transport Barrier due to neutral beam injection during current ramp-up in tokamak, 17th International Conference on Plasma Physics and Applications, Magurele, Romania, 15-20 June, 2017.

[49] Spineanu, M. Vlad, Clusters of helicity and stochastic linking number generation in plasma, Europhysics Conference on Statistical Physics (SigmaPhi2017), Corfu, Greece, 10-15 July 2017
[50] Spineanu, M. Vlad, Clusters of helicity and stochastic linking number generation in plasma, Europhysics Conference on Statistical Physics (SigmaPhi2017), Corfu, Greece, 10-15 July 2017
[51] Spineanu, M. Vlad, Singular states of the 2D Euler fluid and of the density of eigenvalues of random matrices, Collisionless Boltzmann (Vlasov) equation and modeling of self-gravitating systems and plasmas, CIRM, Luminy October 30 – Novemver 3, 2017
[52] Spineanu, M. Vlad, Singular states of the 2D Euler fluid and of the density of eigenvalues of random matrices, Collisionless Boltzmann (Vlasov) equation and modeling of self-gravitating systems and plasmas, CIRM, Luminy October 30 – Novemver 3, 2017
[53] Stancu, E.R. Ionita, M. Teodorescu, S.D. Stoica, V. Marascu, G. Dinescu, AS. Peillon, F. Gensdarmes, C. Grisolia, Modification of tungsten surfaces by He and He/H_2 hollow cathode discharges, 17th International Conference on Plasma Physics and Applications (CPPA 2017), June 15-20, Magurele, Bucharest, Romania, poster presentation P7-10.
[54] C.M. Ticoş, M. Galaţanu, A. Galaţanu, C. Luculescu, A. Scurtu, N. Udrea, D. Ticoş, "Cracks and Nanodroplets Produced on Tungsten Surface by Dense Plasma Jets". 17th International Balkan Workshop on Applied Physics and Materials Science. IBWAP 2017, 11-14, July, 2017, Constanta, Romania
[55] V. Tiron, C. Costin, I. Mihaila, G. Popa, Ion energy distribution function measurements during high power impulse magnetron sputtering of W and Al targets in Ar-He and Ar-D_2 gas mixtures, 17th International Conference on Plasma Physics and Applications, CPPA 2017, June 15-20, 2017, Magurele, Bucharest, Romania (poster).
[56] Tiseanu, A. Galatanu, T. Craciunescu, C. Dobrea, M. Lungu and A. Sima, "Advanced X-ray imaging methods for characterization of plasma facing components struc-tural integrity and operation", EUROMAT 2017, September 17-22, 2017, Thessaloniki Greece
[57] Tiseanu, A. Galatanu, T. Craciunescu, C. Dobrea, M. Lungu, A. Sima, Advanced X-ray imaging methods for characterization of plasma facing components structural integrity and operation, EUROMAT2017, Thessaloniki, Greece, 17-22 September, 2017;
[58] Tiseanu, Comparative study on X-ray tomography/fluorescence by synchrotrons and conventional X-ray sources, The 2nd International workshop on materials physics organized by the National Institute of Material Phisycs (NIMP), Magurele, Romania, May 16-17, 2017;
[59] Tiseanu, X-ray tomography / fluorescence by synchrotrons and conventional X-ray sources, Application for imaging and metrology of automotive parts, The 5th Laser Ignition Conference (LIC '17), Bucharest, Romania, 20-23 June 2017;
[60] Tiseanu, X-ray Tomography/Fluorescence by Synchrotrons and Conventional X-ray Sources: Application to Imaging of Materials and Structures Synthesized / Processed with Lasers, Plasma and Electron Radiation, IONS Balvanyos 2017, Balvanyos, Romania, 25-28 July, 2017;
[61] Vanozzi, A. Augieri, G. Celentano, A. Rufoloni, S. Rubanov, T. Petrisor, Growth of biaxially –textured $La_2Zr_2O_7$ and Zr-doped CeO_2 on cold-rolled Ni-W substrates by CSD, 13th European Conference on Applied Superconductivity (EUCAS 2017), Geneve (Ch), 17-22/09/2017.
[62] I.-L. Velicu, V. Tiron, G. Popa, High Power Impulse Magnetron Sputtering: An overview on the benefits of ultra-short pulse operating mode, XXXIII International Conference on Phenomena in Ionized Gases (ICPIG) 2017, July 9-14, 2017, Estoril, Lisbon, Portugal (oral presentation).
[63] I.-L. Velicu, V. Tiron, I. Mihaila, C. Costin, Pulsed magnetron sputtering: the role of the applied power on tungsten coatings properties, 16th International Conference on Global Research and Education, Inter-Academia 2017, September 25-28, 2017, Iasi, Romania (poster).
[64] M. Vlad, F. Spineanu, Hidden drifts and turbulence evolution, Collisionless Boltzmann (Vlasov) equation and modeling of self-gravitating systems and plasmas, CIRM, Luminy, October 30 – November 3, 2017
[65] M. Vlad, F. Spineanu, Quasi-coherent aspects in turbulent transport, Europhysics Conference on Statistical Physics (SigmaPhi2017), Corfu, Greece, 10-15 July 2017

[66] M. Vlad, F. Spineanu, Radial pinch produced by the gradient of turbulence amplitude in tokamak plasmas, 17th International Conference on Plasma Physics and Applications, Magurele, Romania, 15-20 June 2017

[67] Weckmann, P. Petersson, M. Rubel , E. Fortuna-Zaleœna, W. Zielinski, B. Romelczyk-Baishya, E . Grigore, C. Ruset, A Kreter, Ageing of structural materials in tokamaks TEXTOR liner study, 16th International Conference on Plasma-Facing Materials and Components for Fusion Applications, Düsseldorf / Neuss 16th –19th May 2017

[68] E. Zakharov, Xujing Li, S.N. Gerasimov and JET Contributors, C.V. Atanasiu, K. Lackner, M. Hoelzl, E. Strumberger, J. Artola Such, Tokamak MHD and its interface (ssec) with the wall model, 30th ITPA-MHD Disruptions & Control topical group workshop October 9 2017, Fusion For Energy, Barcelona, Spain (oral presentation).

[69] L.E. Zakharov, C.V. Atanasiu,X. Li, Interface of wall current modeling with disruption simulation codes, JOREK-STARWALL discussion meeting, IPP, Garching bei München, Germany, March 10, 2017.

[70] L.E. Zakharov, H. Xiong, D. Hu,X. Li, C.V. Atanasiu, Hiro currents: physics and a bit of politics, Theory and Simulation of Disruptions Workshop, July 17-19, 2013,PPPL, Princeton NJ, USA (oral presentation).

[71] L.E. Zakharov, L. Guazzotto X. Li, C.V. Atanasiu, Outline of our work on disruption, Informal discussion, August 14, 2013, PPPL, Princeton NJ, USA (oral presentation).

[72] V. Zoita, T. Craciunescu, A. Fernandes, V. Kiptily, M. Anghel, D. Croft, M. Curuia, L., Giacomelli, D. Kina, I. Lengar, M. Riva, S. Soare, Performance of the neutron attenuators for the JET gamma-ray cameras, 17th International Conference on Plasma Physics and Applications (CPPA2017), Magurele-Bucharest, Romania, June 16-20, 2017

Annex 1

Members of the EUROfusion Consortium:

Country	Institute, University or Finance Agency
Austria	Austrian Academy of Sciences, Vienna
Belgium	Ecole Royale Militaire-Koninklijke Militaire School, Plasma Physics Laboratory, Brussels
Bulgaria	Bulgarian Academy of Sciences, Institute of Nuclear Research and Nuclear Energy, Sofia
Croatia	Ruđer Bošković Institute, Zagreb
Cyprus	University of Cyprus, Nicosia
Czech Republic	Academy of Sciences of the Czech Republic, Institute of Plasma Physics, Prague
Denmark	DTU, Plasma Physics and Fusion Energy, Lyngby
Estonia	University of Tartu, Institute of Physics
Finland	VTT Technical Research Centre of Finland, Espoo
France	Commissariat à l'énergie atomique et aux énergies alternatives,CEA, Cadarache
Germany	Forschungszentrum Jülich, FZJ; Karlsruhe Institute of Technology, KIT; Max Planck Institute of Plasma Physics, IPP, Garching and Greifswald
Greece	National Center For Scientific Research "DEMOKRITOS", Athens
Hungary	Hungarian Academy of Science, Wigner Research Centre for Physics, Budapest
Ireland	Dublin City University, Plasma Research Laboratory
Italy	Agenzia nazionale per le nuove tecnologie, l'energia e lo sviluppo economico sostenibile, ENEA (Italy), Frascati
Latvia	University of Latvia, Institute of Solid State Physics, Riga
Lithuania	Lithuanian Energy Institute, Kaunas
The Netherlands	FOM, Foundation for Fundamental Research on Matter, Utrecht
Poland	Institute of Plasma Physics and Laser Microfusion, Warsaw
Portugal	Universidade Técnica de Lisboa, Instituto Superior Técnico, IST IPFN
Romania	Institutul de Fizica Atomica (IFA), Illfov
Slovakia	Comenius University, Department of Experimental Physics, Bratislava
Slovenia	JSI Jozef Stefan Institute, Ljubljana
Spain	Centro de Investigataciones Energeticas, Medioambientales y Tecnologicas, (CIEMAT), Madrid
Sweden	Vetenskapsrådet, Stockholm
Switzerland	École Polytechnique Federale de Lausanne EPFL, Swiss Plasma Center (SPC), Lausanne
United Kingdom	Culham Centre for Fusion Energy (CCFE), Host to JET

Annex 2

EUROfusionWork Packages:

- WPJET1 JET Campaign*
- WPJET2 Plasma-Facing Components*
- WPJET3 Technological Exploitation of DT Operation*
- WPJET4 JET Enhancements*
- WPMST1 Medium-Size Tokamak Campaigns*
- WPMST2 Preparation of the exploitation of Medium Size Tokamaks
- WPPFC Preparation of efficient PFC operation for ITER and DEMO*
- WPDTT1 Assessment of alternative divertor geometries and liquid metals PFC
- WPDTT2 Definition and design of the DTT
- WPSA Preparation of exploitation of JT-60SA*
- WPS1 Preparation and Exploitation of W7-X Campaigns
- WPS2 Stellarator Theory Development and Modelling
- WPCD Integrated Tokamak Modelling Code*
- WPISA Infrastructure Support Activities*
- WPPMI Plant Level System Engineering, Design Integration and Physics Integration
- WPMAG Magnet system*
- WPBB Breeding blanket
- WPCS Containment Structures
- WPDIV Divertor
- WPHCD Heating and current drive systems
- WPTFV Tritium, fuelling & vacuum systems
- WPBOP Heat transfer, balance-of-plant and site
- WPD&C Diagnostic and control
- WPRM Remote Maintenance Systems
- WPMAT Materials*
- WPENS Early Neutron Source
- WPSAE Safety and Environment
- WPSES Socio Economic studies
- WPPI Public Information
- WPEDU Education*
- WPTRA Training
- WPENR Enabling Research*
- WPPMU Management*

* with Romanian participation

Collaborations of Romanian teams:

- *Max Planck Institute for Plasma Physics, Garching, Germany*
  (National Institute for Laser, Plasma and Radiation Physics, Romania; *pag 13**)*
- *Consorzio RFX (CNR, ENEA, INFN, Universita' di Padova, Acciaierie Venete SpA), Corso Stati Uniti 4, 35127 Padova, Italy*
  (National Institute for Laser, Plasma and Radiation Physics, -, Romania, *pag 32**)*
- *Instituto de Plasmas e Fusão Nuclear, Instituto Superior Técnico, Universidade de Lisboa*
  (Institute of Atomic Physics, Bucharest, Romania; *pag 40**)*
- *University of Rome "Tor Vergata", Via del Politecnico 1, 00133 Rome, Italy*
  (National Institute for Laser, Plasma and Radiation Physics, -, Romania, *pag 32**)*
- *University of Innsbruck, Fusion@Österreichische Akademie der Wissenschaften, Austria*
  (Institute of Atomic Physics, Bucharest, Romania; *pag 40**)*
- *Instituto di Fisica del Plasma "Piero Caldirola«, Consiglio Nazionale delle Ricerche, Milano, Italy*
  (Institute of Atomic Physics, Bucharest, Romania; *pag 40**)*
- *Slovenian Fusion Association (SFA), Jozef Stefan Institute, Reactor Physics Department, Ljubljana, Slovenia*
  (Institute of Atomic Physics, Bucharest, Romania; *pag 40**)*
- *Institute of Plasma Physics and Laser Microfusion, Warsaw, Poland,*
  (Institute of Atomic Physics, Bucharest, Romania; *pag 40**)*
- *Princeton Plasma Physics Laboratory, Princeton, USA*
  (National Institute for Laser, Plasma and Radiation Physics, Romania; *pag 13**)*